

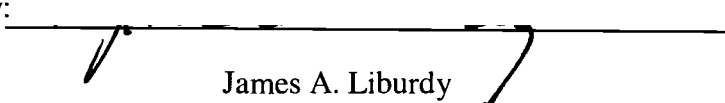
AN ABSTRACT OF THE THESIS OF

Guozhong Yang for the degree of Master of Science in Mechanical Engineering
presented on December 4, 2003.

Title: A Numerical Model of Drop-on-Demand Droplet Formation from a Vibrating
Nozzle and a Rigid Nozzle.

Redacted for Privacy

Abstract Approved by:


James A. Liburdy

Droplet formation from a rigid and a vibration nozzle driven by a pulsing pressure is simulated. Droplet formation is simulated by using one-dimensional model. For the case of droplet formation from a vibration nozzle, the nozzle vibration is simulated by large deflection plate vibration equation. Droplet formation from a rigid nozzle is studied simply by setting the nozzle deflection always to be zero. The one-dimensional model is solved by MacCormack method. The large deflection plate vibration equation is solved by mode shape approximation and Runge—Kuta time integration method. Three different effect factors, the driving pressure thrust input effects, the fluid viscosity effects, and the nozzle vibration effects, on droplet formation are studied. The driving pressure thrust input effects and the fluid viscosity effects are studied based on a rigid nozzle. The nozzle vibration effects are studied by

comparing the results from a vibration nozzle with the results from a rigid nozzle. Results show: 1) the primary droplet break-off time is constant if the driving pressure magnitude is high, but the primary droplet volume and primary droplet velocity increase slightly as the driving pressure thrust input increase; 2) higher thrust input can possibly result in the occurrence of overturn phenomenon; 3) increasing the fluid viscosity cause the primary droplet break-off later, but the primary droplet volume and the primary droplet velocity does not change significantly by fluid viscosity; 4) the nozzle vibration effect on the primary droplet break-off time and the primary droplet size is small, but the nozzle vibration cause the primary droplet velocity to increase by an amount of the nozzle vibration velocity magnitude; 5) nozzle vibration cause longer liquid thread to form and the total satellite droplet volume to increase significantly which eventually break into multiple satellite droplet.

© Copyright by Guozhong Yang

December 4, 2003

All Rights Reserved

A Numerical Model of Drop-on-Demand Droplet Formation from
a Vibrating Nozzle and a Rigid Nozzle

By

Guozhong Yang

A THESIS

Submitted to

Oregon State University

In partial fulfill of

the requirements for the

degree of

Master of Science

Presented on December 4, 2003

Commencement in June 2004

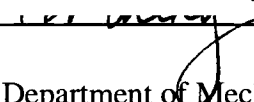
Master of Science thesis of Guozhong Yang presented on December 4, 2003

APPROVED:

Redacted for Privacy


Major Professor, representing Mechanical Engineering

Redacted for Privacy


Head of Department of Mechanical Engineering

Redacted for Privacy


Dean of the Graduate School

I understand that my thesis will become part of the permanent collection of Oregon State University libraries. My signature below authorizes release of my thesis to any reader upon request.

Redacted for Privacy

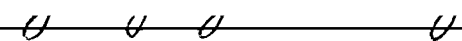

Guozhong Yang, Author

TABLE OF CONTENTS

	<u>Page:</u>
1. INTRODUCTION.....	1
2. LITERATURE REVIEW.....	4
2.1 Drop-on-demand Droplet Formation in Ink-Jet Printer.....	4
2.2 Non-rigid Fluid Chamber.....	6
2.3 Numerical Modeling of Droplet Formation	7
2.4 Droplet Break-off Process.....	10
3. THEORETICAL DERIVATION.....	13
3.1 One-Dimensional Droplet Model.....	13
3.2 Early Stage Droplet Formation Model.....	18
3.3 Modeling Nozzle Flow.....	21
3.4 Nozzle Vibration Dynamics.....	22
4. NUMERICAL CODING.....	32
4.1 Numerical Schemes.....	32
4.2 Stability Analysis.....	43
4.3 Numerical Converged Solution.....	48
4.4 Uncertainty.....	51
4.5 Validation of Coding.....	52
5. DATA ANALYSIS.....	55
5.1 Test Conditions.....	55

TABLE OF CONTENTS (CONTINUED)

	<u>Page:</u>
5.2 Data Processing	60
6. RESULTS.....	66
6.1 Droplet Formation from A Rigid Nozzle.....	71
6.2 Nozzle Vibration Effect on Droplet Formation.....	
6.3 Phase Angle Study of Break-off Relative to Nozzle	81
Vibration	93
7. CONCLUSIONS AND RECOMENDATIONS.....	96
7.1 Conclusions	96
7.2 Recommendations.....	97
BIBLIOGRAPHY.....	99
APPENDICES.....	102
A. FORTRAN Source Code.....	103
B. MATLAB Code for Data Processing.....	141
C. Sample Droplet Formation Time Sequences.....	151

LIST OF FIGURES

<u>Figure:</u>	<u>Page:</u>
3.1 Schematic of liquid jet shape and the coordinate	14
3.2 Schematic of liquid jet shape in the early stage	20
3.3 Plate free vibration normalized orthogonal mode shapes for clamped edge boundary condition, mode numbers 1 through 6	28
4.1 Relationship of parts of the model	33
4.2 Numbering sequence of nodes	35
4.3 Threshold gradient calculations	40
4.4 Liquid column break-off shapes by different break-off criteria	43
4.5 Sample driving pressure for showing convergence of the code	49
4.6 Sample break-off shapes by different grid size	50
4.7 Dripping water simulation comparison with that of Eggers	54
5.1 Pressure function studied with arbitrary unit	59
5.2 Definition of the primary droplet, satellite droplet, primary droplet break-off position, and satellite break-off position; all units are nondimensionalized by the capillary scales	62
5.3 Typical nozzle deflection history; all units are nondimensionalized by the capillary scales	65
6.1 Sample driving pressure and the resulted nozzle deflection history: a) the driving pressure versus time, b) nozzle deflection versus time; all units are nondimensionalized by the capillary scales.	67
6.2 Sample droplet formation time evolution.	68

LIST OF FIGURES (CONTINUED)

<u>Figure:</u>	<u>Page:</u>
6.3 Liquid shape, velocity, and capillary pressure distribution at a time close to break-off. The final primary break-off point indicated is predicted by capillary wave instability; all units are nondimensionalized by the capillary scales	69
6.4 Break-off shapes for rigid nozzle by different pressure inputs; all units are nondimensionalized by the capillary scales; (a) $P^* = 2.5$, (b) $P^* = 5$, (c) $P^* = 10$	73
6.5 Primary droplet formation parameters versus nondimensional thrust $P^* \cdot T^*$; all units are non-dimensionalized by the capillary scales; a) primary break-off time, t_d^* , b) primary break-off length, l_d^* , c) primary droplet volume, V_d^* , d) primary droplet velocity, u_d^* . 'o', '□', and '+' represent $P^* = 10, 5, \text{ and } 2.5$ respectively	75
6.6 Satellite droplet formation parameters versus nondimensional thrust $P^* \cdot T^*$; all units are nondimensionalized by the capillary scales; a) primary break-off time, t_s^* , b) primary droplet volume, V_s^* . 'o', '□', and '+' represent $P^* = 10, 5, \text{ and } 2.5$ respectively	76
6.7 Break-off shapes versus viscosity as expressed through Re/We ; all units are nondimensionalized by the capillary scales; (a) $P^* = 2.5$, (b) $P^* = 5$, (c) $P^* = 10$	78
6.8 Viscous effect on primary droplet; all units are nondimensionalized by the capillary scales; a) primary break-off time, t_d^* , b) primary break-off length, l_d^* , c) primary droplet volume, V_d^* , d) primary droplet velocity, u_d^* ; 'o', '□', and '+' symbol represent $P^* = 10, 5, 2.5$ respectively Comparison of break-off shapes of water by vibration and rigid nozzle	79
6.9 Viscous effect on satellite droplet formation; all units are nondimensionalized by the capillary scales; a) satellite break-off time, t_s^* , b) satellite volume, V_s^* ; 'o', '□', and '+' represent $P^* = 10, 5, \text{ and } 2.5$ respectively	80

LIST OF FIGURES (CONTINUED)

<u>Figure:</u>	<u>Page:</u>
6.10 Comparison of break-off shapes by water with viscosity parameter $Re/We=60$ from a vibration and a rigid nozzle; all units are nondimensionalized by the capillary scales; (a) rigid nozzle, (b) vibration nozzle	83
6.11 Comparison of break-off shapes by fluid with viscosity parameter $Re/We=5$ from a vibration and a rigid nozzle; all units are nondimensionalized by the capillary scales; (a) rigid nozzle, (b) vibration nozzle.	84
6.12 Nozzle vibration effect on the primary droplet; all units are nondimensionalized by the capillary scales; a) the primary break-off time, b) the primary break-off length, c) the primary droplet volume, d) the primary droplet velocity. 'o', '□', 'x' and '+' represent rigid nozzle $Re/We = 5$, rigid nozzle $Re/We = 60$, vibration nozzle $Re/We = 5$, and vibration nozzle $Re/We = 60$ respectively	85
6.13 Magnitude of primary droplet velocity change by nozzle vibration; all units are nondimensionalized by the capillary scales; (a) fluid viscosity $Re/We=5$, (b) fluid viscosity $Re/We=60$	86
6.14 Nozzle vibration effect on satellite droplet; all units are nondimensionalized by the capillary scales; a) the satellite break-off time, b) the satellite volume; 'o', '□', 'x' and '+' represent rigid nozzle $Re/We = 5$, rigid nozzle $Re/We = 60$, vibration nozzle $Re/We = 5$, and vibration nozzle $Re/We = 60$ respectively	87
6.15 Comparison of break-off shape by three different vibration nozzles; all units are nondimensionalized by the capillary scales; (a) $h^* = 0.32$, (b) $h^* = 0.64$, (c) $h^* = 0.96$	89
6.16 Nozzle vibration effect on primary droplet by three different nozzles; all units are nondimensionalized by the capillary scales; a) the primary break-off time, b) the primary break-off length, c) the primary droplet volume, d) the primary droplet velocity; 'o', '□', and '+' represent $h^* = 0.32, 0.64, \text{ and } 0.96$ respectively	90

LIST OF FIGURES (CONTINUED)

<u>Figure:</u>	<u>Page:</u>
6.17 Nozzle vibration effect on satellite compared that from rigid nozzle; all units are nondimensionalized by the capillary scales; a) satellite break-off time, b) satellite volume. 'o', '□', and '+' represent $h^* = 0.32, 0.64, \text{ and } 0.96$ respectively	92
6.18 Phase angle study of primary droplet break-off; all units are nondimensionalized by the capillary scales	94
6.19 Phase angle study of satellite break-off time; all units are nondimensionalized by the capillary scales.	95

LIST OF TABLES

<u>Table:</u>	<u>Page:</u>
3.1 Roots of equation (3.39), mode numbers 1 through 6	25
4.1 Break-off criteria	41
4.2 Uncertainty analysis of the numerical scheme	51
4.3 Dimensional parameters of Eggers (1994) used for validation	53
4.4 Non-dimensional parameters for coding validation	53
5.1 Dimensional parameters chosen for capillary scales calculation	55
5.2 The resulting capillary scales	56
5.3 Fluids studied	56
5.4 Nozzle plate properties	57
5.5 Nozzle plates studied	57
5.6 Nozzle plates non-dimensional first mode natural frequency and stiffness parameter	58
5.7 Driving pressure input	59

NOMENCLATURE

A:	Cross section area, $A = \pi \cdot r^2$
Bo:	Bound number
C:	Damping coefficient
D:	Bending rigidity
E:	Young's modulus
F:	Airy stress function
G:	Radius amplification factor
K:	Liquid column principle radii
L:	Liquid column tip position
P:	Driving pressure magnitude
Q	Velocity amplification factor
R:	Spherical shape radius
Re:	Reynolds number
T:	Driving pressure pulse times
Urel:	Velocity relative to nozzle vibration velocity magnitude
V:	Volume of droplet
We:	Weber number
X:	Dependent term in the hyperbolic one-dimensional equation
Y:	Convection term in the hyperbolic one-dimensional equation
Z:	Acceleration term in the hyperbolic one-dimensional equation
a:	Nozzle radius

c:	Capillary wave speed
d:	Nozzle plate diameter
f:	Frequency
g:	Gravitation acceleration
h:	Nozzle plate thickness
l:	Droplet break-off length
p:	Pressure
r:	Radius in one-dimensional coordinate frame
t:	Time
u:	Velocity in one-dimensional coordinate frame
w:	Nozzle plate deflection
z:	Position in fixed one-dimensional coordinate frame
β :	Arbitrary constant value, unit: 1/m
γ :	Liquid-air interface surface tension
δ :	Kronecker unit tensor
δt :	Time step
δX :	Dependent term increment
$\delta \eta$:	Spatial grid size
η :	Position in moving one-dimensional coordinate frame
κ :	$\kappa = \beta \cdot d$, Mode shape constant
λ :	Wave length
μ :	Dynamic viscosity of fluid
ρ :	Density

σ :	Normal stresses
τ :	Nozzle vibration period
ν :	Poisson ratio
ϕ :	Phase angle
ψ :	Radius amplification factor
φ :	Amplification factor
\mathfrak{R} :	Plate vibration mode shape function
\mathfrak{S} :	Plate vibration mode frequency function

Subscript:

0:	Driving input
N:	Normal
T:	Tangential
a:	Ambient
c:	Capillary scales
d:	Primary droplet
e:	Nozzle exit plane
i, j:	Node identification number
η :	In moving one-dimensional coordinate frame
n:	Plate mode shape identification number
l:	Liquid
p:	Plate
s:	Satellite droplet
t:	Liquid jet tip

Superscript:

*: Non-dimensional form

n: Time step identification number

A Numerical Model of Drop-on-Demand Droplet Formation from a Vibrating Nozzle and a Rigid Nozzle

1. INTRODUCTION

Droplet formation is an important process being widely used in ink-jet printing, fuel atomization, and solid particle transportation. Research on droplet formation has continued for more than one century. Drop-on-demand (DOD) droplet formation, which can produce a single droplet asynchronously on demand, is one type of droplet formation process widely used in ink-jet printing. Printing quality is crucial to DOD printing systems. Controlling droplet size, droplet velocity and minimizing satellite effect are critical for improving printing quality. In addition, the ability to control droplet formation by only varying the operation is a great advantage which makes the DOD printing systems more versatile and finally more competitive in market.

Droplet formation is a complex interaction among surface tension, viscous force, and momentum. Momentum is related to input operating boundary conditions. Surface tension force comes from the surface shape and the interfacial properties. Viscous force is related to fluid viscosity directly. In DOD ink-jet printing technology, what can be varied are the nozzle geometry, the operating conditions and the fluid properties. Understanding different operating condition and fluid properties effects on droplet formation is critical in designing a droplet formation system. For

the case of piezoelectric driven droplet formation from a short vibrating nozzle, the modeling of flow through the nozzle and the modeling of nozzle dynamic characteristics are also critical to the prediction of droplet formation.

Droplet formation from long rigid nozzle has been studied for a couple of years, and is well understood. But little is known for the droplet ejection from short vibrating nozzle. In this paper, droplet formation from a short vibrating nozzle was predicted numerically. Droplet formation from a short rigid nozzle was predicted also in order to make comparison with that from a vibrating nozzle.

The specific problem studied is droplet ejection from an ejector. The ejector is covered by vibration nozzle plate with a diameter of 8 mm. The nozzle is fixed at the center of nozzle plate and axisymmetric, has a diameter of $50\ \mu\text{m}$. The nozzle length is equal to the nozzle plate thickness, which varies between $16\ \mu\text{m}$ and $48\ \mu\text{m}$. A known pressure input is applied to the reservoir, driving fluid to form a droplet and the nozzle to vibrate. The pressure acting on the nozzle plate is assumed to be uniform in space and varies with time.

The focus of this study is to predict the nozzle vibration effect on DOD droplet formation. To achieve that, a one-dimensional droplet formation model coupled with a vibrating nozzle was formulated. The nozzle vibration magnitude can be set to be zero which corresponds to the rigid nozzle case. For the case of vibrating nozzle, nozzle vibration is predicted by solving the thin plate vibration equations, with an axisymmetric hole. DOD droplet formation from three different thickness vibration nozzle plates is considered to study the nozzle vibration effect on droplet

formation. The effects of fluid properties are studied by varying the fluid viscosity while keeping other properties the same as water.

2. LITERATURE REVIEW

Early in 1878, Rayleigh (1878) theoretically predicted droplet formation from a perturbed steady liquid jet. In the following one hundred years, research on droplet formation had been focused on continuous droplet formation from a steady liquid jet. Most of the ink-jet printing system developed prior 1970's were based on liquid jet instability, and thus consist a continuous liquid jet.

The burst of drop-on-demand technology in late 1970's led the droplet formation research to a new stage. This type of printing has the ability to produce a single droplet asynchronously on demand, which can not be well predicted by Raleigh theory. Many types of drop-on-demand ink-jet printer invented and developed in 1980s. Many experimental and numerical studies on the drop-on-demand droplet formation phenomenon were conducted since then. A good summary of development of ink-jet print technology and current commercially available printing systems is contained in Lee (1998).

2.1 DROP-ON-DEMAND DROPLET FORMATION IN INK-JET PRINTER

Drop-on-demand technology is being used widely in current printing systems. Drop-on-demand droplet formation process and the effect of various factors have been studied extensively by both experimental and numerical methods in the past two decades. Bogy et al (1984) experimentally studied the wave propagation in a drop-on-

demand ink-jet device. The device consist a long cylindrical channel with nozzle mounted on one end of the tube. The device was excited by piezoelectric cylinder over part of its length. Droplet formation process was observed under different pulsing pressure and tube length conditions. Results showed that the acoustic wave propagation has significant effect on the operation of this device.

Shield et al. (1987) experimentally studied the drop formation from long cylindrical channel, with a length to diameter ratio (l/d), of 20. An excited piezoelectric cylinder was used over a portion of its length which was driven by a square wave voltage input. Droplet formation of water and ethylene glycol were observed. Results showed that the primary droplet radius was in the order of the nozzle radius and varied slightly with the driving pressure input while the formation of satellite droplet and satellite droplet size were highly dependent on the pulsing pressure input. Results were compared with that simulated by using a one-dimensional model for droplet formation coupled with a one-dimensional model for acoustic pressure in the channel developed by Shield et al (1986). Comparison showed good agreement for most of the conditions. Further improvement of the model was recommended to model the physics accurately.

Hofer (1986) studied the droplet size modulation by multiple pressure pulsing input. His study showed that by controlling the time between two pressure pulses, the droplet size can be modulated. The interaction of multiple pressure pulses with meniscus surface causes multiple liquid jet protrusions. By proper control of the time

between pressure pulses, the multiple protrusions can merge into one droplet, by which the drop size can be modulated.

Burr et al. (1996) studied the surface oscillation mode effect on drop formation. His study showed that droplet size could be modulated by controlling the pulsing pressure input when the pulsing pressure has an energy concentration on a specific surface mode. The drop size can be reduced significantly if the energy concentrated on higher order surface modes. The experimental results showed good agreement with that from numerical simulation.

Chen et al. (2002, a) found the same trend as Burr (1996). Their result indicates that droplet size can be reduced significantly by changing the pressure input. Droplet radius can be reduced by a factor of two, while the droplet velocity is only reduced by a factor of 0.4.

2.2 NON-RIGID FLUID CHAMBER

Current models studying the acoustic wave transformation are based on a rigid fluid chamber. The chamber volume variation is small compared with the chamber size and thus usually neglected. The development of micro-ejector requires the chamber size is small and the chamber volume variation can not be neglected. Droplet formation from a non-rigid chamber becomes an interesting topic in recent years. Several micro-ejector designs based on vibrating plate had been published in the past few years.

Pan et al. (2002) studied the droplet ejection by a vibrating plate at the bottom of a chamber. His design used a thin chamber with rigid nozzle plate covered at the top. The vibrating plate at the bottom side was excited by a piezoelectric crystal. The deflection of plate was simulated by solving the plate vibration equation. Commercially available Flow-3D was used to study the fluid structure interactions. His study showed the feasibility of the micro-ejector using vibration membrane excited at back side.

Percin et al. (2003) designed a droplet ejector which can eject droplet from open reservoir. The chamber is open to atmosphere at the top and the nozzle is mounted on a vibrating nozzle plate at the bottom. The nozzle diameter is small and the fluid is held in the chamber by surface tension if there is no driving pressure input. The vibrating nozzle plate was excited directly by putting a piezoelectric crystal on it. His study showed the droplet ejection from the open reservoir depends on both the plate vibration characteristic and the capillary wave characteristic. Both numerical simulation and experimental results showed that droplet can be ejected from an open reservoir if the plate is driven at the proper frequency and proper vibration magnitude.

2.3 NUMERICAL MODELING OF DROPLET FORMATION

Numerical simulation of droplet formation is based on solving the Navier-Stokes equation with a moving free surface. Both three-dimensional models and one-

dimensional models are being used widely in recent years. Three-dimension models have wide applicability, while one-dimensional models are much simpler, less computation work, and reasonable accuracy. A good summary on the droplet formation dynamics and the numerical simulation is available in Eggers (1997).

Fromm (1982) presented a numerical simulation of drop-on-demand droplet formation from an axisymmetric rigid nozzle using a three-dimensional model and marker-and-cell front tracking technique. The fluid was considered as incompressible. He showed the feasibility of modeling droplet formation numerically.

Lee (1974) developed a one-dimensional model for droplet formation by assuming it to be axisymmetric and the liquid jet radius was much smaller compared with the jet length $r/l \ll 1$. He used the one-dimensional equation theoretically predicted the droplet formation from a perturbed steady liquid jet. He pointed out the possibility using a one-dimension model to simulate the droplet formation process. Numerical solution for the one-dimensional model was not succeeded until ten years later.

Using the one-dimensional model that Lee (1974) developed, Adams et al. (1984) succeeded the numerical simulation of droplet formation from axisymmetric nozzle. The MacCormack numerical scheme was used to solve his one-dimensional equation and a Lagrangian moving grid was used to track the moving free surface. He compared his results with that of Fromm (1982) who used a three-dimensional model. The results showed that the one-dimensional model performed well and by using the one-dimensional model the computation work was much reduced.

Yamamoto et al. (1995) using a one-dimensional model predicted the drop-on-demand droplet formation from a rigid nozzle, and compared with experimental results. The initial velocity from the nozzle was measured experimentally for each driving pressure. The initial velocity was used as a boundary condition in the numerical modeling. Results showed that the numerical model well predicted the droplet formation process, the primary droplet volume and the formation of satellites.

Eggers et al (1994) used a one-dimensional model to simulate droplet formation from a perturbed liquid jet and droplet formation from a dripping faucet. The numerical scheme taken by Eggers was weighted implicit method. The problem was mapped to a unit interval $z/l \in [0,1]$ to avoid using a moving grid. Results showed that the one-dimensional model could be applied to the cases where the liquid column radius in the same scale as the jet length, which was unexpected by Lee (1974) when he developed the one-dimensional model.

Wilkes et al (1999) studied dripping faucet by both three-dimensional and one-dimensional equation using the Galerkin finite element method. He pointed out the occurrence of the overturn phenomenon close to the break-off by three-dimensional model simulation, which can not be captured by the one-dimensional model. Close to the break-off singularity, the result using one-dimensional model differed with that of the three-dimensional model slightly. His model did not simulate the droplet movement after break-off occurs.

2.4 DROPLET BREAK-OFF PROCESS

The Navier-Stokes equations form a singularity at the break-off point, and viscosity has a strong effect on the time for the singularity to occur. The Navier-Stokes equations fail to simulate the phenomenon close the break-off, especially for low viscous fluids which the break-off occurs very quickly. Eggers (1993), using similarity theory, developed the “3/2 power law” scaling theory for describing the droplet break-off process. The theory was based the fact that close to the break-off point all external scale and boundary conditions are irrelevant. The break-off was governed by the “internal properties”, the surface tension force and viscous force. The time evolution of the liquid column near the break-off point can be predicted based on the time and distance to the break-off point by the “3/2 power law” scaling theory. The validation of the “3/2 power law” scaling theory was not done yet by that time.

Brenner et al. (1997) studied the droplet break-off phenomenon of water falling from a nozzle by one-dimensional numerical simulation and experimental methods. He compared the results with that predicted by “3/2 power law” scaling theory. The results predicted by the “3/2 power law” scaling theory agreed well with the numerical simulation within the time interval $10^{-3} - 10^{-1}t_c$ to break-off time, where t_c is the capillary time scale. Results showed that the minimum radius does not decrease monotonically, but increase for a while at time $10^{-3}t_c$. The maximum interface slope saturates to a constant value at same time.

Eggers (2000) studied the break-off of very low viscous liquid column, $Re/We = 5 \cdot 10^9$, by a one-dimensional simulation method. The numerical simulation showed that the interface slope reaches a maximum value, 10^4 , prior to droplet break-off. The minimum radius at the maximum slope reached 10^4 depended on the boundary conditions. The development of singularity predicted by “3/2 power law” theory agreed well with that predicted by the one-dimensional numerical simulation.

Day et al. (1998) studied the inviscid fluid break-off using three-dimensional simulation method. The three-dimensional equation was solved by using boundary-element method. Result showed that the overturn phenomenon and the break-off angle were independent on the initial conditions. The inviscid droplet break-off has a fixed cone shape. The cone angle is 18.1° for liquid thread and 112.8° for the droplet, measured from the axial direction. The inviscid fluid break-off shape was predicted by “3/2 power law” theory and a formulation of break-off shape was proposed.

Chen et al. (2002, b) studied the break-off of water and 83% glycerol in water. Three-dimensional numerical simulation and experimental study were constructed and compared with that predicted by “3/2 power law” theory. The overturn phenomenon was reported for water. The break-off shape from both numerical simulation and experimental agreed well with that the “3/2 power law” similarity solution. The “3/2 power law” theory deviated from simulation significantly for the 83% glycerol in water case. Results indicated the “3/2 power law” similarity solution adopted by Eggers (1993) was valid within the potential flow regime.

Papageorgiou (1995) studied the break-off of high viscous liquid threads by Stokes equation. Numerical simulation based on the one dimensional model and theoretical predictions based on the similarity solution were constructed. By Stokes equation, he developed the “1 power law” scaling theory for high viscous fluid break-off process. The numerical results showed good agreement with that predicted by “1 power law” scaling theory close to break-off occurs.

Lister et al. (1998) studied the break-off of viscous thread surrounded by another viscous fluid. Stokes equation and one-dimensional numerical method were used in his study. The surrounding fluid was assumed to have the same viscosity as the viscous liquid thread. Results showed that the thread minimum radius and location of minimum radius to pinch-off point develop linearly with time, the maximum velocity develop in a exponential form of time $t - t_0$, where t_0 is pinch-off time. The viscous thread break-off to a fixed cone shape, 5.9° cone angle for liquid thread and 112.8° cone angle for the droplet measured from the axial direction.

3. THEORETICAL DERIVATION

In this section, a one-dimensional equation for droplet formation from a vibrating nozzle is derived, together with a nozzle vibration dynamic equation for both small and large amplitude deflection. Plate vibration natural frequency and natural modes are analyzed by small amplitude deflection theory. Flow through the nozzle is modeled by inviscid assumption.

3.1 ONE-DIMENSIONAL DROPLET MODEL

The liquid jet dynamics is simulated by solving the one-dimensional Navier-Stokes equation. The one-dimensional model is adopted because of its simplicity, less computation effort, and expected to yield reasonable accurate results based on previous study in the literature. A schematic of motion and geometry of the liquid jet shape and the coordinates frame are shown in Figure 3.1.

Similar to the derivation of Lee (1974), the one-dimensional-model assumes that the variables depend only on the axial location but not the radial position. Several assumptions are made in developing the one-dimensional equations: 1) the liquid jet is axisymmetric along nozzle centerline, 2) there is no wetting effect between fluid and nozzle, 3) the working fluid is considered as Newtonian and incompressible, 4) no gravitational effect, 5) no friction force at air-fluid interface.

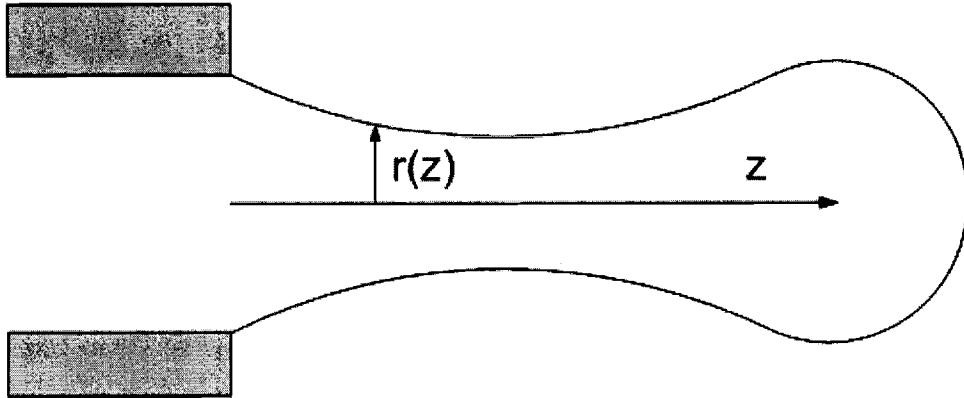


Figure 3.1: Schematic of liquid jet shape and the coordinate

The one-dimensional continuity equation can be written as:

$$\frac{\partial A}{\partial t} + \frac{\partial(A \cdot u)}{\partial z} = 0 \quad (3.1)$$

where u is the jet velocity, A is the liquid jet cross section area, $A = \pi \cdot r^2$, and r is the liquid jet radius. The one-dimensional momentum equation is written as:

$$\frac{\partial u}{\partial t} + u \cdot \frac{\partial u}{\partial z} = \frac{1}{\rho_l} \cdot \frac{\partial \sigma_z}{\partial z} \quad (3.2)$$

where σ_z is the axial normal stress, $\sigma_z = -p + 2 \cdot \mu \frac{\partial u}{\partial z}$, and p is the liquid jet pressure, μ is fluid dynamic viscosity, ρ_l is fluid density.

By Young-Laplace equation, Middleman (1995), the radial normal stress, σ_r ,

is:

$$\sigma_r = -p_a - \gamma \cdot \left(\frac{1}{K_N} + \frac{1}{K_T} \right) \quad (3.3)$$

where p_a is the surrounding ambient pressure, γ is the air-fluid interfacial surface tension, K_N, K_T are the principle radii of liquid jet curvature, defined as:

$$K_N = r \cdot \sqrt{1 + \left(\frac{\partial r}{\partial z} \right)^2} ; K_T = - \sqrt{\left[1 + \left(\frac{\partial r}{\partial z} \right)^2 \right]^3} / \left(\frac{\partial^2 r}{\partial z^2} \right) \quad (3.4)$$

Simplifying equations (3.1) through (3.3); results in the Lagrangian form of the one-dimensional liquid jet dynamic equations in a non-moving coordinate frame of reference:

$$\frac{dr}{dt} + \frac{r}{2} \cdot \frac{\partial u}{\partial z} = 0 \quad (3.5)$$

$$\frac{du}{dt} = -\frac{1}{\rho_l} \cdot \left[\frac{\partial}{\partial z} \left(\frac{1}{K_N} + \frac{1}{K_T} \right) - 3 \cdot \mu \cdot \frac{\partial^2 u}{\partial z^2} \right] \quad (3.6)$$

Boundary conditions for above continuity and momentum equations are a moving free surface at the liquid jet leading/trailing edge and no separation of liquid jet at nozzle. At the leading/trailing edge:

$$r = 0, z(t) = \int_0^t u(x) \cdot dx \quad (3.7)$$

At the nozzle outlet edge:

$$r = a, u = u_e \quad (3.8)$$

where $z(t)$ is the location of the leading/trailing edge, a is the nozzle radius, and u_e the fluid velocity at nozzle exit plane.

3.1.1 Effect of Nozzle Motion

The effect of nozzle movement effect on drop formation is accounted by defining a new coordinate frame which moves at same velocity with the nozzle. The

origin of the coordinate system is at the nozzle exit plane, $\eta = z - \int_0^t u_{nozzle}(x) \cdot dx$. The

liquid jet velocity in the new coordinate frame is:

$$u_\eta(\eta, t) = u(z, t) - u_{nozzle}(t) \quad (3.9)$$

where $u_\eta(\eta, t)$ is the liquid jet velocity relative to nozzle, and $u_{nozzle}(t)$ is the nozzle velocity. The liquid jet radius in the new coordinate is:

$$r_\eta(\eta, t) = r(z, t) \quad (3.10)$$

By adopting in the new coordinate system, the continuity and momentum equations become:

$$\frac{dr_\eta}{dt} + \frac{r_\eta}{2} \cdot \frac{\partial u_\eta}{\partial \eta} = 0 \quad (3.11)$$

$$\frac{du_\eta}{dt} = -\frac{1}{\rho_l} \cdot \left[\frac{\partial}{\partial \eta} \left(\frac{1}{K_N} + \frac{1}{K_T} \right) - 3 \cdot \mu \cdot \frac{\partial^2 u_\eta}{\partial \eta^2} \right] - \frac{du_{nozzle}}{dt} \quad (3.12)$$

3.1.2 Non-Dimensionalized Form

Equations (3.11) and (3.12) are non-dimensionalized in order to determine the parameters which affect the droplet formation. By defining a length scale, l_c , velocity scale, u_c , time scale, t_c , and pressure scale, p_c . The equations are non-dimensionalized by the capillary scales. The definitions of the capillary scales are:

$$l_c = a; \quad u_c = \sqrt{\frac{\gamma}{\rho_l \cdot a}}; \quad t_c = \sqrt{\frac{\rho_l \cdot a^3}{\gamma}}; \quad p_c = \gamma/a \quad (3.13)$$

The non-dimensional parameters are:

$$\eta^* = \eta/a; \quad t^* = t/t_c; \quad r_\eta^* = r_\eta/a; \quad u_\eta^* = u_\eta/u_c$$

$$u_{nozzle}^* = u_{nozzle}/u_c; \quad K_N^* = K_N/a; \quad K_T^* = K_T/a. \quad (3.14)$$

Substituting the non-dimensional parameters into the continuity and momentum equation results in:

$$\frac{dr_\eta^*}{dt^*} + \frac{r_\eta^*}{2} \cdot \frac{\partial u_\eta^*}{\partial \eta^*} = 0 \quad (3.15)$$

$$\frac{du_\eta^*}{dt^*} = - \left[\frac{\partial}{\partial \eta^*} \left(\frac{1}{K_N^*} + \frac{1}{K_T^*} \right) - 3 \cdot \frac{We}{Re} \cdot \frac{\partial^2 u_\eta^*}{\partial \eta^{*2}} \right] - \frac{du_{nozzle}^*}{dt^*} \quad (3.16)$$

where We/Re is defined as: $We/Re = \frac{\mu}{\sqrt{\rho_l \cdot a \cdot \gamma}}$. The principle radii equation (3.4) is

non-dimensionalized as:

$$K_N^* = r_\eta^* \cdot \sqrt{1 + \left(\frac{\partial r_\eta^*}{\partial \eta^*}\right)^2} ; K_T^* = - \sqrt{\left[1 + \left(\frac{\partial r_\eta^*}{\partial \eta^*}\right)^2\right]^3} / \left(\frac{\partial^2 r_\eta^*}{\partial \eta^{*2}}\right) \quad (3.17)$$

Equations (3.15) and (3.16) can be written in the form:

$$\frac{dX}{dt^*} + \frac{\partial Y}{\partial \eta^*} + Z = 0 \quad (3.18)$$

where X is the unknown variable, Y is the convection term, and Z is the acceleration term:

$$X = \left\{ \begin{array}{l} \ln(r_\eta^*) \\ u_\eta^* \end{array} \right\} ; Y = \left\{ \begin{array}{l} \frac{u_\eta^*}{2} \\ \left(\frac{1}{K_N^*} + \frac{1}{K_T^*}\right) + 3 \cdot \frac{We}{Re} \cdot \frac{\partial u_\eta^*}{\partial \eta^*} \end{array} \right\} ; Z = \left\{ \begin{array}{l} 0 \\ \frac{\partial u_{nozzle}^*}{\partial t^*} \end{array} \right\} \quad (3.19)$$

3.2 EARLY STAGE DROPLET FORMATION MODEL

The one-dimensional model can be applied only when a liquid jet has left the nozzle for a fixed distance. Assumptions for describing the early stages of liquid jet leaving from a nozzle are required. The one-dimensional model is applied when the liquid jet tip has moved a fixed distance, L , from nozzle exit plane, taken to be nozzle radius, $L = a$.

In this early stage a spherical liquid jet shape is assumed, such that the liquid jet pressure is uniform. The liquid jet tip velocity is calculated by mass conservation based on the velocity at the nozzle exit plane. A schematic of liquid jet shape in the early stage is shown in figure 3.2.

The spherical shape assumption results in:

$$R^2 - (R - L)^2 = a^2 \quad (3.20)$$

where R is the sphere radius, L is the liquid tip location, and a is the nozzle radius.

By equation (3.20), the sphere radius is:

$$R = \frac{1}{2} \cdot \left(L + \frac{a^2}{L} \right) \quad (3.21)$$

The pressure in the liquid jet, a result of the surface tension effect, during the early stage is:

$$p = \frac{2 \cdot \gamma}{R} \quad (3.22)$$

Equations (3.21) and (3.22) give the relation between liquid jet tip location and internal pressure as:

$$p = \frac{4 \cdot \gamma}{L} \cdot \frac{L^2}{L^2 + a^2} \quad (3.23)$$

The volume of the liquid jet in the early stage, V , is:

$$V = \pi \cdot \left(\frac{L \cdot a^2}{2} + \frac{L^3}{6} \right) \quad (3.24)$$

By mass conservation:

$$\frac{d}{dt}(V) = \pi \cdot a^2 \cdot u_e \quad (3.25)$$

where u_e is the time dependent fluid velocity at nozzle exit plane which is defined in the next section.

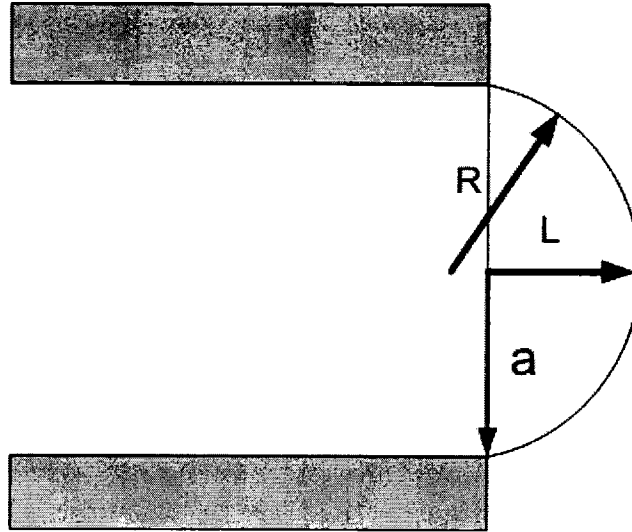


Figure 3.2: Schematic of liquid jet shapes in initial stage

By equations (3.24) and (3.25), the relationship between fluid velocity at nozzle exit

plane and the liquid tip velocity, $u_t = \frac{dL}{dt}$, is:

$$u_e = \left(\frac{a^2}{2} + \frac{L^2}{2} \right) \cdot u_t \quad (3.26)$$

Equations (3.23) and (3.26) are non-dimensionalized by the scales defined in equation

(3.13), as:

$$p_e^* = \frac{4}{L^*} \cdot \frac{L^{*2}}{L^{*2} + 1} \quad (3.27)$$

$$u_e^* = \left(\frac{1}{2} + \frac{L^{*2}}{2} \right) \cdot u_t^* \quad (3.28)$$

3.3 MODELLING NOZZLE FLOW

Since the known boundary condition is the pressure inside the chamber, a model for the nozzle flow dynamics is necessary in order to determine the velocity history at the nozzle exit plane which is a boundary condition for the liquid jet simulation. Since the nozzle length, h , is very short, the ratio of nozzle length to nozzle radius $h/a \ll 1$, entrance effects on the nozzle flow dynamics is significant. In order to model flow out of the nozzle, following assumptions are made: 1) fluid is Newtonian and incompressible; 2) the wall viscous layer is small compared with nozzle radius, so nozzle flow is plug flow, 3) there is no minor pressure change by sudden contraction and expansion, and 4) the fluid completely fills the nozzle.

By the above assumptions, the viscous effect is neglected. The momentum equation for nozzle flow is:

$$\rho_l \cdot \frac{du}{dt} = - \frac{dp}{dz} \Big|_e \quad (3.29)$$

The continuity equation is:

$$\frac{du}{dz} = 0 \quad (3.30)$$

From equations (3.25) and (3.26), the nozzle flow velocity follows:

$$\rho_l \cdot \frac{du_e(t)}{dt} = \frac{p_0(t) - p_e(t)}{h} \quad (3.31)$$

where p_0 is the applied driving pressure, p_e is the pressure at the nozzle exit plane determined by surface tension, h is the nozzle length, and u_e is the nozzle exit plane velocity.

Equation (3.31) is non-dimensionalized by the scales defined by equation (3.13), results in:

$$h^* = h/a; t^* = t/t_c; p_0^* = P_0/p_c; u_e^* = u_e/u_c \quad (3.32)$$

Substituting the non-dimensional parameters into equation (3.31) results in the non-dimensional nozzle flow dynamics equation:

$$\frac{du_e^*}{dt^*} = \frac{p_0^* - p_e^*}{h^*} \quad (3.33)$$

3.4 NOZZLE VIBRATION DYNAMICS

The circular nozzle is fixed at the center of a uniform thickness plate. Vibration dynamics of the plate was studied in order to model the vibration dynamics of nozzle. Thin plate theory is used since the nozzle plate diameter to thickness ratio $\frac{d}{h}$ in the order of 200, far larger than 20, the criterion to be classified as a thin plate.

The large deflection plate vibration equation is solved to study the plate vibration character, while the plate natural frequencies and natural modes are analyzed by small deflection plate vibration equation for its simplicity. The effect of the nozzle opening on the natural frequency and natural modes are neglected since hole's size is small,

$a/d = 0.00125$. The difference between large and small deflection plate vibration is based on the plate vibration magnitude, w , relative to the thickness, h . For small magnitude, $\frac{w}{h} \leq 0.2$, Airy stress is small and thus neglected. For large magnitude,

$\frac{w}{h} \geq 0.5$ the airy stress can not be neglected.

3.4.1 Natural Frequency of Plate Vibration

The small deflection plate natural vibration equation is given by Rao (1999):

$$\nabla^4 w + \frac{\rho_p \cdot h}{D} \cdot \frac{\partial^2 w}{\partial t^2} + \frac{C}{D} \cdot \frac{\partial w}{\partial t} = 0 \quad (3.34)$$

where ρ_p is plate density, C is damping factor of the vibration, D is the bending

rigidity, $D = \frac{E \cdot h^3}{12 \cdot (1 - \nu^2)}$, E is Young's modulus, and ν is Poisson ratio.

The boundary conditions are axial symmetric, finite deflection amplitude at the center and clamped edge, which are expected as. At $r = r_o$:

$$w = 0, \quad \frac{\partial w}{\partial r} = 0 \quad (3.35)$$

At $r = 0$:

$$w \ll Inf, \quad \frac{\partial w}{\partial r} = 0 \quad (3.36)$$

where r_o is plate radius.

Using separation of variables, assuming $w(r,t) = \mathfrak{R}(r) \cdot \mathfrak{S}(t)$, where $\mathfrak{R}(r)$ is a radial dependent function, $\mathfrak{S}(t)$ is a time dependent function, and substituting into equation (3.34) yields:

$$\frac{1}{\mathfrak{S}(t)} \cdot \left[\frac{\rho_p \cdot h}{D} \cdot \frac{d^2 \mathfrak{S}(t)}{dt^2} + \frac{C}{D} \cdot \frac{d \mathfrak{S}(t)}{dt} \right] = -\frac{\nabla^4 \mathfrak{R}(r)}{\mathfrak{R}(r)} = -\beta^4 \quad (3.37)$$

where β is a real constant. The general solution for this equation is:

$$\mathfrak{R}(r) = c1 \cdot J_0(\beta \cdot r) + c2 \cdot Y_0(\beta \cdot r) + c3 \cdot I_0(\beta \cdot r) + c4 \cdot K_0(\beta \cdot r) \quad (3.38)$$

where J_0 , Y_0 are Bessel functions of the first kind, I_0 , K_0 are modified Bessel functions of the first kind, and $c1$, $c2$, $c3$, and $c4$ are arbitrary constants. Substituting the boundary conditions of equations (3.35) and (3.36) into equation (3.38) yields:

$$J_0(\beta \cdot d) \cdot I_1(\beta \cdot d) + J_1(\beta \cdot d) \cdot I_0(\beta \cdot d) = 0 \quad (3.39)$$

The first six roots of equation (3.39) are listed in table 3.1

Solving equation (3.37) results in the plate natural frequencies:

$$f_n = \frac{1}{2 \cdot \pi} \cdot \left(\frac{\kappa_n}{d} \right)^2 \cdot \sqrt{\frac{E \cdot h^2}{12 \cdot (1 - \nu^2) \cdot \rho_p}} \cdot \sqrt{1 - \frac{1}{4} \cdot \frac{E \cdot h^2}{12 \cdot (1 - \nu^2) \cdot \rho_p} \cdot \left(\frac{C}{\rho_p \cdot h} \right)^2} \quad (3.40)$$

where f_n is the nth natural frequency and $\kappa_n = \beta_n \cdot d / 2$ are constant values dependent on the boundary condition. The natural frequency shift caused by damping

$$\text{is } \sqrt{1 - \frac{1}{4} \cdot \frac{E \cdot h^2}{12 \cdot (1 - \nu^2) \cdot \rho_p} \cdot \left(\frac{C}{\rho_p \cdot h} \right)^2}.$$

Table 3.1
Roots to equation (3.39), mode numbers 1 through 6

n	$\kappa_n = \beta_n \cdot d$
1	3.1961
2	6.3064
3	9.4395
4	12.577
5	15.716
6	18.857

When $\frac{1}{4} \cdot \frac{E \cdot h^2}{12 \cdot (1 - \nu^2) \cdot \rho_p} \cdot \left(\frac{C}{\rho_p \cdot h} \right)^2 = 1$ results in critical damping, for which

no plate natural oscillation exist. The case $\frac{1}{4} \cdot \frac{E \cdot h^2}{12 \cdot (1 - \nu^2) \cdot \rho_p} \cdot \left(\frac{C}{\rho_p \cdot h} \right)^2 > 1$ is over-

damped and no natural frequency exists.

3.4.2 Natural Mode of Plate Vibration

After substituting in the boundary conditions, the mode shape function equation (3.38) becomes:

$$\mathfrak{R}_n(r) = \frac{c1}{I_0(\beta_n \cdot d)} \cdot (I_0(\beta_n \cdot d) \cdot J_0(\beta_n \cdot r) + J_0(\beta_n \cdot d) \cdot I_0(\beta_n \cdot r)) \quad (3.41)$$

The modal shape function equation (3.41) is orthogonalized by defining:

$$\iint_A \rho_p \cdot h \cdot \mathfrak{R}_i(r) \cdot \mathfrak{R}_j(r) \cdot dA = \delta_{ij} \quad (3.42)$$

where δ_{ij} is the Kronecker delta, $\delta_{ij} = 1$ when $i = j$, and $\delta_{ij} = 0$ when $i \neq j$.

Apply the orthogonal equation (3.42) to mode shape functions equation (3.41)

results in the orthogonal mode shape functions:

$$\mathfrak{R}_n(r) = \frac{1}{d} \cdot \sqrt{\frac{1}{2 \cdot \pi \cdot \rho_p \cdot h}} \cdot \left(\frac{I_0\left(\kappa_n \cdot \frac{r}{d}\right)}{I_0(\kappa_n)} - \frac{J_0\left(\kappa_n \cdot \frac{r}{d}\right)}{J_0(\kappa_n)} \right) \quad (3.43)$$

When the orthogonal mode shape functions are normalized by $\frac{1}{d} \cdot \sqrt{\frac{1}{2 \cdot \pi \cdot \rho_p \cdot h}}$. The

normalized orthogonal mode shape functions $\mathfrak{R}_n^*(r)$ results:

$$\mathfrak{R}_n^*(r) = \left(\frac{I_0\left(\kappa_n \cdot \frac{r}{d}\right)}{I_0(\kappa_n)} - \frac{J_0\left(\kappa_n \cdot \frac{r}{d}\right)}{J_0(\kappa_n)} \right) \quad (3.44)$$

Figure 3.3 shows the first six orthogonal mode shapes.

3.4.3 Forced Plate Vibration

The forced plate vibration equation based on small deflection theory is:

$$\nabla^4 w + \frac{\rho_p \cdot h}{D} \cdot \frac{\partial^2 w}{\partial t^2} + \frac{C}{D} \cdot \frac{\partial w}{\partial t} = P_0 \quad (3.45)$$

The boundary condition for a clamped edge plate is: At $r = r_o$:

$$w = 0, \frac{\partial w}{\partial r} = 0 \quad (3.46)$$

At $r = 0$:

$$\frac{\partial w}{\partial r} = 0, w \ll Inf \quad (3.47)$$

In obtaining a numerical solution, the boundary condition $w \ll Inf$ is difficult to implement. By analyzing $\nabla^4 w + \frac{\rho_p \cdot h}{D} \cdot \frac{\partial^2 w}{\partial t^2} + \frac{C}{D} \cdot \frac{\partial w}{\partial t} = p_0$ another boundary condition results: At $r = 0$:

$$\frac{\partial^3 w}{\partial r^3} = 0 \quad (3.48)$$

The plate vibration dynamics equation is non-dimensionalized by the same scales equation (3.13), results in:

$$w^* = w/a; h^* = h/a; r^* = r/a; t^* = t/t_c; \rho^* = \rho_p/\rho_t$$

$$p_0^* = p_0/p_c; E^* = E/p_c; D^* = \frac{E^* \cdot h^{*3}}{12 \cdot (1-\nu^2)}; C^* = \frac{C \cdot a}{t_c \cdot p_c}. \quad (3.49)$$

Substituting the non-dimensional parameters back into equation (3.45) results in the non-dimensional plate vibration equation:

$$\nabla^4 w^* + \frac{\rho^* \cdot h^*}{D^*} \cdot \frac{\partial^2 w^*}{\partial t^{*2}} + \frac{C^*}{D^*} \cdot \frac{\partial w^*}{\partial t^*} = \frac{p_0^*}{D^*} \quad (3.50)$$

$$\text{where } \nabla^4 = \frac{\partial^4}{\partial r^{*4}} + \frac{2}{r^*} \frac{\partial^3}{\partial r^{*3}} - \frac{1}{r^{*2}} \frac{\partial^2}{\partial r^{*2}} + \frac{1}{r^{*3}} \frac{\partial}{\partial r^*}$$

The boundary condition equations (3.46), (3.47), and (3.48) are non-dimensionalized by the scales in equation (3.13) also. The non-dimensionalized boundary conditions are: At $r^* = r_o^*$:

$$w^* = 0; \frac{\partial w^*}{\partial r^*} = 0 \quad (3.51)$$

At $r^* = 0$:

$$\frac{\partial w^*}{\partial r^*} = 0; \quad \frac{\partial^3 w^*}{\partial r^{*3}} = 0 \quad (3.52)$$

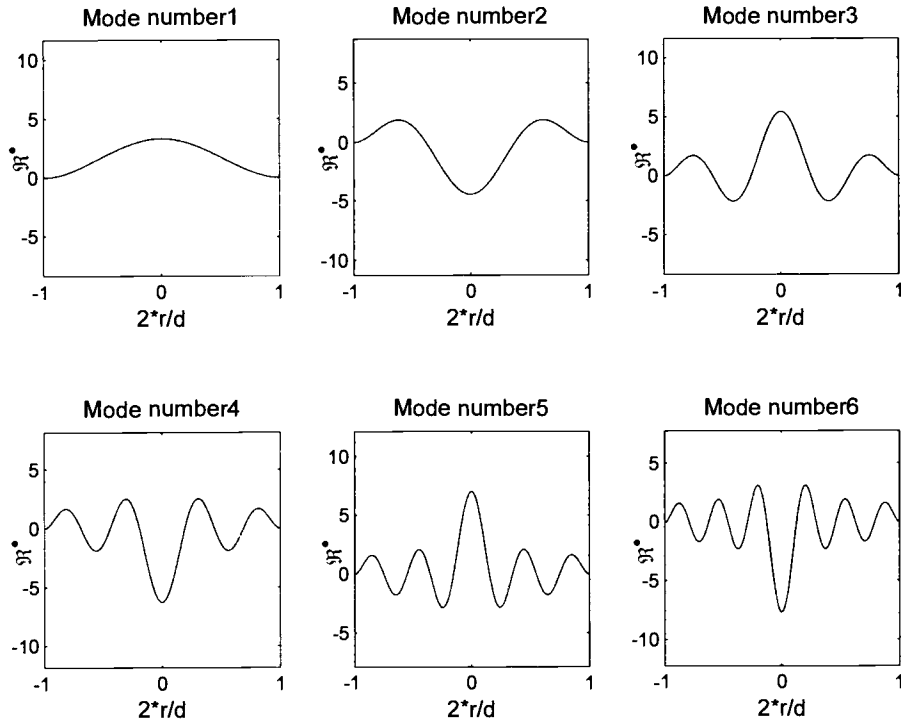


Figure 3.3: Plate free vibration normalized orthogonal mode shapes for clamped edge boundary condition; mode numbers 1 through 6

3.4.4 Hole Effect on Plate Vibration Dynamics

For the numerical solution, hole's effect is considered by defining the free edge boundary condition at the hole edge. The boundary conditions for axisymmetric plate vibration equation with a circular hole at center are: At $r = d/2$, (clamped edge boundary):

$$w = 0; \frac{\partial w}{\partial r} = 0 \quad (3.53)$$

At $r = a$, (free edge boundary):

$$\frac{\partial^3 w}{\partial r^3} + \frac{1}{r} \cdot \frac{\partial^2 w}{\partial r^2} - \frac{1}{r^2} \cdot \frac{\partial w}{\partial r} = 0; \quad \frac{\partial^2 w}{\partial r^2} + \frac{\nu}{r} \cdot \frac{\partial w}{\partial r} = 0 \quad (3.54)$$

Equations (3.53) and (3.54) are non-dimensionalized by scales equation (3.13), the non-dimensional boundary conditions are: At $r^* = d^*/2$:

$$w^* = 0; \frac{\partial w^*}{\partial r^*} = 0 \quad (3.55)$$

At $r^* = 1$:

$$\frac{\partial^3 w^*}{\partial r^{*3}} + \frac{1}{r^*} \cdot \frac{\partial^2 w^*}{\partial r^{*2}} - \frac{1}{r^{*2}} \cdot \frac{\partial w^*}{\partial r^*} = 0; \quad \frac{\partial^2 w^*}{\partial r^{*2}} + \frac{\nu}{r^*} \cdot \frac{\partial w^*}{\partial r^*} = 0 \quad (3.56)$$

3.4.5 Forced Plate Vibration by Large Deflection Theory

Since the pressure required to form a droplet from a small orifice is very high, the plate deflection magnitude likely falls into the large deflection range. Large deflection plate vibration needs to be considered when the ratio between the plate

deflection magnitude and plate thickness $\frac{w}{h} \geq 0.5$. The vibration dynamics by large

deflection theory is given by Szilard (1974):

$$D \cdot \nabla^4 w + \rho_p \cdot h \cdot \frac{\partial^2 w}{\partial t^2} + C \cdot \frac{\partial w}{\partial t} = h \cdot \frac{1}{r} \frac{\partial}{\partial r} \left(\frac{\partial w}{\partial r} \cdot \frac{dF}{dr} \right) + p_0 \quad (3.57)$$

$$\nabla^4 F = -\frac{E}{r} \cdot \frac{\partial w}{\partial r} \cdot \frac{\partial^2 w}{\partial r^2} \quad (3.58)$$

where F is airy stress function, which defines the in plane stress due to large magnitude plate deflection. For small deflection, the plate in plane stretch is small and thus neglected.

Sangrut (2003) studied the numerical solution to equation (3.57) and (3.58) by an approximation method. Equation (3.57) and (3.58) are non-dimensionalized by the scales defined in equation (3.13) and airy stress scale defined as:

$$F_c = \gamma \cdot a \quad (3.59)$$

By which define the non-dimensional parameters:

$$w^* = w/a; h^* = h/a; r^* = r/a; t^* = t/t_c; p_0^* = p_0/p_c; E^* = E/p_c$$

$$D^* = \frac{E^* \cdot h^{*3}}{12 \cdot (1 - \nu^2)}; F^* = F/F_c; C^* = \frac{C \cdot a}{t_c \cdot p_c}; \rho^* = \rho_p/\rho_l \quad (3.60)$$

Substituting the non-dimensional parameters back into equations (3.57) and (3.58)

results in the non-dimensional plate vibration equations:

$$\nabla^4 w^* + \frac{\rho_p^* \cdot h^*}{D^*} \cdot \frac{\partial^2 w^*}{\partial t^{*2}} + \frac{C^*}{D^*} \cdot \frac{\partial w^*}{\partial t^*} = \frac{h^*}{D^*} \cdot \frac{1}{r^*} \frac{\partial}{\partial r^*} \left(\frac{\partial w^*}{\partial r^*} \cdot \frac{dF^*}{dr^*} \right) + \frac{p_0^*}{D^*} \quad (3.61)$$

$$\nabla^4 F^* = -\frac{E^*}{r^*} \cdot \frac{\partial w^*}{\partial r^*} \cdot \frac{\partial^2 w^*}{\partial r^{*2}} \quad (3.62)$$

where $\nabla^4 = \frac{\partial^4}{\partial r^{*4}} + \frac{2}{r^*} \frac{\partial^3}{\partial r^{*3}} - \frac{1}{r^{*2}} \frac{\partial^2}{\partial r^{*2}} + \frac{1}{r^{*3}} \frac{\partial}{\partial r^*}$, with the plate radius is non-dimensional as $r^* = r/a$

3.4.6 Parametric Study on Plate Vibration Characteristic

The plate vibration frequency and plate bending rigidity is studied parametrically in order to predict the different plate vibration effects on droplet formation. Non-dimensionalizing the plate vibration natural frequency equation (3.40) by the scales in equation (3.13), results in the plate natural frequency parametric:

$$f_1^* = \frac{1}{2 \cdot \pi} \cdot \left(\frac{32 \cdot a}{d} \right)^2 \cdot \sqrt{\frac{E \cdot h^2 \cdot \rho_l}{12 \cdot (1 - \nu^2) \cdot a \cdot \gamma \cdot \rho_p}} \cdot \sqrt{1 - \frac{E \cdot h^2}{48 \cdot (1 - \nu^2) \cdot \rho_p} \cdot \left(\frac{C}{\rho_p \cdot h} \right)^2} \quad (3.63)$$

For plate static deflection of a given load P, has the deflection

magnitude $\frac{w_o}{h} = \frac{d^4}{64 \cdot D \cdot h} \cdot \frac{\gamma}{a} \cdot \frac{p}{\gamma/a}$; where w_o is the center deflection magnitude.

Define the plate bending rigidity parametric as:

$$D^* = \frac{64 \cdot D \cdot h}{d^4} \cdot \frac{\gamma}{a} \quad (3.64)$$

The plate bending rigidity parameter reflects the plate deflection magnitude relative to the plate thickness, while the plate natural frequency parameter can be used to predict the nozzle vibration period relative to the droplet break-off time.

4. NUMERICAL CODING

Finite difference method is used to integrate the modeling equations. Figure 4.1 shows the relationship between the equations. Prediction-correction type time integration spatial center differencing method is used to achieve second order accuracy in both time and space. Details about the numerical schemes are presented first, the stability analysis second, sample convergence of solution third, and the validation of coding fourth.

4.1 NUMERICAL SCHEMES

An explicit prediction-correction type numerical method is used in solving the finite difference equations. Approximate solution of the large deflection plate vibration equation by Sangrut (2003) is used in solving the large deflection equation for getting nozzle vibration characteristic.

4.1.1 Early Stage Modeling

With known pressure boundary condition at nozzle inlet plane, the nozzle flow dynamic equation (3.33) and early stage assumption equation (3.28) are solved to model the liquid jet formation in early stage. For known information at time step, the algorithm is:

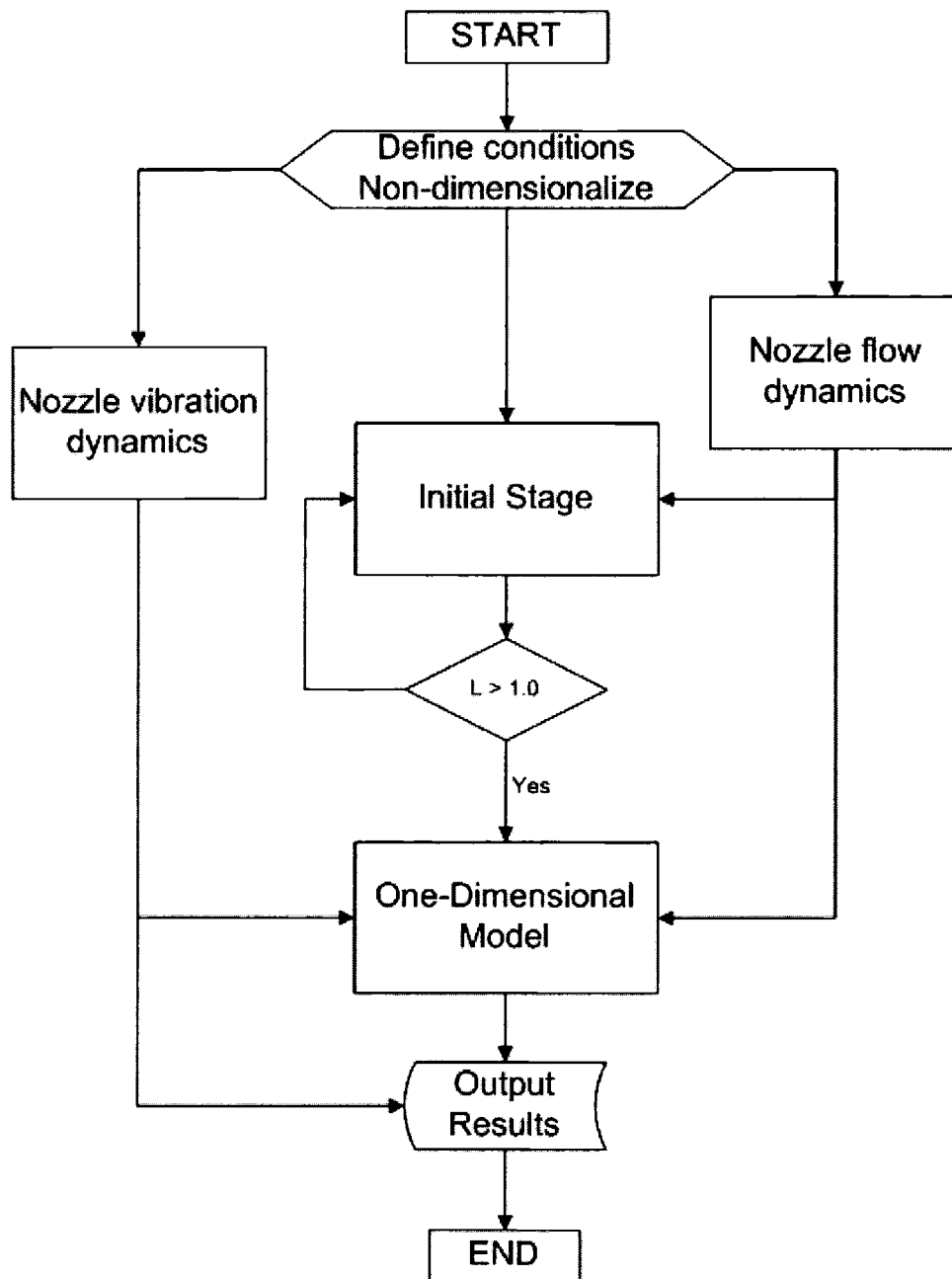


Figure 4.1: Relationship of each part of the model

Prediction of the tip location is by:

$$L^{*n+1/2} = L^{*n} + u_t^{*n} \cdot \Delta t^* / 2 \quad (4.1)$$

where the superscript n denotes the time step number, time step number + 1/2 denotes predicted value for time step n+1. Evaluation of the pressure at nozzle exit plane is by Equation (3.27):

$$p^{*n+1/2} = \frac{4}{L^{*n+1/2}} \cdot \frac{L^{*n+1/2}}{\left(L^{*n+1/2}\right)^2 + 1} \quad (4.2)$$

Calculation of the nozzle exit velocity by nozzle flow dynamic Equation (3.33):

$$u_e^{*n+1} = u_e^{*n} + \Delta t^* \cdot \frac{\left(p_0^{*n+1} + p_0^{*n}\right)/2 - p_e^{*n+1/2}}{h^*} \quad (4.3)$$

Calculation of the liquid jet tip velocity is from:

$$u_t^{*n+1} = u_e^{*n+1} \cdot \frac{2}{1 + \left(L^{*n+1/2}\right)^2} \quad (4.4)$$

Calculate liquid jet tip location at time step n + 1:

$$L^{*n+1} = L^{*n} + \Delta t^* \cdot \left(u_t^{*n} + u_t^{*n+1}\right) / 2 \quad (4.5)$$

Above numerical scheme is used in modeling droplet formation in the early stage $L^{*n+1} \leq 1.0$.

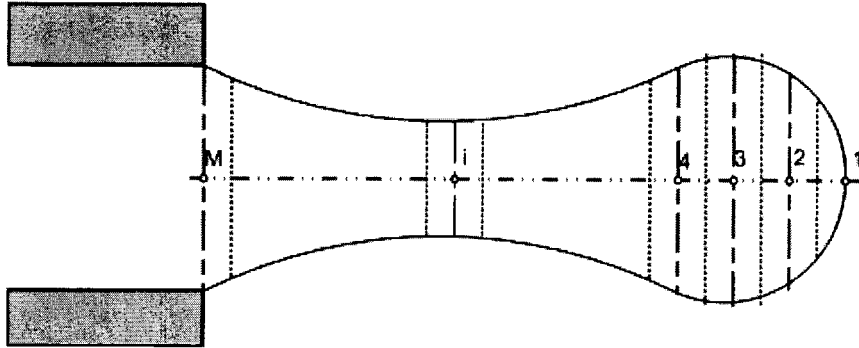


Figure 4.2: Numbering sequence of nodes

4.1.2 One-Dimensional Modeling

The liquid jet is divided into M uniform elements and the FDE solution of the one-dimensional equation is adopted once the criterion $L^{*n+1} \geq 1.0$ is satisfied. The numbering sequence of the elements is shown in figure 4.2.

Time integration of the one-dimensional equations (3.19) is solved numerically in modeling the droplet formation. The integral form of equation (3.19) from time step n to time step $n+1$ can be written as:

$$X^{n+1} - X^n = - \int_{t^{*n}}^{t^{*n+1}} \frac{\partial Y}{\partial \eta^*} \cdot dt^* - \int_{t^{*n}}^{t^{*n+1}} Z \cdot dt^* \quad (4.6)$$

According to equation (3.17), the time integration of nozzle effect term G is:

$$\int_{t^{*n}}^{t^{*n+1}} Z \cdot dt^* = H^{n+1} - H^n \quad (4.7)$$

$$\text{where } H = \begin{Bmatrix} 0 \\ u_{nozzle}^* \end{Bmatrix} \quad (4.8)$$

Explicit prediction-correction type MacCormack method is used in doing time integration of the convection term F .

$$\delta X_i^{n+1/2} = -\delta t^* \cdot \frac{Y_{i+1}^n - Y_i^n}{\eta_{i+1}^n - \eta_i^n} \quad (4.9)$$

$$\delta X_i^{n+1} = -\delta t^* \cdot \frac{Y_{i-1}^{n+1/2} - Y_i^{n+1/2}}{\eta_{i+1}^n - \eta_i^n} \quad (4.10)$$

where $Y_i^{n+1/2}$ terms in equation (4.9) are evaluated based on the predicted value of $X_i^{n+1/2}$. The predicted value of $X_i^{n+1/2}$ is calculated by:

$$X_i^{n+1/2} = X_i^n + \delta X_i^{n+1/2} \quad (4.11)$$

Value of X_i at next time step, $n+1$, is:

$$X_i^{n+1} = X_i^n + \frac{1}{2} \cdot (\delta X_i^{n+1/2} + \delta X_i^{n+1}) - H^{n+1} + H^n \quad (4.12)$$

Above numerical scheme can be applied only to the interior nodes, node 1 through M-1. The boundary nodes, 1st node and number M node, are treated as:

For the nozzle exit plane, M node: Non-dimensional radius kept to be one all the time:

$$r_M^* = 1 \quad (4.13)$$

Non-dimensional velocity is treated as:

$$u_M^{*n+1/2} = u_M^{*n} \quad (4.14)$$

$$u_e^{*n+1} = u_e^{*n} + \delta t^* \cdot \frac{(p_0^{*n+1} + p_0^{*n})/2 - p_e^{*n+\frac{1}{2}}}{h^*} \quad (4.15)$$

where equation (4.15) provides the boundary condition for the prediction time step, and equation (4.16) is the boundary velocity for the correction time step.

For leading edge node, 1st node: Non-dimensional radius kept to be zero all the time:

$$r_1^* = 0 \quad (4.16)$$

Non-dimensional velocity is treated by linear extrapolation from neighbor elements:

$$u_1^* = u_2^* + (\eta_1^* - \eta_2^*) \cdot (u_3^* - u_2^*) / (\eta_3^* - \eta_2^*) \quad (4.17)$$

The trailing edge node, after break-off occurs, is treated by the same method as leading edge node.

The nodal positions are held fixed until the calculation is completed for a given time step, n, and then updated. The position is updated by center differencing approximation method:

$$\eta_i^{*n+1} = \eta_i^{*n} + \frac{1}{2} \cdot \delta t^* \cdot (u_i^{*n} + u_i^{*n+1}) \quad (4.18)$$

By Langrangian moving grid method, the spatial grid will spread or contract, which lead to non-uniform grid size. For fixed time step size, the contraction will possibly lead to unstable solution, while spreading should be avoided in order to get good spatial resolution. Node are added or deleted to maintain nearly uniform special grid size.

The criteria for adding/deleting nodes are: Adding nodes:

$$\eta_i^* - \eta_{i-1}^* \geq 1.6 \cdot \delta\eta^* \quad (4.19)$$

Deleting nodes:

$$\eta_i^* - \eta_{i-1}^* \leq 0.6 \cdot \delta\eta^* \quad (4.20)$$

where $\delta\eta^*$ is the spatial grid size controlled.

Linear extrapolation is adopted when nodes need to added, by which has:

$$\eta_l^* = (\eta_i^* + \eta_{i-1}^*)/2 ; r_l^* = (r_i^* + r_{i-1}^*)/2 ; u_l^* = (u_i^* + u_{i-1}^*)/2 \quad (4.21)$$

where η_l^* , r_l^* , u_l^* are the position, radius, and velocity of added nodes between node i and $i-1$. When the criteria for deleting node, $\eta_i^* - \eta_{i-1}^* \leq 0.6 \cdot \delta\eta^*$, is satisfied, the front node, node number $i-1$ is deleted. The numbering of nodes is reordered according to $\eta_{i-1}^* > \eta_i^* > \eta_{i+1}^*$ whenever node is added or deleted.

4.1.3 Nozzle Vibration Modeling

Nozzle vibration dynamic modeling is based on solving the large plate vibration equation. The large deflection plate vibration equation, Equations (3.57) and (3.58) are solved by spatial mode shape approximation method and time integration by Runge-Kuta method. Details about the method solving the plate vibration equation method referred to Sangrut (2003).

4.1.4 Droplet Break-off

Proper definition is essential in simulating droplet break-off process. Since the one-dimensional model can not simulate the overturn phenomenon, the definition of break-off avoid the development of infinite gradient singularity while let the simulation close enough to the zero radius singularity. The overturn phenomenon is defined as at some axial position, the liquid radius has more than one value. For one-dimensional model the element is defined as the axial position and each element has only one radius value, thus one-dimensional model can not catch the overturn phenomenon. The overturn phenomenon is a very common in droplet formation and results from fluid properties and driving pressure input. Two criteria are chosen to define the break-off, threshold of minimum radius and threshold of maximum gradient. The definition of break-off is either of the two criteria being satisfied. The threshold minimum radius chosen is 0.001 of the nozzle radius, while the maximum gradient chosen is maximum gradient resolvable by the spatial grid size based on spherical shape with unit radius. The threshold maximum gradient is selected to prevent the failure of simulation due to occurrence of overturn phenomenon.

The definition of threshold is based on the maximum resolvable gradient by FDE method for a sphere with a unit radius. An illustration of the threshold gradient calculation is shown in figure 4.3. In figure 4.3, node numbered as 0 is the tip node. The center differencing numerical scheme can be applied to the first node, numbered as 1. The gradient of sphere at position of the first node is taken as the threshold

gradient in the one-dimensional model. The threshold gradient can be calculated approximately by equation:

$$\left. \frac{dr^*}{d\eta^*} \right|_{\max} = \sqrt{\frac{2}{\delta\eta^*}} \quad (4.22)$$

where $\delta\eta^*$ is the spatial grid size taken at the end of initial stage.

For a typical non-dimensional spatial grid size of 0.005, the gradient threshold is taken to be 20. Numerical experiment shows that overturn phenomenon can be avoided by taking the threshold gradient defined by equation (4.22). The break-off criteria are listed in table 4.1. The break-off is defined as that either one of the two criteria is satisfied.

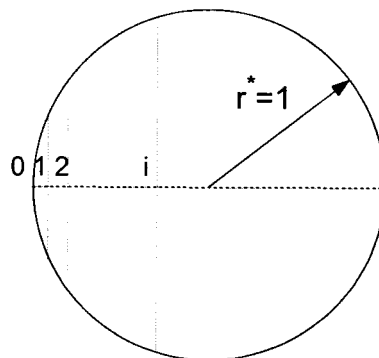


Figure 4.3 Threshold gradient calculations

Table 4.1
Break-off criteria

Criteria	Non-dimensional Value
Minimum threshold radius: r_{\min}^*	0.001
Maximum threshold gradient: $dr^*/d\eta^* _{\max}$	$\sqrt{2/\delta\eta^*}$

The liquid jet is defined to break-off at the position of minimum radius if the minimum radius criterion is satisfied, while the break-off position is defined by spherical shape intersection based on the maximum gradient curvature radii. Free movement of break-off droplet and the formation of satellite from the liquid filament are simulated also. In order to simulate the free movement of break-off droplet and the formation of satellite, the method of the liquid column break-off is required to be defined also.

The definition of liquid column break-off shape is dependent on the break-off criteria being satisfied. If the minimum threshold radius is satisfied, the break-off shape is simply setting the minimum radius to be zero. The front part is defined as the primary droplet and the part attached to the nozzle exit plane is defined as the liquid filament. If the maximum threshold gradient is satisfied, the break-off shapes for the primary droplet and the liquid filament are defined separately. The primary droplet trailing edge part is defined by spherical rounding; the radius taken for the rounding is defined as the curvature radius at the maximum gradient node. The liquid filament is defined by linear extrapolation from the minimum radius node to a point where a zero

radius reached. The extrapolated shape is defined as the liquid filament shape and the zero radius position is defined as the leading edge node of the liquid filament. An illustration figure shown the definition of break-off shape is shown in figure 4.4.

The free movement of break-off droplet and the evolution of the liquid filament are simulated starting from the break-off shape. The threshold gradient of the free moving droplet is defined as twice the threshold gradient considered for the one-dimensional modeling. The increment of threshold gradient limitation for free droplet movement simulation is to prevent the program being stopped by the high gradient at leading/trailing edge of the droplet due to bouncing of the free moving droplet. The simulation of the free movement of primary droplet is stopped when the droplet has left the nozzle 50 times the radius of nozzle. The simulation of the liquid filament is stopped when the liquid filament break-off again.

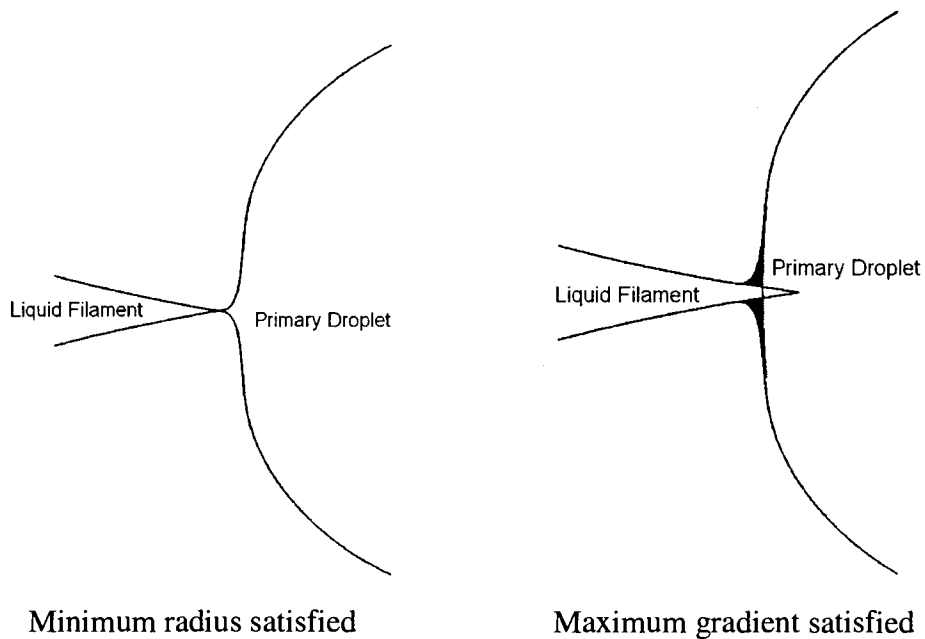


Figure 4.4 Liquid column break-off shapes by different break-off criteria

4.2 STABILITY ANALYSIS

Von-Neumann stability analysis is performed for the one-dimensional model equation. The nozzle plate vibration equation is unconditionally stable, details about the nozzle plate vibration stability issue is referred to Sangrut (2003).

The one-dimensional equation is highly non-linear, and the von-Neumann stability analysis by the FDE is very lengthy and tedious. The two issues related to the one-dimensional equation stability are the capillary wave and viscous diffusion. The stability analysis is much simplified by analyzing the capillary wave stability

requirement and viscous diffusion stability requirement separately. Numerical experimental shows that the solution is stable if both of these two criteria satisfied.

4.2.1 Capillary Wave Stability Requirement

The capillary wave stability requirement can be obtained by analyzing the one-dimensional mass conservation equation. By the FDE of mass conservation:

For the prediction time step:

$$r_i^{*n+1/2} = r_i^{*n} + \frac{\delta^*}{\delta\eta_{i,i+1}^*} \cdot r_i^{*n} \cdot (u_{i+1}^{*n} - u_i^{*n}) \quad (4.23)$$

For the correction time step:

$$r_i^{*n+1} = r_i^{*n} + \frac{1}{2} \cdot \frac{\delta^*}{\delta\eta_{i,i+1}^*} \cdot r_i^{*n} \cdot (u_{i+1}^{*n} - u_i^{*n}) - \frac{1}{2} \cdot \frac{\delta^*}{\delta\eta_{i,i-1}^*} \cdot r_i^{*n+1/2} \cdot (u_{i-1}^{*n+1/2} - u_i^{*n+1/2}) \quad (4.24)$$

where $\delta\eta_{i,i+1}^* = \eta_i^* - \eta_{i+1}^*$ $\delta\eta_{i,i-1}^* = \eta_{i-1}^* - \eta_i^*$.

For Von-Neumann stability, consider the solution of the form:

$$r_i^{*n} = \hat{\phi}^n(k) \cdot e^{i \cdot k \cdot \eta_i^*}; \quad u_i^{*n} = \hat{\psi}^n(k) \cdot e^{i \cdot k \cdot \eta_i} \quad (4.25)$$

$$r_i^{*n+1/2} = \hat{\phi}^{n+1/2}(k) \cdot e^{i \cdot k \cdot \eta_i}; \quad u_i^{*n+1/2} = \hat{\psi}^{n+1/2}(k) \cdot e^{i \cdot k \cdot \eta_i} \quad (4.26)$$

where k is wave number

Substitute equation (4.25) into equation (4.23) results in:

$$\hat{\phi}^{n+1/2}(k) = \hat{\phi}^n(k) \cdot \left[1 + \frac{1}{2} \cdot \frac{\delta^*}{\delta\eta_{i,i+1}^*} \cdot \hat{\psi}^n(k) \cdot \left(e^{i k \delta\eta_{i,i+1}^*} - 1 \right) \right] \quad (4.27)$$

$$\text{Define: } G^n(k) = \left[1 + \frac{1}{2} \cdot \frac{\delta^*}{\delta\eta_{i,i+1}^*} \cdot \hat{\psi}^n(k) \cdot \left(e^{i k \delta\eta_{i,i+1}^*} - 1 \right) \right] \quad (4.28)$$

Substitute equation (4.25), (4.26), (4.28) into equation (4.24) results in:

$$\hat{\phi}^{n+1}(k) = \hat{\phi}^n(k) \cdot \left[\frac{1}{2} + \frac{1}{2} \cdot G^n(k) - \frac{1}{4} \cdot G^n(k) \cdot \frac{\delta \alpha^*}{\delta \eta_{i,i-1}^*} \cdot \psi^{n+1/2} \cdot \left(e^{-ik\delta \eta_{i,i-1}^*} - 1 \right) \right] \quad (4.29)$$

$$G^{*n} = \left[\frac{1}{2} + \frac{1}{2} \cdot G^n(k) - \frac{1}{4} \cdot G^n(k) \cdot \frac{\delta \alpha^*}{\delta \eta_{i,i-1}^*} \cdot \psi^{n+1/2} \cdot \left(e^{-ik\delta \eta_{i,i-1}^*} - 1 \right) \right] \quad (4.30)$$

where $G^n(k)$, and $G^{*n}(k)$ are the radius amplification factor for prediction time step and correction time step.

The solution is stable if both the amplification factor for prediction step $G^n(k)$ and the amplification factor for correction step $G^{*n}(k)$ are less than one. A complex graph show:

$$-2 \leq \left(e^{ik\delta \eta^*} - 1 \right) \leq 0, \text{ and } -2 \leq \left(e^{-ik\delta \eta^*} - 1 \right) \leq 0 \quad (4.31)$$

By equation (4.27), (4.29), and (4.30) get, the stability is satisfied if:

$$\hat{\psi}^{n+1/2}(k) \cdot \frac{\delta \alpha^*}{\delta \eta_{i,i-1}^*} \leq \frac{1}{2}, \text{ and } \hat{\psi}^n(k) \cdot \frac{\delta \alpha^*}{\delta \eta_{i,i+1}^*} \leq \frac{1}{2} \quad (4.32)$$

Define: $\delta \eta^* = \min(\delta \eta_{i,i+1})$ is the minimum grid size, and

$\hat{\psi}(k) = \max(\hat{\psi}_i^n(k), \psi_i^{n+1/2}(k))$ is the maximum wave speed. The capillary wave

stability requirement is:

$$\hat{\psi}(k) \cdot \frac{\delta \alpha^*}{\delta \eta^*} \leq \frac{1}{2} \quad (4.33)$$

The non-dimensional speed of capillary waves is given by Foote (1973):

$$c = \sqrt{\frac{2 \cdot \pi}{\lambda}} \quad (4.34)$$

where λ is the non-dimensional capillary wave length.

The smaller wave length corresponds to the higher wave speed. The smallest resolvable non-dimensional wave length is $\lambda = 2 \cdot \delta\eta^*$. The highest wave speed resolvable is $\sqrt{\frac{\pi}{\delta\eta^*}}$. Substitute to equation (4.33) get the capillary wave stability

criteria is:

$$\frac{\alpha^*}{(\delta\eta^*)^{3/2}} \leq \frac{1}{2} \cdot \frac{1}{\sqrt{\pi}} \quad (4.35)$$

4.2.2 Viscous Diffusion Stability Requirement

The viscous diffusion stability requirement can be obtained by analyzing the one-dimensional viscous diffusion momentum equation. The stability analysis is performed by using same grid size to avoid the lengthy derivations. Consider the solution is in the form of equation (4.25), (4.26). By the FDE get the velocity for the prediction time step due to viscous effect is:

$$\hat{\psi}^{n+1/2}(k) = \hat{\psi}^n(k) \cdot \left[1 - \frac{3}{2} \cdot \frac{We}{Re} \cdot \frac{\alpha^*}{(\delta\eta^*)^2} \cdot (1 - e^{ik\delta\eta^*}) \cdot (e^{-ik\delta\eta^*} - e^{ik\delta\eta^*}) \right] \quad (4.36)$$

$$\text{Define: } Q^n(k) = \left[1 - \frac{3}{2} \cdot \frac{We}{Re} \cdot \frac{\alpha^*}{(\delta\eta^*)^2} \cdot (1 - e^{ik\delta\eta^*}) \cdot (e^{-ik\delta\eta^*} - e^{ik\delta\eta^*}) \right] \quad (4.37)$$

$$\bar{Q}^n(k) = \left[1 - \frac{3}{2} \cdot \frac{We}{Re} \cdot \frac{\alpha^*}{(\delta\eta^*)^2} \cdot (1 - e^{-ik\delta\eta^*}) \cdot (e^{-ik\delta\eta^*} - e^{ik\delta\eta^*}) \right] \quad (4.38)$$

For the correction step has:

$$\hat{\psi}^{n+1}(k) = \hat{\psi}^n(k) \cdot \left[\frac{1}{2} + \frac{1}{2} \cdot Q^n(k) \cdot Q^{*n}(k) \right] \quad (4.39)$$

The amplification factor for the correction step is:

$$Q^{*n}(k) = \left[\frac{1}{2} + \frac{1}{2} \cdot Q^n(k) \cdot \bar{Q}^n(k) \right] \quad (4.40)$$

where $Q^n(k)$ and $Q^{*n}(k)$ are the velocity amplification factor for the prediction time step and the correction time step respectively.

A complex graph:

$$0 \leq \left(1 - e^{ik\delta\eta^*} \right) \cdot \left(e^{ik\delta\eta^*} - e^{-ik\delta\eta^*} \right) \leq 2 \cdot \sqrt{2} \quad (4.41)$$

$$0 \leq \left(1 - e^{-ik\delta\eta^*} \right) \cdot \left(e^{ik\delta\eta^*} - e^{-ik\delta\eta^*} \right) \leq 2 \cdot \sqrt{2} \quad (4.42)$$

Equation (4.37), (4.39), (4.41) and (4.42) results in the viscous diffusion stability requirement, as:

$$\frac{3}{2} \cdot \frac{We}{Re} \cdot \frac{\delta^*}{(\delta\eta^*)^2} \cdot 2 \cdot \sqrt{2} < 1 \quad (4.43)$$

For fixed grid step, the time step requirement for stability can be easily derived from equation (4.35) and (4.43), the time step is:

$$\delta^* < \min \left[\frac{\sqrt{2}}{6} \cdot \frac{Re}{We} \cdot (\delta\eta^*)^2, \frac{1}{2 \cdot \sqrt{\pi}} \cdot (\delta\eta^*)^{3/2} \right] \quad (4.44)$$

4.3 NUMERICAL CONVERGED SOLUTION

The convergence of the above numerical scheme is proved by simulating drop formation process for a sample pressure boundary condition based on different grid size. The driving pressure, which is chosen to show the convergence, is a pulse function with non-dimensional pressure magnitude of ten and non-dimensional pulse time width 0.15. The driving pressure is shown in figure 4.5.

The selection of convergence is based the break-off information. It is believed that as the simulation converged to a fixed break-off phenomenon, the intermediate phenomenon leading to droplet break-off should converge to a fixed solution also. The convergence criteria selected is the droplet break-off shape. Figure 4.6 shows the break-off shapes from different grid size. In order to get comparable results, the simulation is stopped when the maximum gradient reaches a gradient threshold, the maximum resolvable gradient based on the largest spatial grid size, 0.1. The slight difference of break-off and break-off length between different grid sizes partially comes from the resolution of maximum gradient.

Figure 4.6 shows the break-off shape converged to a fixed shape as the grid refined. The grid size taken for other cases simulation is 0.1/16, which refined the initial grid size by a factor of 16, consider the accuracy and computation time.

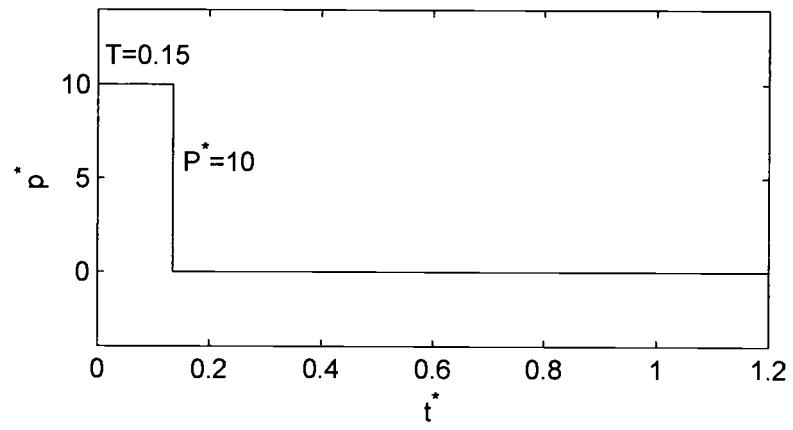


Figure 4.5: Sample driving pressure for showing convergence of the code

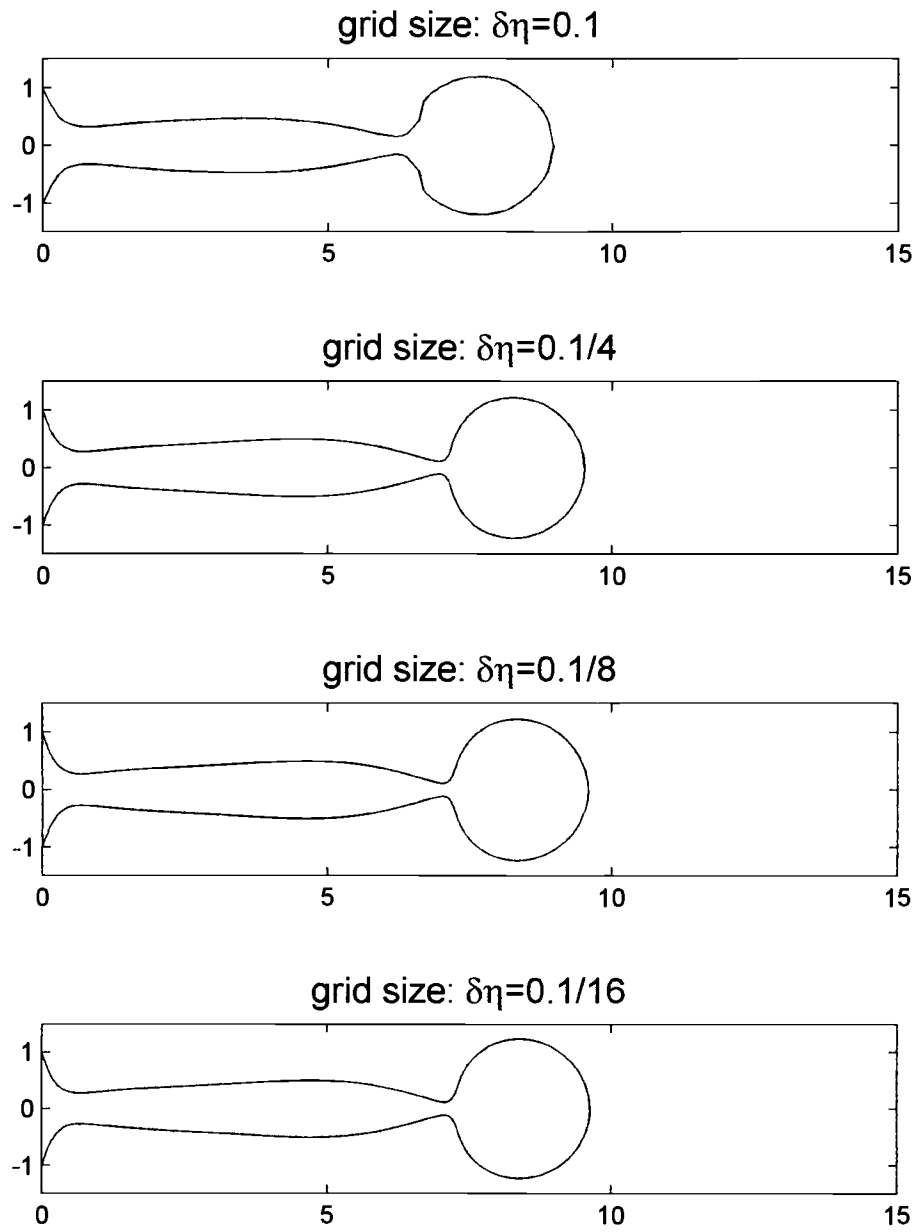


Figure 4.6: Sample droplet break-off shape by different grid size

4.4 UNCERTAINTY

The uncertainty of the numerical scheme can be obtained from the sample case showing the convergence. An important issue related to the uncertainty is the parameters chosen to check the accuracy. The condition chosen for uncertainty analysis is the break-off shape defined by the coarsest grid size. The parameters chosen are the primary droplet break-off time, t_d^* , the primary droplet break-off length, l_d^* , the liquid column tip length at break-off, l_t^* , the liquid column minimum radius at break-off, r_{\min}^* , and volume content of the liquid column at break-off, V^* .

Uncertainty values are calculated based on four different grid sizes mentioned previously. Of these an average and standard deviation were determined. Table 4.2 shows of the parameters being chosen, that the uncertainty is within 3%. So the numerical scheme is accurate enough to make a good prediction. The uncertainty is due to the different truncation errors resulting from the selected grid sizes.

Table 4.2
Uncertainty analysis of the numerical scheme

	Average	Standard Deviation	Percentage Error (%)
Break-off time: t_d^*	3.4979	0.0223	0.639
Break-off length: l_d^*	7.001	0.0776	1.108
Break-off Tip length: l_t^*	9.5844	0.0767	0.801
Break-off minimum radius: r_{\min}^*	0.1128	0.0033	2.917
Break-off Volume: V_d^*	11.355	0.0441	0.388

4.5 VALIDATION OF CODING

Because of a lack of results to compare for droplet formation from a vibrating nozzle, the coding for droplet formation and nozzle vibration dynamics are validated separately. The integrated code, which is the integration of above two part codes, is believed to be valid. Validation of droplet formation from a rigid nozzle is compared to results published by other researcher, while the validation of nozzle vibration dynamics is referred to Sangrut (2003).

4.5.1 Validation of One-Dimensional Drop Formation Coding

The validation of coding is compared with the dripping water faucet case, Eggers (1994). His result has been compared with experimental results of Peregrine (1990) at the time of droplet detaches from a liquid column. Table 4.3 shows the dimensional parameters used by Eggers (1994). The dimensional parameters are non-dimensionalized by the scales equation (3.13), the non-dimensional parameters are used as the input in the coding to make the sure the simulation are based on the same condition. The resulted non-dimensional parameters are shown in table 4.4. Figure 4.7 shows the simulation time history of dripping faucet and the comparison with that of Eggers (1994). The non-dimensional time between profiles is 0.4, the same as Eggers, starting from a point of drop has begun falling. In Eggers simulation, an experimental picture (1990) is superimposed at the time of droplet detach from the nozzle.

Table 4.3
Dimensional parameters of Eggers (1994) used for validation

Dimensional parameters	Values
Nozzle radius: a (mm)	2.6
Fluid kinematical viscosity: ν (mm^2 / sec)	1.00
Fluid-air interface surface tension: γ (kg / sec^2)	0.0728
Fluid density: ρ (kg / m^3)	998.6
Fluid average velocity out of nozzle: u (m/sec)	0.003349
Gravity acceleration: g (m / sec^2)	9.8

Note: Velocity is calculated by $u = 0.02 \cdot \frac{\gamma}{(\rho \cdot \sqrt{a})}$ as indicated in the paper.

Table 4.4
Non-dimensional parameters for coding validation

Non-Dimensional parameters	Eggers
Re/We:	435.37
Bo:	0.908726
Inlet Re:	8.714

The good agreement between Egger simulation and current simulation confirms that the coding is validated for the part of prior a droplet break-off. The part of coding for droplet free movement simulation and the liquid filament is not validated since currently there is no experimental results to compare. It is reasonable

to assume that the part of coding for simulating free droplet movement and filament movement is valid since the numerical algorithm used as the same as the part validated.

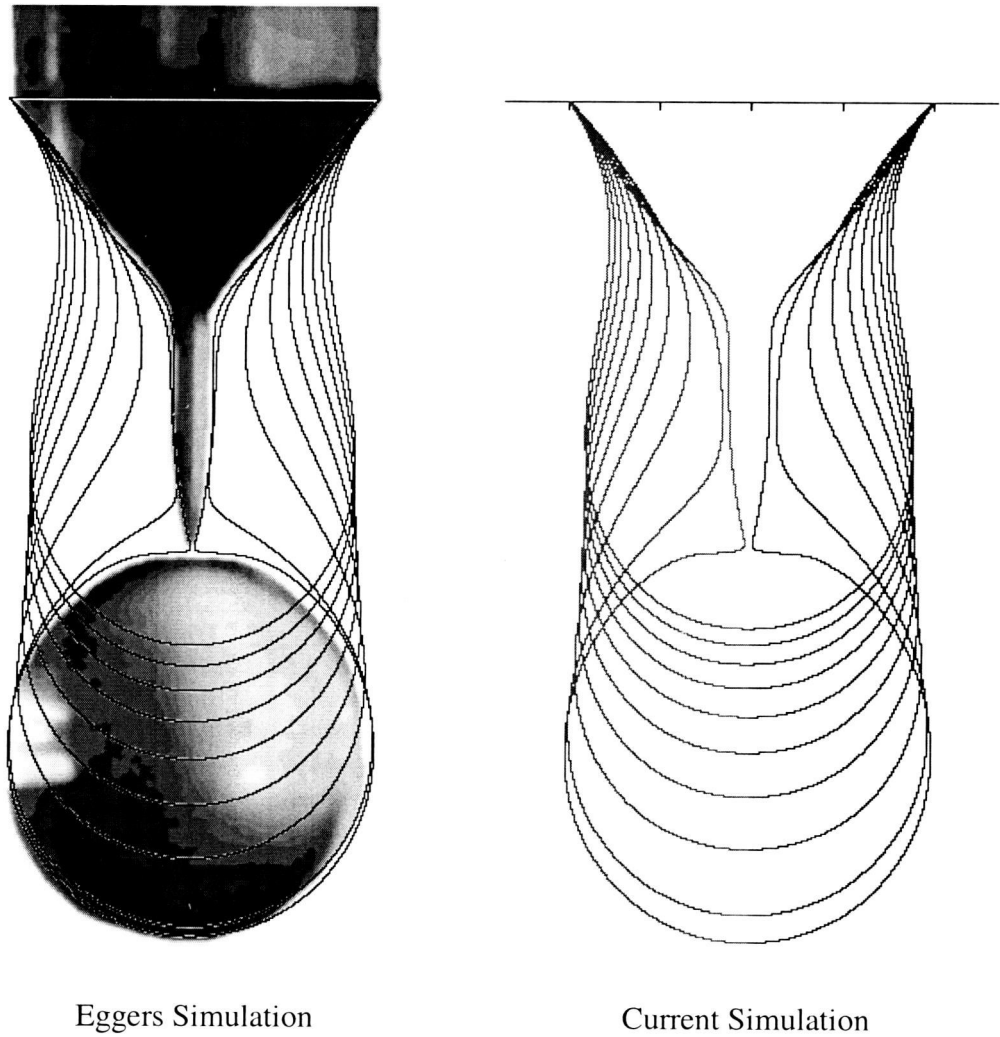


Figure 4.7: Dripping water simulation comparison with that of Eggers

5. DATA ANALYSIS

5.1 TEST CONDITIONS

The test conditions are based on the geometric setup of the test device to be used for future study by. Fluid is consider as water initially, and the viscous effect on drop formation is studied by varying the fluid viscosity while keep all other properties the same as water. Three different plates are considered to study the effect of different nozzle vibration characteristics on droplet formation.

5.1.1 The Capillary Scales

The capillary scales, used to nondimensionalize the problem, are based on the nozzle radius, density of water, and the air-water interface surface tension. The nozzle radius is referred to the nozzle plate used by Siresha (2003). The density of water and the air-water interface surface tension are referred to Munson (1990). The dimensional parameters are listed in Table 5.1, and the resulted capillary scales are listed in Table 5.2.

Table 5.1
Dimensional parameters chosen for capillary scales calculation

Nozzle Radius: a (μm)	50
Water density: ρ_l (kg/m^3)	998.2
Air-Water surface tension: γ (kg/s^2)	0.0728

Table 5.2
The resulting capillary scales

Length scale: l_c (μm)	50
Time scale: t_c (μs)	41.40
Velocity scale: u_c (m/s)	1.208
Pressure scale: p_c (Pa)	1456

5.1.2 Fluids Considered

Five different fluids are considered to study viscous effect on drop formation, by changing the viscosity while keeping all other properties the same as water. Water viscosity is referred to Munson (1990), the dynamic viscosity of water is $\mu = 1.002 \times 10^{-3} \text{ kg/m}\cdot\text{s}$ fluid viscosity is varied by multiply the water viscosity by a factor from 1—12. The five different fluid viscosities adopted in this simulation and the corresponding Re/We number are shown in Table 5.3.

Table 5.3
Fluids studied

Fluid Number	Fluid dynamic viscosity / Water dynamics viscosity	Re/We
1	1	60
2	2	30
3	4	15
4	6	10
5	12	5

5.1.3 Nozzle Plates Considered

Droplet formation from both rigid and vibration nozzle plate are simulated to study nozzle vibration effect on droplet formation. The nozzle radius and nozzle plate radius are fixed, nozzle radius $a = 50\mu m$, nozzle plate radius $d/2 = 4mm$. The rigid nozzle plate thickness is fixed $h = 16\mu m$. Three different thicknesses are selected for vibrating nozzle plate cases, by changing the plate thickness. The properties of the plate materials, are given by Less EMF Inc (2003), and are shown in table 5.4. Different nozzle plates studied are listed in Table 5.5. The plate non-dimensional first mode natural vibration frequencies and non-dimensional stiffness, defined by equations (3.63) and (3.64), are listed in Table 5.6.

Table 5.4
Nozzle plate properties

Density: ρ_p (kg/m^3)	7590
Young's modulus: E (Gpa)	102
Poisson ratio: ν	0.35

Table 5.5
Nozzle plates studied

Plate Number	Application	Plate Thickness (μm)
1	Rigid	16
2	Vibration	16
3		32
4		48

Table 5.6
Nozzle plates non-dimensional first mode natural frequency
and stiffness parameter

Plate Number	Plate natural frequency f^*	Plate stiffness D^*
2	0.076316	0.003574
3	0.152631	0.457477
4	0.228947	7.816428

5.1.4 Driving Pressures Considered

The driving pressure applied to form droplets is a pulsing pressure function with different pressure magnitude and pulse times. Single pulse is selected for its widely application to drop-on-demand droplet formation.

The non-dimensional driving pressure function is shown in Figure 5.1, units are arbitrary. The positive pressure is initiated at time equal to zero. Twelve different driving pressure pulses are studied, by the combination of three different driving pressure magnitudes and four different pulsing times. The pressure magnitude, P^* , and pulse times, T^* , are selected to have the thrust inputs, $P^* \cdot T^*$, for each pressure magnitude selected to have the same range of values from 1.0—2.5. The non-dimensional pressure magnitudes, the non-dimensional pressure pulsing times corresponding to each pressure magnitude and the resulting non-dimensional thrust inputs are shown in table 5.7.

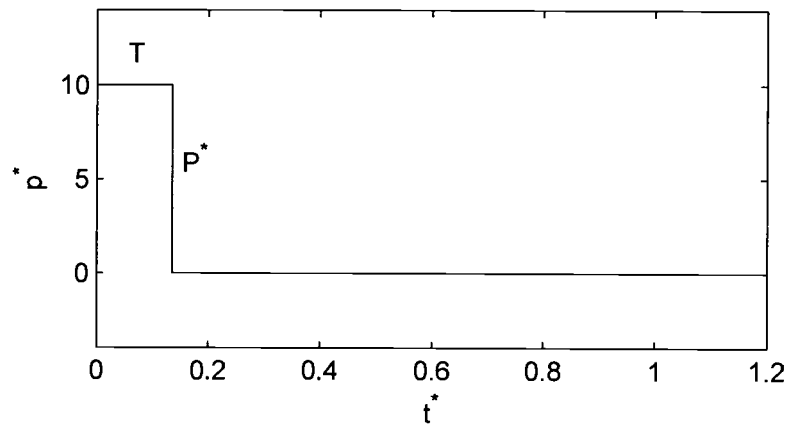


Figure 5.1: Pressure function studied with arbitrary units

Table 5.7
Driving pressure input

Pressure number	Pressure magnitude: P^*	Pulse width: T^*	Thrust input: $P^* \cdot T^*$
1	10	0.1	1.0
2	10	0.12	1.2
3	10	0.15	1.5
4	10	0.2	2.0
5	5	0.2	1.0
6	5	0.24	1.2
7	5	0.3	1.5
8	5	0.4	2.0
9	2.5	0.2	1.0
10	2.5	0.48	1.2
11	2.5	0.6	1.5
12	2.5	0.8	2.0

5.2 DATA PROCESSING

Four data output files from the numerical coding are generated, (i) elements radius, (ii) elements position, (ii) elements velocity, and (iv) elements pressure. Each file generated is a 2-dimensional matrix, with the rows and columns representing the elements values and the output time. A fifth file recording the nozzle deflection is generated. The fifth file is two vectors, containing the nozzle deflection magnitude and nozzle deflection velocity at each output time. The non-dimensional time between output data files is $\delta t^* = 0.1$, starting from time equal to zero. A specific data set output is added at the time of half hemisphere begins to form and whenever the break-off criterion is satisfied. The program is stopped when the break-off criteria is satisfied at the second time, which is when the filament and droplet both break-off from the nozzle. The selection of output file format makes the output file within reasonable size while catching all important information regarding the droplet formation process. The output data files are loaded to MATLAB. Data are processed to obtain the time series plot of droplet formation history, to detect the break-off, and to study the effect of various factors on the droplet formation.

5.2.1 Time Series Droplet Formation

Time series plot is a straight forward method to show the droplet formation process. A two-dimensional time series liquid shape plot is constructed by plotting

the fluid shapes at different time in time series order. The time series plot is constructed by the MATLAB program 'timeseriesplot.m'.

The 'timeseriesplot.m' program works by loading the elements radius file and the elements position file. Define the elements position as x-axis and the elements radius as y-axis. The elements are connected linearly to obtain the liquid shapes. Time series plots are constructed by plot the liquid shapes in the same figure in a time series order. A sample case is shown in the results chapter while all other time series plots are attached in the appendix due to the high number of cases studied.

5.2.2 Primary/Satellite Break-off Detection

Break-off is an important parameter for droplet formation. A lot of information can be studied from the droplet break-off, like droplet formation time, primary droplet size and primary droplet velocity. Two break-offs are defined, the primary break-off and the satellite break-off. The primary break-off is defined as the break-off of primary droplet from other liquid segments, while the satellite break-off is defined as the liquid filament break-off from the nozzle near the nozzle exit plane. The definition of satellite break-off is void in case of droplet formation without satellite forms. The definition of primary droplet, satellite droplet, primary break-off position, and satellite break-off position is shown in figure 5.2.

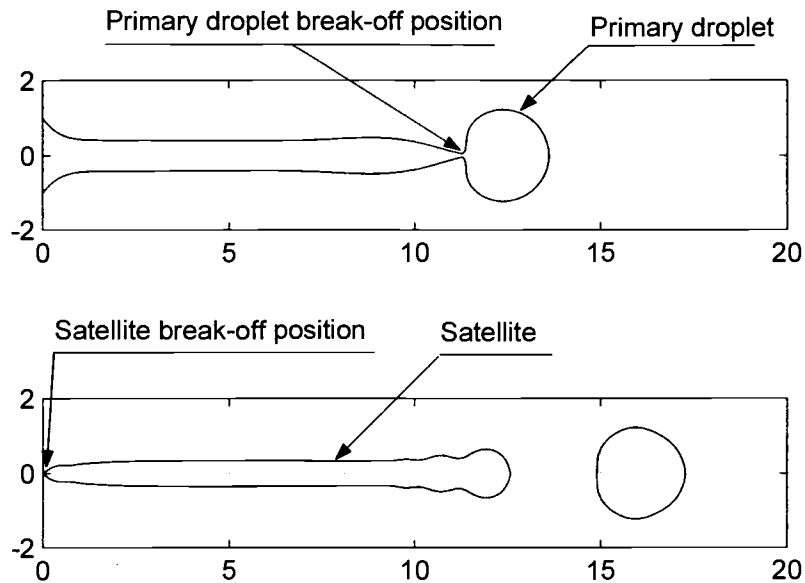


Figure 5.2: Definition of primary droplet, satellite droplet, primary break-off position, and satellite break-off position; all units are nondimensionalized by the capillary scales

The break-off shape plots is constructed to study different parametric effects on droplet formation. The break-off shapes of all the cases studied for each parametric study are plotted in the same figure to make comparisons. The break-off shape is defined as the liquid shape when the break-off criterion is first satisfied. The break-off shape is the liquid shape relative to the nozzle exit plane. The MATLAB program 'breakoffshapessave.m' can detect the liquid shapes when break-off shapes are first satisfied and saves the liquid shape data at the break-off as '*.mat' file. Another MATLAB program 'breakoffshapeplot.m' loads the break-off shape files, '*.mat', of the cases studied and plot the break-off shapes in the same figure.

The primary droplet formation time and the satellite droplet formation time is constructed to study the effects of various factors on droplet break-off time. The primary droplet break-off time is defined as the time when the primary break-off occurs. Similarly the satellite droplet break-off time is defined as the time when the satellite break-off occurs. Once the primary break-off and the satellite break-off is detected, the primary droplet break-off time and the satellite droplet break-off time can be detected easily from the data output file rows recording the break-off shape.

The primary break-off length is an important parameter to study the break-off, while the satellite break-off length is important to study flow dynamics at nozzle exit plane. The primary break-off length and the satellite break-off length is defined as the primary droplet and the satellite droplet break-off position relative to the nozzle exit plane. The MATLAB program 'breakofflength.m' can detect the primary break-off length and the satellite break-off length. By comparing the break-off shape with the break-off criterion, the element satisfying the break-off criterion can be detected. The primary/satellite break-off position and the primary/satellite break-off length can be detected once the element match the break-off criteria is detected.

The volume of the primary droplet and the satellite droplet is used in evaluating the primary and satellite droplet size. In the simulation, the non-dimensional droplet size is evaluated by calculate the non-dimension droplet volume. The primary droplet and the satellite droplet volume can be calculated based on the primary break-off shape and the satellite break-off shape detected above.

The primary droplet velocity is a critical in many applications. Parametric study of the effects of various factors on the primary droplet velocity is presented. The primary droplet velocity is calculated based on the primary droplet momentum when the simulation stops. The primary droplet momentum is calculated based the radius and velocity of all the elements contain in the primary droplet. Defined by equation (5.1)

$$u_d^* = \frac{\sum_{i=1}^N (\pi \cdot r_i^{*2} \cdot u_i^*)}{\sum_{i=1}^N (\pi \cdot r_i^{*2})} \quad (5.1)$$

where u_d^* is defined as the primary droplet velocity, and N is the total number of elements in the primary droplet. u_i^* is the velocity of each element.

5.2.3 Phase Angle of Break-off Time

A phase angle study is constructed to study different nozzle plate vibration characteristics on the primary and satellite droplet break-off time. The phase angle at break-off time is defined as the break-off time relative the nozzle vibration period. The nozzle vibration period is interpreted by the time history of the nozzle deflection. Figure 5.3 shows a typical centerline nozzle deflection.

The non-dimensional nozzle vibration half period can be obtained from the time it takes for the nozzle to return to its initial position, designated as, $\tau^*/2$. The phase angle of the primary/satellite break-off time is defined as:

$$\phi_d = \pi \cdot \frac{2 \cdot t_d^*}{\tau^*}, \quad \phi_s = \pi \cdot \frac{2 \cdot t_s^*}{\tau^*} \quad (5.2)$$

where ϕ_d , ϕ_s are the primary and satellite break-off time phase angle respectively, t_d^* , t_s^* are the primary and satellite break-off time respectively, and τ^* is the non-dimensional nozzle vibration period.

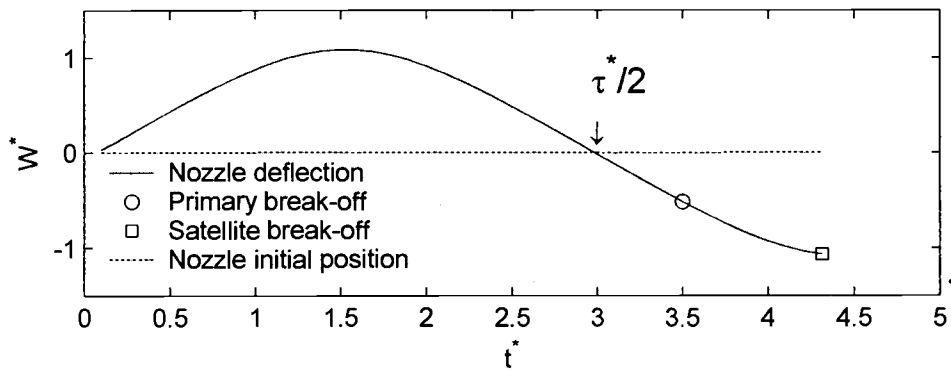


Figure 5.3: Typical nozzle deflection history; all units are nondimensionalized by the capillary scales

6. RESULTS

The results from numerical simulation will be presented in this chapter. Three different effecting factors, the driving pressure input effects, the viscous effects, and the nozzle vibration effects, on droplet formation are studied. Six parameters are chosen to study the droplet formation process, the primary break-off time, the primary droplet break-off length, the primary droplet volume, the primary droplet velocity, the satellite droplet break-off time, and the satellite droplets volume. In the first part, droplet formation from rigid nozzle are simulated to study the driving pressure input effect and viscosity effect on droplet formation. Nozzle vibration effects on droplet formation are studied in the second part. A phase angle study of the primary droplet break-off time and the satellite droplet break-off time are studied in the third.

A typical droplet formation history is determined by the driving pressure input and the resulting nozzle deflection time history as are shown in Figure 6.1. The time evolution of a droplet is shown in Figure 6.2. Initially the nozzle plate is flat, and the liquid surface is uniform at the nozzle exit plane. Slight positive pressure is applied to the chamber to overcome the capillary force. A strong positive pulsing pressure is applied to the chamber; the pressure drives the fluid flow out of the nozzle and causes the nozzle plate to deflect. The resultant liquid jet eventually breaks into a main droplet, with or without a satellite droplet forming. The break-off is denoted as a “front break” if the liquid jet first breaks into a droplet with a long liquid thread attached to the nozzle. The break-off is called a “rear break” if the liquid jet first

breaks into a droplet near the nozzle exit plane with a long liquid thread attached to the rear of the droplet. The pressure is step function of time with $t=0$ corresponding to the initiation of the pressure.

Figure 6.2 shows the fluid shape at different times after the initiation of the pressure pulse. The fluid shape and position shown in the figure is the position relative to the nozzle exit plane. The time for each figure is indicated, where time is nondimensionalized by the capillary time scales, t_c . The shape at the time when the initial half hemisphere forms, the first break-off, and the second break-off are shown. The other seven times selected to show the shapes at intermediate times. The simulation stops when the second break-off occurs, which is indicated in the last figure.

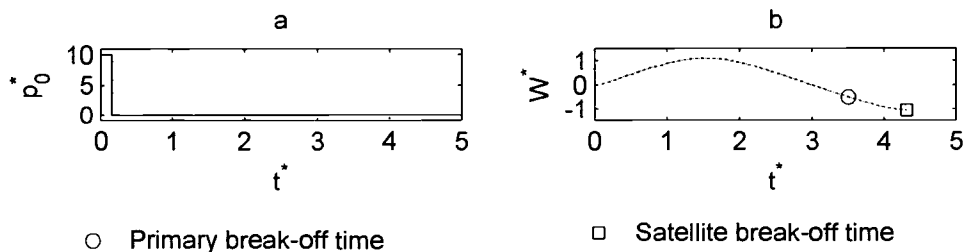


Figure 6.1: Sample driving pressure and the resulted nozzle deflection history: a) the driving pressure versus time, b) nozzle deflection versus time; all units are nondimensionalized by the capillary scales.

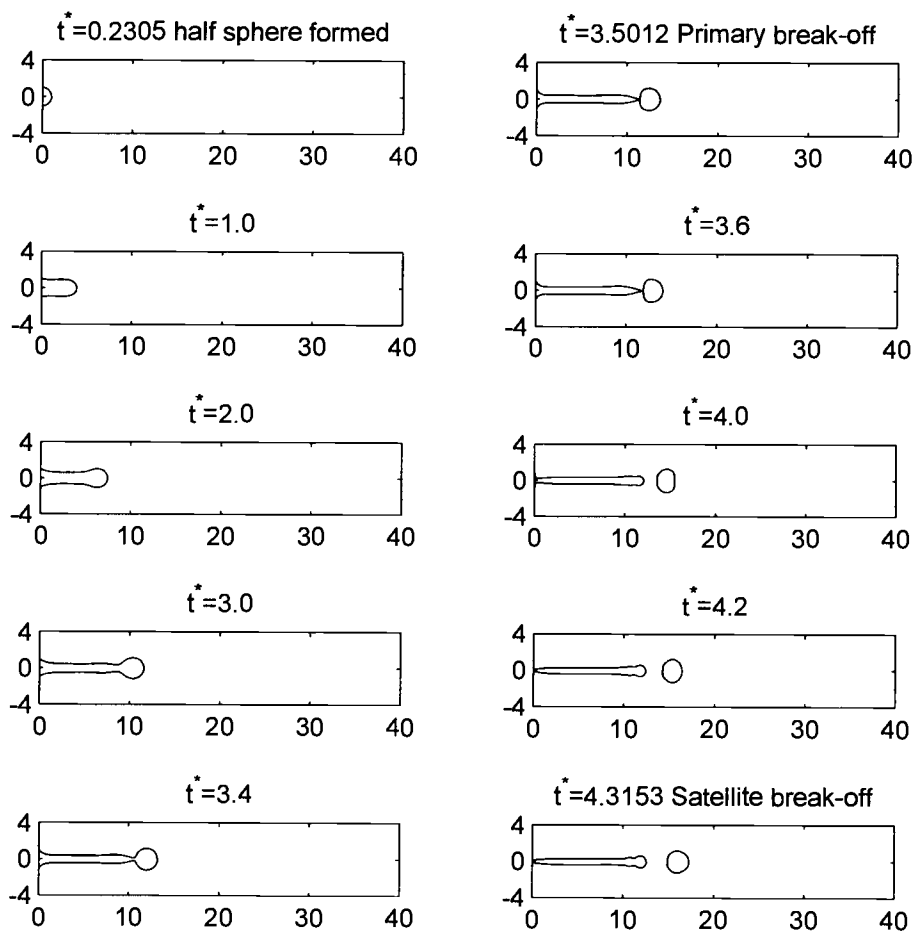


Figure 6.2: Sample droplet formation time evolution

The fluid jet break-off is caused by capillary wave instability generated by the driving pressure and nozzle vibration. As the instability develops, locally high pressure gradients and high velocity forms in some regions in the liquid jet. Fluid is pushed out of these regions in a short time. This causes the liquid jet break-off. Figure 6.3 shows the liquid jet shape together with the velocity and surface tension

distribution at a time just before break-off. The solid line represents the liquid jet shape, the dash line with '+' symbol represents the velocity distribution, and the dash-dot line with 'x' symbol represents the capillary pressure distribution. At the necking region there is a high pressure gradient and high velocity region which causes the liquid jet to break-off. The position indicated by the arrow shows the final primary droplet break-off position predicted by the development of capillary wave instability. The final break-off position simulated might differ slightly from that predicted by capillary wave instability. Close to the nozzle exit plane, a further instability is developing which eventually causes the liquid jet to break-off from nozzle, forming a satellite droplet.

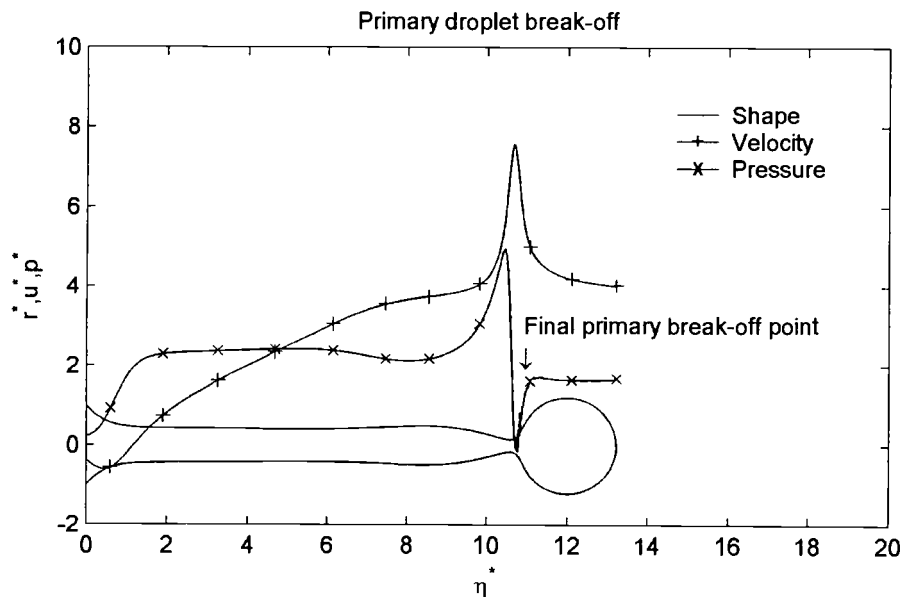


Figure 6.3: Liquid shape, velocity, and capillary pressure distribution at a time close to break-off. The final primary break-off point indicated is predicted by capillary wave instability; all units are nondimensionalized by the capillary scales

Both the primary droplet and satellite droplet are analyzed to study different operation condition and fluid property effects on droplet formation. The parameters chosen for the primary droplet are the primary droplet break-off time, the primary droplet break-off length relative to the nozzle exit plane, the primary droplet volume, and the primary droplet velocity. The parameters chosen for the satellite droplet are the satellite break-off time and the satellite volume. The primary droplet break-off time is defined as the time when the primary droplet break-off from the liquid filament. The satellite break-off time is defined as the time of the liquid filament breaks from the nozzle. The primary droplet break-off length is defined as the primary droplet break-off position relative to the nozzle exit plane. The primary droplet velocity is defined as the primary droplet velocity in a fixed coordinate frame at the time the second break-off occurs. The primary droplet velocity is calculated by the primary droplet momentum at the time of second break-off occurs. The calculation is defined by Equation 5.1.

A phase angle plot is constructed to study different nozzle vibration effects on the primary and satellite droplet break-off. The definition of primary/satellite break-off phase angle is defined by Equation 5.2.

6.1 DROPLET FORMATION FROM A RIGID NOZZLE

The driving pressure and fluid property effects on droplet formation are presented for the case of droplet formation from a rigid nozzle. The length of the pressure pulse is varied from 0.1—1.0, where time is nondimensionalized by the capillary time scale, t_c . The pressure magnitude is varied from 2.5—10, which is nondimensionalized by the capillary pressure scale, p_c . The fluid viscosity parameter Re/We is varied from 5—60, where $Re/We=60$ corresponding to water and $Re/We=5$ corresponding to fluid viscosity twelve times of water.

6.1.1 Effect of Driving Pressure

Driving pressure effects on droplet formation are studied by varying the pressure magnitude and pressure pulsing time width. According to the static hemisphere shape assumption, the minimum non-dimension pressure magnitude required to form a droplet is $P^* = 2$. Three different non-dimensional pressure magnitude selected are 2.5, 5, and 10, representing low, medium, and high pressure magnitudes. The product of pressure magnitude and pressure pulsing time width, are defined as the thrust input. The thrust input is maintained the same for different input driving pressure magnitudes. The fluid considered is water at $20^\circ C$. The break-off shapes from different input driving pressures and correspondingly different pulsing times are shown in Figure 6.4. In Figure 6.4, the column (a) shows the break-off shapes for the high pressure magnitude, the column (b) shows the break-off shape for

the medium pressure magnitude, and the column (c) shows the break-off shape for the low pressure magnitude. For the low pressure magnitude, fluid retreats back into the nozzle and no droplet forms with 1.2 thrust input.

For the case of the same thrust input, $P^* \cdot T^* = 1.2$, the higher pressure magnitude results in higher energy concentration on the front part of the liquid jet. The front moves forward with high velocity, thus a long liquid column forms. Low pressure magnitudes result in a more uniform energy distribution. The fluid tip does not move too far at the time of break-off, thus much shorter liquid threads form compared with those of high pressure magnitude input. The higher pressure magnitude results in more liquid flow out of the nozzle.

For a fixed pressure magnitude, longer pulsing times result in higher velocities and thus longer liquid columns at the time of break-off. However, the break-off shape for the two cases having thrust input equal to 2.5, and the pressure magnitude of 5 and 2.5 differ from the above explanation. The difference can be explained by the occurrence of the overturn phenomenon. As shown in Figure 6.4, for the thrust input of $P^* \cdot T^* = 1.2$ and pressure magnitude $P^* = 5$, the minimum radius of the liquid jet is not small enough to initiate break-off. But, break-off is detected by this program because of the existence of high surface gradients at the break-off region. The phenomenon of high surface gradient occurs earlier with a small radius resulting in a predicted break-off, where in fact an overturn phenomenon occurs. Unfortunately the one-dimensional model can not simulate the overturn process since it requires multiple radii at a given location.

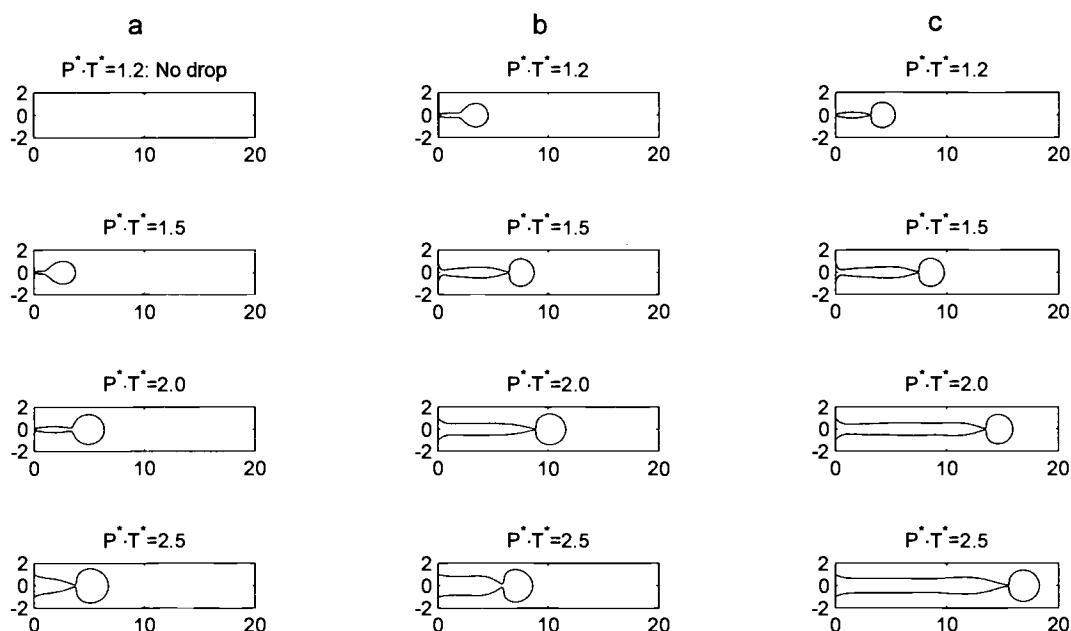


Figure 6.4: Break-off shapes for rigid nozzle by different pressure inputs; all units are nondimensionalized by the capillary scales; (a) $P^* = 2.5$, (b) $P^* = 5$, (c) $P^* = 10$

Driving pressure effects on the primary droplet break-off time, break-off length, primary droplet volume, and primary drop velocity are shown in Figure 6.5. In Figure 6.5 a) it is shown that in order to form a droplet the pressure magnitude must be higher than a minimum critical pressure, and therefore there is a minimum thrust input for each pressure magnitude. The break-off time for a step pulsing pressure input is roughly constant, about 3.5 times of the capillary time scale, if the pressure magnitude is sufficiently high. The break-off time for a low pressure magnitude, is slightly longer, about 4.0 times of the capillary time scale. Figure 6.5.b indicates the break-off length increases as the thrust input increases and the pressure magnitude

increases. This is because the droplet velocity increases and the break-off time remains about constant as the thrust input increases and pressure magnitude increases. The break-off time and break-off length for a high thrust input in Figures 6.5.a and 6.5.b show divergence from the above explanation. This is due to the overturn phenomenon mentioned previously for a high thrust input. For a high thrust input, the break-off shape indicates the possibility of the overturn phenomenon which is not captured by the numerical model, and the physical break-off time should be longer and the break-off length should be longer than what is indicated from the simulations.

Figure 6.5.c shows that the primary droplet volume increases as the thrust input increase, but is not significantly affected by pressure magnitude. The primary droplet velocity increases as the thrust input increases and the pressure magnitude increases, which is shown in Figure 6.5.d.

The effects of driving pressure on satellite break-off time and satellite volume are shown in Figure 6.6. The satellite break-off time increases as the thrust input increases, but is independent of the pressure magnitude. The increase of the satellite break-off time with increasing thrust input is due to the higher velocity at the end of the pressure pulse. With the higher velocity deceleration takes longer to decrease to achieve a negative velocity, which is a necessary condition for the satellite to break-off from the nozzle. The thrust input effect on satellite volume is shown in figure 6.6.b. The satellite volume increases as the thrust increases and pressure magnitude increases. The satellite volume shown in Figure 6.6.b is the total volume of the

satellite, where the satellite might form only one droplet or break-off into multiple droplets depending on different operation condition.

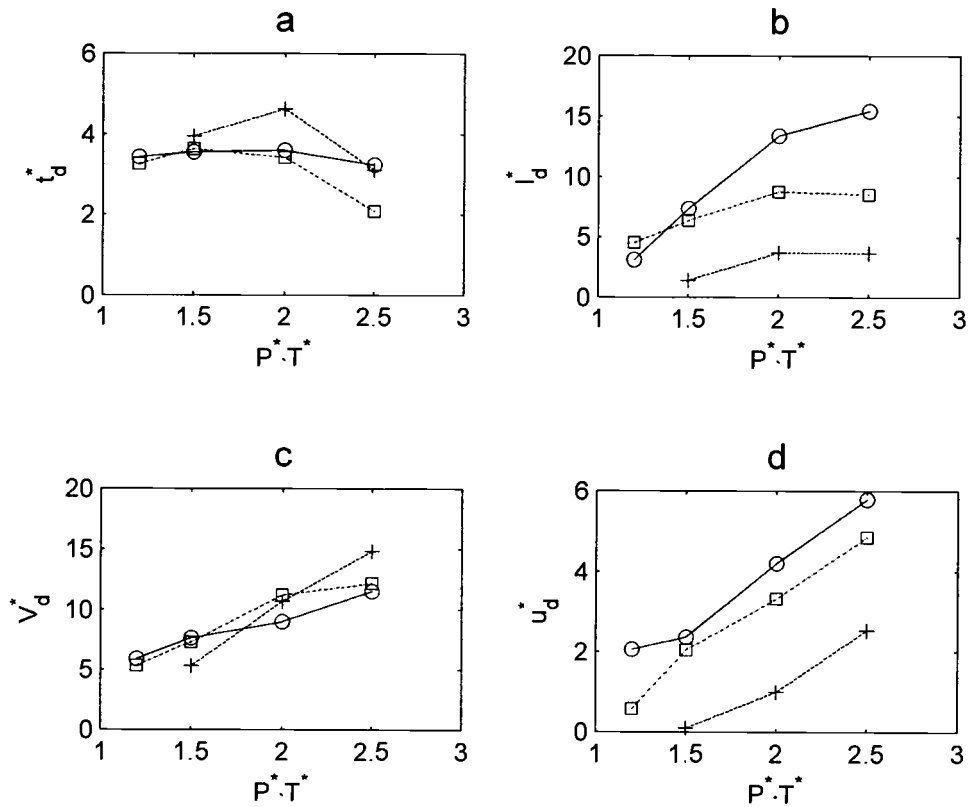


Figure 6.5: Primary droplet formation parameters versus nondimensional thrust $P^* \cdot T^*$; all units are non-dimensionalized by the capillary scales; a) primary break-off time, t_d^* , b) primary break-off length, l_d^* , c) primary droplet volume, V_d^* , d) primary droplet velocity, u_d^* . 'o', '□', and '+' represent $P^* = 10$, 5, and 2.5 respectively

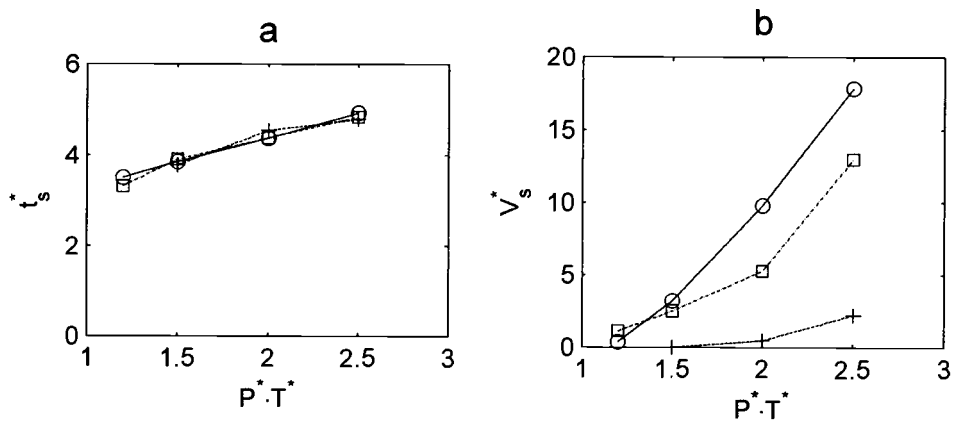


Figure 6.6: Satellite droplet formation parameters versus nondimensional thrust $P^* \cdot T^*$; all units are nondimensionalized by the capillary scales; a) primary break-off time, t_s^* , b) primary droplet volume, V_s^* . '○', '□', and '+' represent $P^* = 10, 5,$ and 2.5 respectively

6.1.2 Viscous Effects

The viscous effects on droplet formation are shown in Figure 6.7. The first, second, and third column in Figure 6.7 show the different pressure magnitude inputs. Fluid viscosity is varied while all other properties are kept the same as water. The parameter Re/We in Figure 6.7 is the non-dimensional viscous effect parameter calculated base on the geometric set-up and corresponding fluid properties. Re/We varies inversely with viscosity, $Re/We = 60$ represents water, $Re/We = 30$ represents a fluid with twice the viscosity of water, and $Re/We = 5$ represents a fluid with twelve times the viscosity of water. The input driving pressure has the same non-dimensional

thrust input of $P^* \cdot T^* = 2.0$, and the three different pressure magnitudes considered are 10, 5, and 2.5.

Figure 6.7 shows the fluid break-off characteristic with a long liquid thread attached to the nozzle. Increasing the fluid viscosity will result in longer and thinner liquid threads. The surface gradient at the primary break-off time increases when increasing the fluid viscosity. For the higher viscous fluid, $Re/We = 5$, results show that the surface gradient becomes infinite before the minimum radius goes to zero which indicates the occurrence of the overturn phenomenon, which can not be handled by the one-dimensional model, so the actual break-off is not correctly predicted.

Viscous effects on the primary droplet break-off time, primary droplet break-off length, primary droplet volume and primary droplet velocity are shown in Figure 6.8. The definition of Re/We and the input driving pressure are the same as those given for Figure 6.7. Figure 6.8 a) shows that the primary break-off time increases as the fluid viscosity increases, the primary break-off time approaches a constant value, about 3.5 times the capillary time scale, as the viscosity decreases. The different pressure magnitude affects the primary break-off for the low pressure magnitude case, and this effect is small when the pressure magnitude is high. Since a typical DOD printer is excited by a high magnitude pulsing pressure magnitude, the exact pressure magnitude may not affect primary break-off time based on these results. Figure 6.8.b indicates the break-off length increases as the fluid viscosity increases. This is partially due to the increase of break-off time. The effect of fluid viscosity on primary

droplet volume and primary droplet velocity is not significant as shown in Figures 6.8.c and 6.8.d.

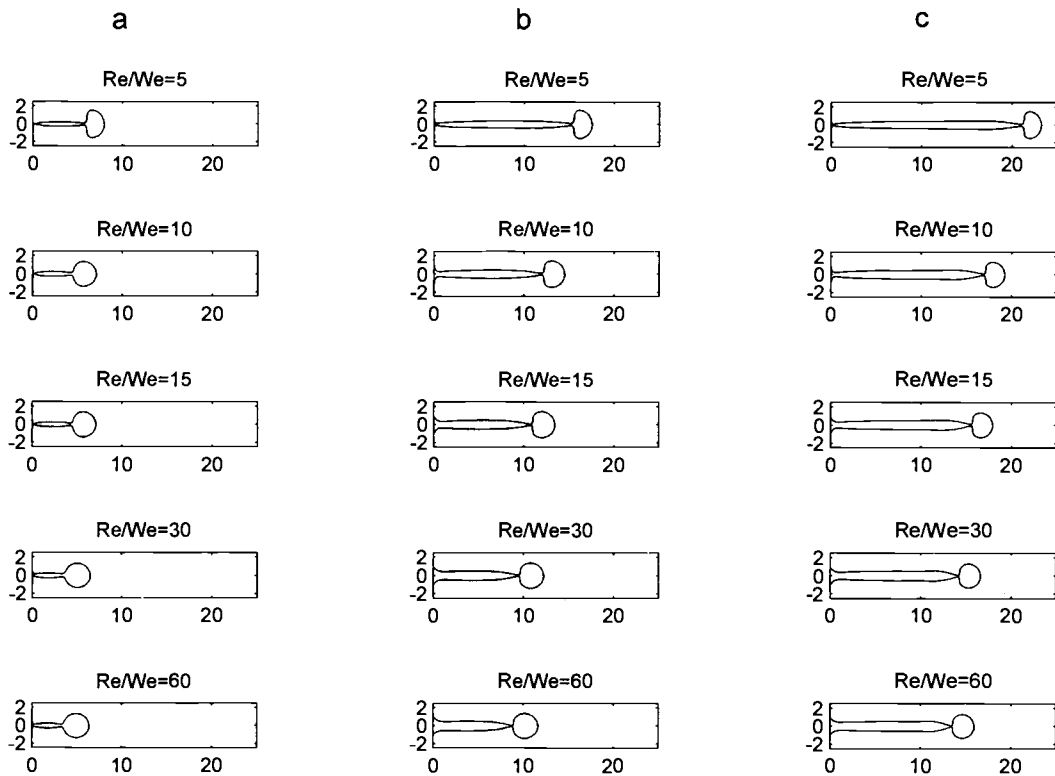


Figure 6.7: Break-off shapes versus viscosity as expressed through Re/We ; all units are nondimensionalized by the capillary scales; (a) $P^* = 2.5$, (b) $P^* = 5$, (c) $P^* = 10$

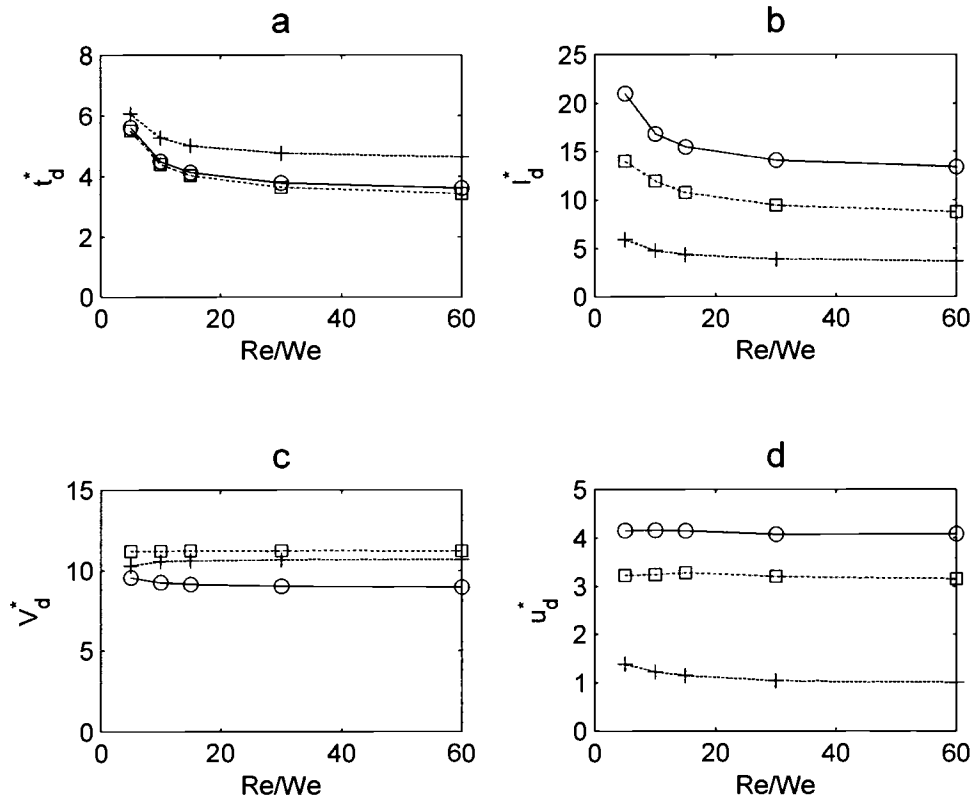


Figure 6.8: Viscous effect on primary droplet; all units are nondimensionalized by the capillary scales; a) primary break-off time, t_d^* , b) primary break-off length, l_d^* , c) primary droplet volume, V_d^* , d) primary droplet velocity, u_d^* ; ‘○’, ‘□’, and ‘+’ symbol represent $P^* = 10, 5, 2.5$ respectively

Viscous effects on satellite break-off time and satellite volume are shown in Figure 6.9. The satellite break-off time increases as fluid viscosity increases but is independent of the pressure magnitude. This is due to the fact that the viscous force has a damping effect on the capillary waves. Increasing fluid viscosity results in strong damping effects, thus strong resistance to the development of capillary wave instability. Figure 6.9.b shows fluid viscosity does not significantly affect satellite volume. For a highly viscous fluid, the overturn phenomenon prohibits accurate prediction of break-off phenomenon using this model, thus the resultant error for high viscous fluids is slightly higher than that for low viscous fluid.

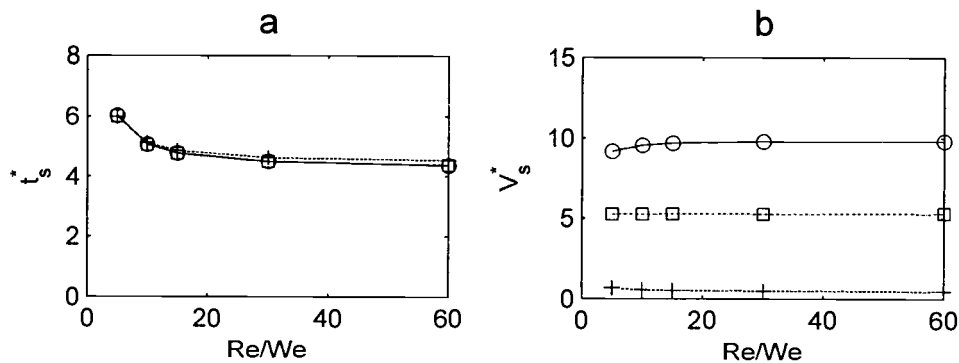


Figure 6.9: Viscous effect on satellite droplet formation; all units are nondimensionalized by the capillary scales; a) satellite break-off time, t_s^* , b) satellite volume, V_s^* ; 'o', '□', and '+' represent $P^* = 10, 5,$ and 2.5 respectively

6.2 NOZZLE VIBRATION EFFECT ON DROPLET FORMATION

Results for study the nozzle vibration effects on droplet formation consist two parts. First, droplet formation from a vibrating nozzle which has the same geometric setup as the rigid nozzle is studied and compared with drop formation from rigid nozzle. The pressure pulse is varied from 0.1—1.0, where time is nondimensionalized by the capillary time scale, t_c . The pressure magnitude is constant 10, which is nondimensionalized by the capillary pressure scale, p_c . The fluid viscosity parameter Re/We chosen are 5 and 60, where $Re/We=60$ corresponding to water and $Re/We=5$ corresponding to fluid viscosity twelve times of water. Secondary, droplet formation from three different length nozzles are studied, results are compared for these three nozzle based on the same pressure magnitude to nozzle length ratio P^*/h^* . The pressure magnitude to nozzle length ratio is 10/0.32, which is non-dimensionalized by the capillary length scale l_c and the capillary pressure scale p_c . The length of the pressure pulse is 0.2, where time is non-dimensionalized by the capillary time scale, t_c . The fluid viscosity parameter Re/We is varied from 5—60, where $Re/We=60$ corresponding to water and $Re/We=5$ corresponding to fluid viscosity twelve times the viscosity of water.

6.2.1 Rigid Nozzle and Vibration Nozzle Comparison

Droplet formation from a vibration nozzle is studied, and compared with droplet formation from a rigid nozzle. The vibration nozzle has the same radius and same length as the rigid nozzle. The deflection of vibration nozzle is calculated by solving the dynamic plate vibration equations. Two different fluids are studied, one is water at 20°C , and the other one is a fluid with twelve times viscosity of water while all other properties are kept the same as water. The non-dimensional viscosity parameter Re/We is 60 for water, and 5 for the second fluid. The driving pressure magnitude is 10, which is non-dimensionalized by the capillary pressure scale, p_c . The thrust input is varied from 1.2—2.5 by varying the pulse times.

The break-off shapes of droplet formation by water from a rigid and a vibration nozzle are shown in Figure 6.10. The break-off shapes of droplet formation by the alternate viscosity fluid from a rigid and a vibration nozzle are shown in Figure 6.11. The break-off shapes plotted for vibration nozzle are the shape relative to the nozzle exit plane. Figure 6.10 and 6.11 shows that the nozzle vibration has a significant effect on the break-off shape. The break-off shapes from a vibration nozzle have longer liquid thread attached to the primary droplet compared with the break-off shapes from a rigid nozzle. Figures 6.10 and 6.11 do not show any evidence of the nozzle vibration effect on the occurrence of infinite shape gradient prior a small radius, which can be interpreted as the occurrence of overturn phenomenon physically.

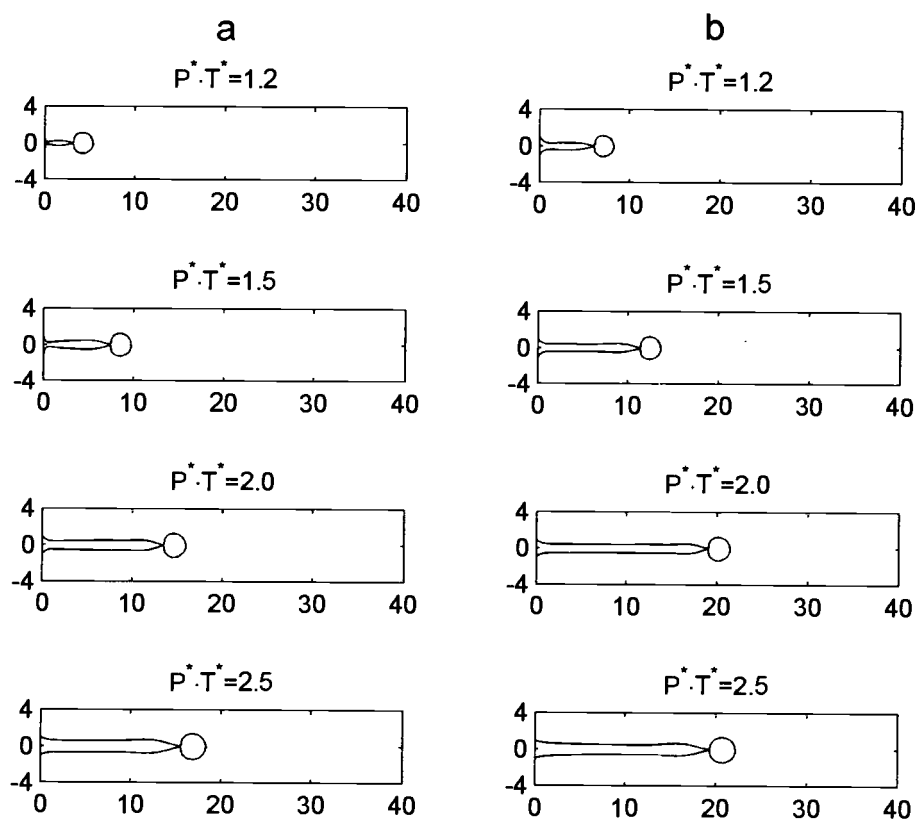


Figure 6.10: Comparison of break-off shapes by water with viscosity parameter $Re/We=60$ from a vibration and a rigid nozzle; all units are nondimensionalized by the capillary scales; (a) rigid nozzle, (b) vibration nozzle.

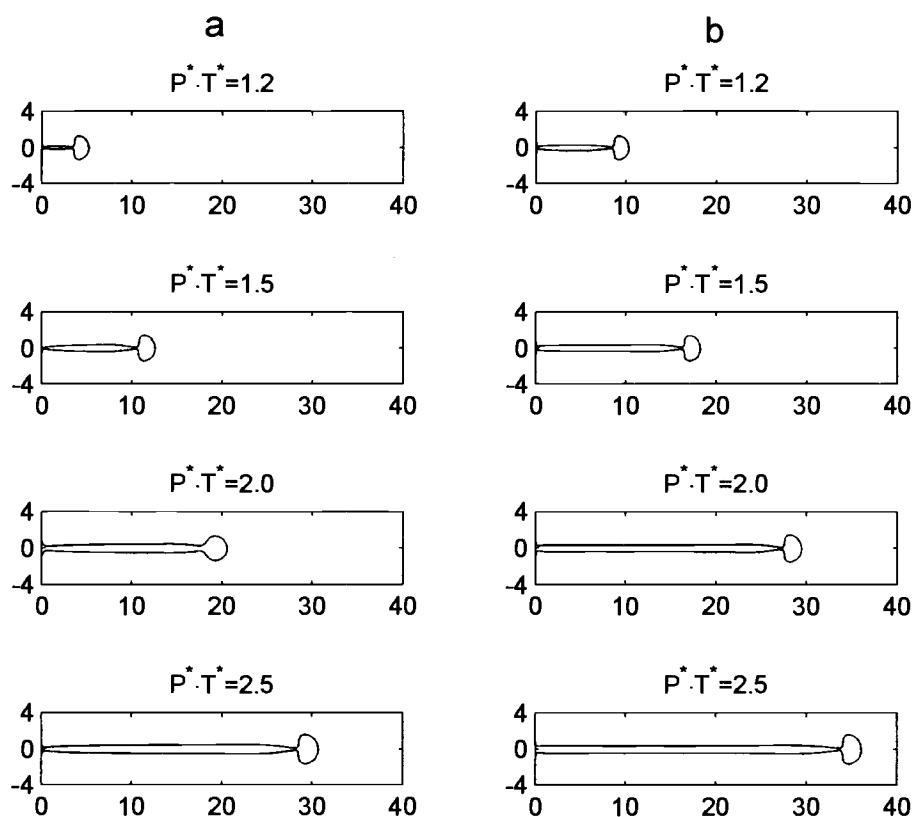


Figure 6.11: Comparison of break-off shapes by fluid with viscosity parameter $Re/We=5$ from a vibration and a rigid nozzle; all units are nondimensionalized by the capillary scales; (a) rigid nozzle, (b) vibration nozzle.

The nozzle vibration effects on the primary droplet are shown in Figure 6.12. Figure 6.12 a) shows that the nozzle vibration causes the primary droplet break-off slightly earlier, and this effect is more significant for higher thrust input. Figure 6.12.b shows that the primary droplet break-off length increases significantly by nozzle vibration. The increment is due to the increment of the primary droplet velocity, as shown in figure 6.12.d. The nozzle vibration effects on the primary

droplet volume are not significant, as shown in Figure 6.12.c. Figure 6.12.d shows that the nozzle vibration effect increases the primary droplet velocity by an order of one capillary velocity scale. The increment of the primary droplet velocity caused by the nozzle vibration effect is about the nozzle vibration velocity magnitude, which can be shown in Figure 6.13.

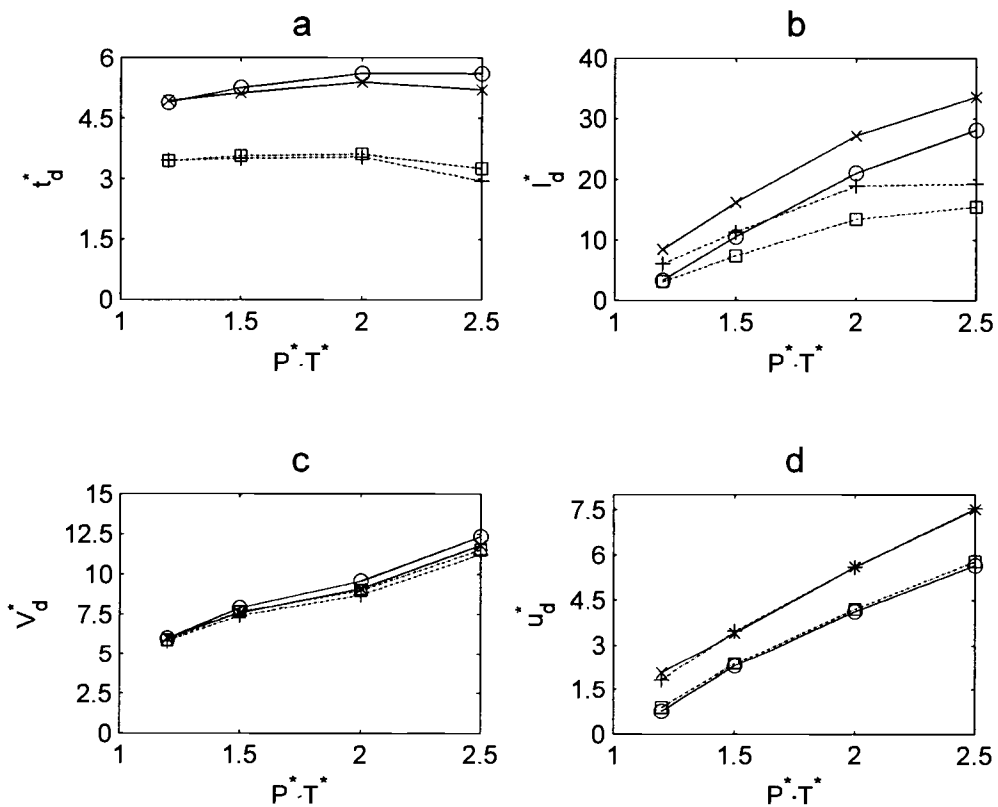


Figure 6.12: Nozzle vibration effect on the primary droplet; all units are nondimensionalized by the capillary scales; a) the primary break-off time, b) the primary break-off length, c) the primary droplet volume, d) the primary droplet velocity. 'o', '□', 'x' and '+' represent rigid nozzle $Re/We = 5$, rigid nozzle $Re/We = 60$, vibration nozzle $Re/We = 5$, and vibration nozzle $Re/We = 60$ respectively

Figure 6.13 shows the velocity increment due to the nozzle vibration effect. In Figure 6.13, “U_{rel}” represents the primary droplet velocity minus the nozzle vibration velocity magnitude. For the rigid nozzle case, the nozzle vibration velocity is zero, so “U_{rel}” equals the primary droplet velocity. The non-dimensional fluid viscosity effect parameter $Re/We = 60$ represents water, and $Re/We = 5$ represents fluid with twelve times the viscosity of water. The good agreement between the corrected primary droplet velocities for vibration nozzle cases and the rigid nozzle, as shown in Figure 6.13, shows that the nozzle vibration can increase the primary droplet velocity by an amount equal to the nozzle vibration magnitude.

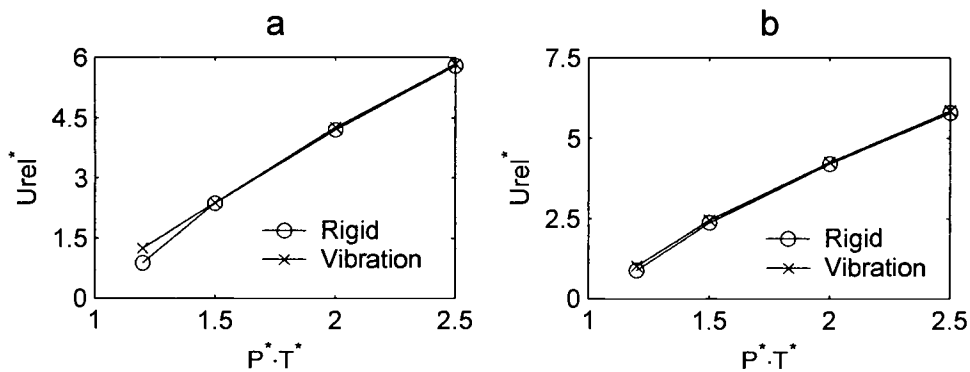


Figure 6.13: Magnitude of primary droplet velocity change by nozzle vibration; all units are nondimensionalized by the capillary scales; (a) fluid viscosity $Re/We=5$, (b) fluid viscosity $Re/We=60$

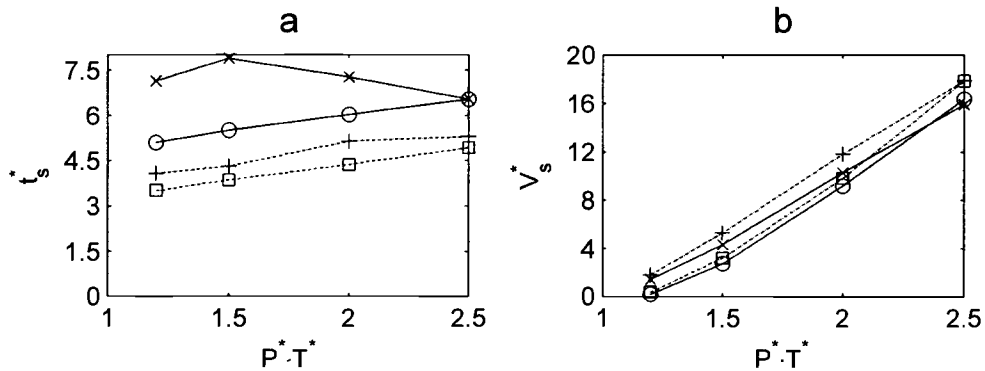


Figure 6.14: Nozzle vibration effect on satellite droplet; all units are nondimensionalized by the capillary scales; a) the satellite break-off time, b) the satellite volume; 'o', '□', 'x' and '+' represent rigid nozzle $Re/We = 5$, rigid nozzle $Re/We = 60$, vibration nozzle $Re/We = 5$, and vibration nozzle $Re/We = 60$ respectively

The nozzle vibration effect on the satellite is shown in Figure 6.14. Figure 6.14 a) shows that the nozzle vibration effects cause the satellite break-off to increase. The effects are more obvious when the fluid viscosity is low. The increment of the satellite break-off time caused by the nozzle vibration effects is about 0.5 times of the capillary time scale. For high viscous fluid, the increment of the satellite break-off time is more complex. This partially is due to the fact that the satellite break-off time is much longer for highly viscous fluid; the nozzle vibrates more than one cycle at the satellite break-off. The nozzle vibration generates multiple waves which interact each other. A phase angle study of the primary droplet break-off time and the satellite break-off time relative to the nozzle vibration period is constructed in section 6.3 to study the nozzle vibration effects on the droplet break-off. Figure 6.14.b shows the

nozzle vibration effects on the satellite volume. Figure 6.14.b shows that the nozzle vibration causes the satellite droplet volume to increase. The increment is about two times the non-dimensional volume, defined as the nozzle radius cubed. The increment is larger for low thrust input, where no satellite droplet formed from the rigid nozzle. For high thrust input, the volume increment of the satellite droplet deviates from the previous statement. This is partially due to the occurrence of the overturn phenomenon, which means that accurate prediction of break-off can not be made.

6.2.2 Different Nozzle Plate Vibration Comparison.

Droplet formations from three different vibration nozzle plates are studied, by varying the nozzle plate thickness. The three different nozzle plates have the same radius and same properties. The non-dimensional nozzle plate thicknesses considered are 0.32, 0.64, and 0.96. Driving pressure considered has fixed pulse times 0.2, nondimensionalized by capillary time scale. The diving pressure magnitude to nozzle plate thickness ratio $\frac{P^*}{h^*}$ is kept constant for the three nozzle plates studied. By keeping $\frac{P^*}{h^*}$ constant, the boundary conditions for the flow out of the nozzle are the same for the three nozzle plates considered, which can be shown by nozzle flow dynamics Equation (3.33) and assuming surface tension at nozzle exit plane is small. So the droplet formation processes from the three different nozzle plates are comparable. Five different fluids are considered in the simulation by varying the fluid viscosity while keeping all other properties the same as water.

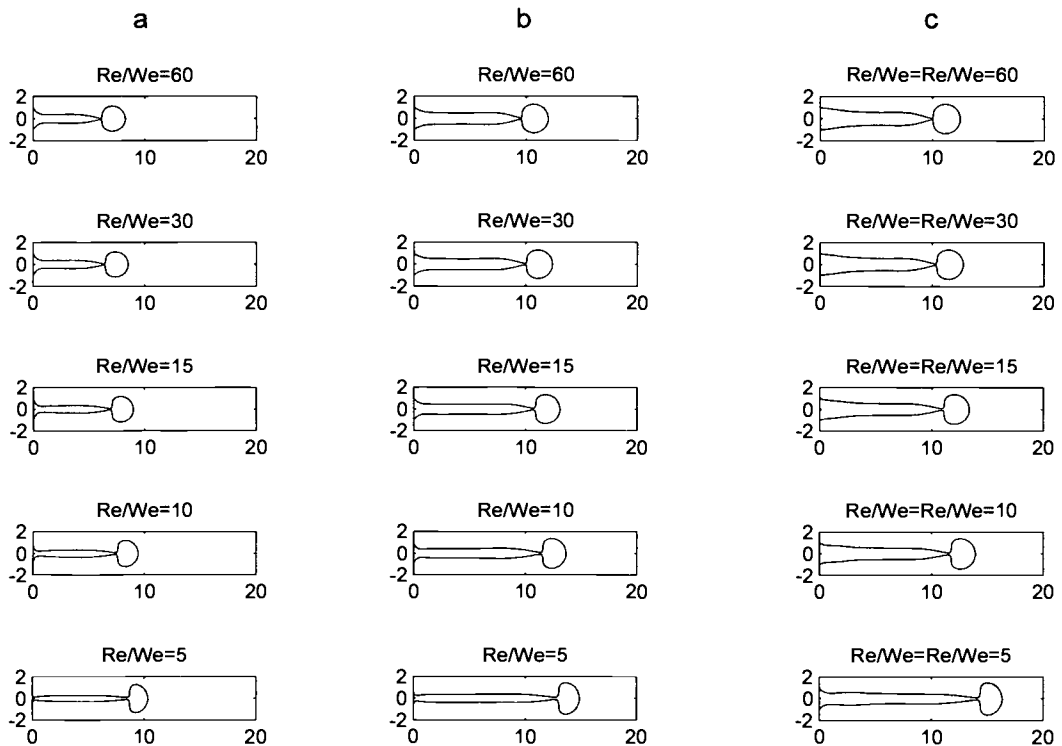


Figure 6.15: Comparison of break-off shape by three different vibration nozzles; all units are nondimensionalized by the capillary scales; (a) $h^* = 0.32$, (b) $h^* = 0.64$, (c) $h^* = 0.96$

Figure 6.15 shows the fluid break-off shape from different nozzle and different fluids. The break-off length for 0.32 length nozzle is much shorter than other the break-off length from other two nozzles. This is due to the fact that the surface tension effect on flow through the nozzle is more significant for short nozzles than that for long nozzle, which can be shown by nozzle flow dynamics equation, Equation (3.33). The break-off shape difference for the 0.64 length nozzle and the 0.96 length nozzle does not differ very much. This implies the surface tension on nozzle flow dynamics can be neglected if the nozzle is long. These three nozzles

show the occurrence of high surface gradient prior a small radius occurrence for high viscous fluid, which indicate the occurrence of overturn phenomenon.

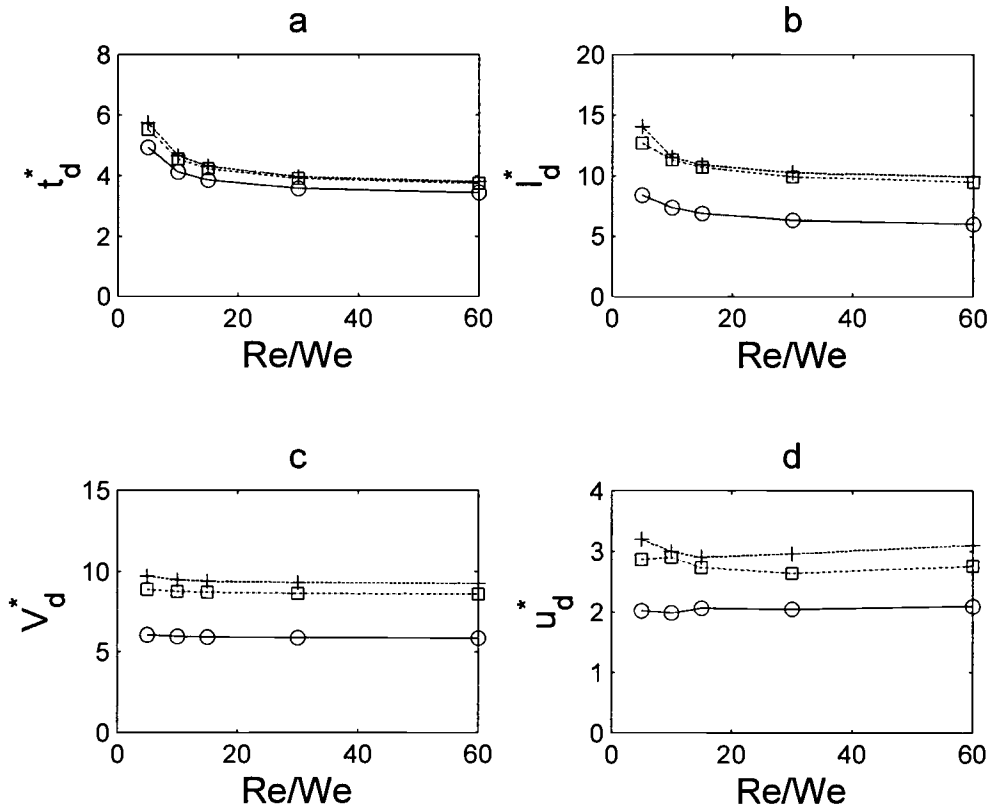


Figure 6.16: Nozzle vibration effect on primary droplet by three different nozzles; all units are nondimensionalized by the capillary scales; a) the primary break-off time, b) the primary break-off length, c) the primary droplet volume, d) the primary droplet velocity; 'o', '□', and '+' represent $h^* = 0.32, 0.64, \text{ and } 0.96$ respectively

Different nozzle vibration characteristic effects on the primary droplet are shown in Figure 6.16. Figure 6.16.a) shows the primary droplet break-off slightly earlier for the 0.32 nozzle, and the break-off time difference between the 0.64 and the 0.96 nozzles is not significant. Similar trend is found for the primary break-off length, as shown in Figures 6.16.b. Figure 6.16.c shows the primary droplet volume for the 0.64 nozzle is much bigger than the primary droplet volume for the 0.32 length nozzle, about twice of volume scales. The primary droplet volume for the 0.96 length nozzle is higher than the 0.64 length nozzle by about 0.5 of capillary volume scales. Figure 6.16.d shows that the primary droplet velocity is much smaller for the 0.32 length nozzle, and the droplet velocity for the 0.96 length nozzle is higher than the 0.64 length nozzle by about 0.2 of capillary velocity scales. These results show that the differences between the 0.32 length nozzle and the 0.64 length nozzle are much bigger than the difference between 0.64 length nozzle and 0.96 length nozzles. This can be interpreted as the nozzle thickness is not an important factor if the nozzle is sufficient long. For short nozzle the surface tension effect is important.

Different nozzle vibration characteristics effects on the satellite droplet break-off can be shown in Figure 6.17. Figure 6.17.a) shows that the satellite break-off times differ from each other for the three nozzles studied. Satellite break-off time is shortest for the 0.32 length nozzle, slightly longer for the 0.64 length nozzle, and the longest for the 0.96 length nozzle. The difference can be explained from the nozzle vibration characteristic, since the satellite break-off time does not affect significantly by the thrust input as shown in section 6.1 and the surface tension effect on flow

through nozzle can be simplified as a correction to the thrust input. The phase angle study in section 6.3 is helpful in analyzing the nozzle vibration effect on satellite break-off time. Figure 6.17.b) shows the satellite droplet volume is smallest for the 0.32 length nozzle; slightly larger for the 0.64 length nozzle, and the largest for the 0.96 length nozzle. Both surface tension effect and nozzle vibration characteristics can affect the satellite droplet volume. Based on these results, it is not clear how important of each factor is. But the difference between 0.64 length nozzle and 0.96 length nozzle indicates higher nozzle vibration frequency may cause bigger satellites.

Since the three nozzles studied are all based on the same physical materials, the nozzle vibration cycle, and nozzle vibration magnitude are closely related to each other. It is not clear which property is dominant in nozzle vibration on droplet formation.

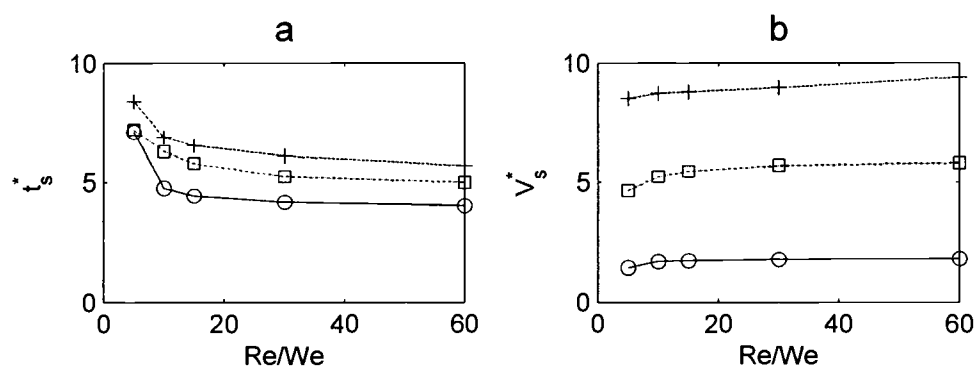


Figure 6.17: Nozzle vibration effect on satellite compared that from rigid nozzle; all units are nondimensionalized by the capillary scales; a) satellite break-off time, b) satellite volume. 'o', '□', and '+' represent $h^* = 0.32$, 0.64, and 0.96 respectively

6.3 PHASE ANGLE OF BREAK-OFF RELATIVE TO NOZZLE VIBRATION

The phase angle is defined by equation 6.2. The Phase angle plot of the primary droplet break-off time for the three nozzles studied is shown in Figure 6.18. A phase angle plot of the satellite droplet break-off time for the three nozzle studied is shown in Figure 6.19. In Figures 6.18 and 6.19, the x-axis is the nondimensional nozzle plate thickness and y-axis is the phase angle of break-off times. Different fluids studied are shown by the non-dimensional viscosity Re/We . The driving pressure has fixed non-dimensional pulse times of 0.2 based on the capillary time scale. The non-dimensional driving pressure magnitude to nozzle length ratio is fixed

$$\text{also, } \frac{P^*}{h^*} = \frac{125}{4}$$

Figure 6.18 shows the primary droplet break-off occurs mostly within one nozzle vibration period. For so short time, the nozzle vibration damping effect on droplet formation is not important for the droplet ejector considered. For known driving pressure input, the primary droplet break-off time is dependent on fluid viscosity as shown in Figure 6.16. The increment of the primary break-off phase angle with the nozzle plate thickness, as shown in Figure 6.18, is due to the increment of the nozzle plate natural frequency. The phase angle increment is not $2 \cdot \pi$, but a small phase angle, which indicates the primary droplet break-off is not a direct result of nozzle vibration. Figure 6.18 shows, for the case studied, the primary droplet

break-off time does not show strong dependence on the different nozzle vibration characteristic.

A phase angle plot of the satellite break-off time for the three nozzles studied is shown in Figure 6.19. The satellite droplet break-off occurs within two nozzle vibration periods. The increment of the satellite break-off phase angle with the nozzle plate thickness, as shown in Figure 6.19, is due to the increment of the nozzle plate natural frequency. The phase angle increment is not $2 \cdot \pi$, but a small phase angle, which indicates that the satellite droplet break-off is not a direct result of the nozzle vibration. Figure 6.19 shows, for the case studied, the satellite break-off does not show strong dependence on the different nozzle vibration characteristic

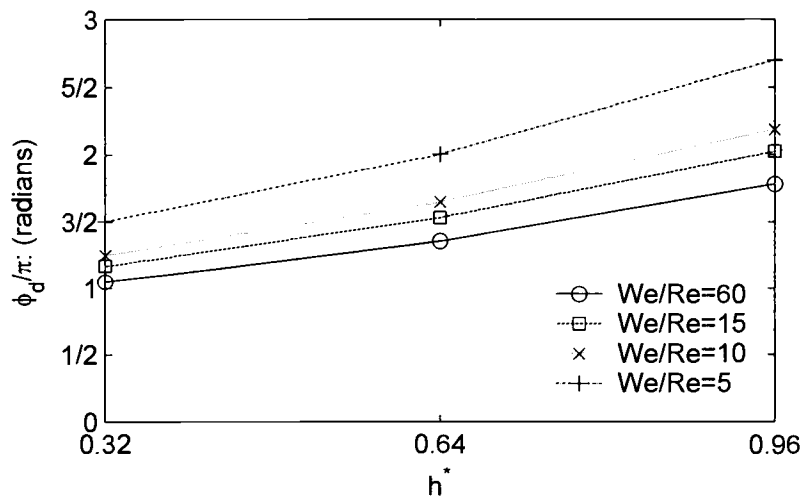


Figure 6.18: Phase angle study of primary droplet break-off; all units are nondimensionalized by the capillary scales

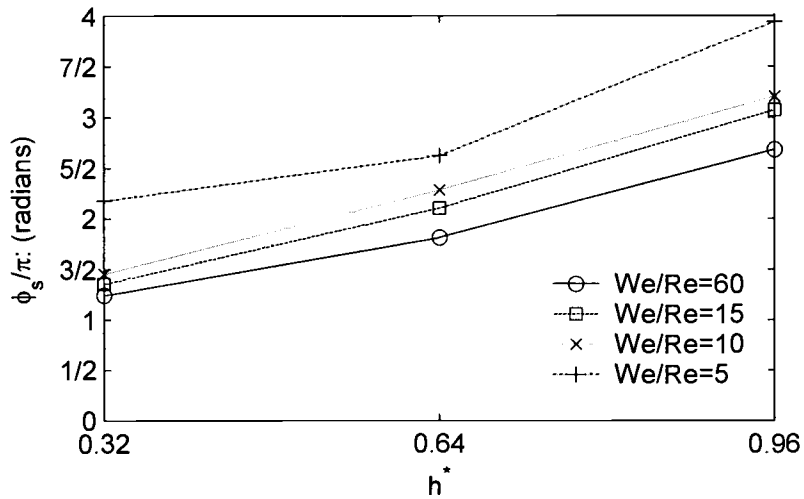


Figure 6.19: Phase angle study of satellite break-off time; all units are nondimensionalized by the capillary scales.

The reason that the droplet break-off depends on the nozzle vibration characteristics only slightly can be explained as that the break-off phenomenon is a development of capillary wave instability. The disturbance frequency affects the development of instability significantly, but the initial disturbance magnitude does not. The instability induced by the pressure pulse dominates the primary droplet break-off, so the nozzle vibration effect on primary break-off is neglectable. The instability caused the satellite break-off consists the effects from both the surface tension and the nozzle vibration. For the case of nozzle is not long enough, the surface tension effect is more important than the nozzle vibration characteristic, so satellite break-off depends on nozzle vibration characteristic slightly.

7. CONCLUSIONS AND RECOMMENDATION

7.1 CONCLUSIONS

A numerical model simulating droplet ejection from a rigid nozzle and a vibrating nozzle has been constructed. Droplet formation from a rigid nozzle is simulated in order to study the different input driving pressure and viscous effects. The numerical modeling of droplet ejection from a vibrating nozzle is simulated based on the same driving pressure and fluid properties and compared with that from a rigid nozzle case. Droplet formation from vibrating nozzle is newly simulated and can not, at this time, be compared with experiments.

Results show that the primary droplet break-off time is affected by fluid viscosity significantly, and higher fluid viscosity results longer break-off time. Primary droplet volume depends on both driving pressure magnitude and thrust input, increasing pressure magnitude and thrust input results in larger size primary droplet. The primary droplet velocity can be affected by pressure magnitude and thrust input. Higher pressure magnitude and thrust input results in high primary droplet velocity. For the cases studied of the vibrating nozzle, the primary droplet break-off occurs within one cycle of nozzle vibration. Results show nozzle vibration effect on primary droplet break-off time and primary droplet size is small, but the effect on primary droplet velocity is significant. Results show the primary droplet velocity is increased

by the order of nozzle vibration magnitude. This means that droplets of similar size with higher momentum by inducing nozzle vibration.

For single pulsing pressure input, all the cases studied show the happening of satellite droplets. Results show that the nozzle vibration increases the size of satellite droplet. Longer liquid threads forms for highly viscous fluids, while increasing driving pressure magnitude and thrust input increases the volume of satellite droplets. It is suggested that a negative pressure pulse can assist the retreat of fluid back into the nozzle, which may minimize the occurrence of satellite droplet.

For the case of high thrust input and high viscous fluid, the maximum liquid shape gradient reaches infinity before zero minimum radiuses reached which can be interpreted as occurrence of overturn phenomenon. The occurrence of overturn phenomenon prohibits accurate modeling of droplet formation process, because the one-dimension model can not resolve this effect.

7.2 RECOMMENDATIONS

Since the changing of the free surface shape with time, smaller grid size is required to accurate model in the region of high shape gradient region. Locally adaptive grid size is favored for accurate modeling of the physics close to singularities while maintaining reasonable computation time. Due to the inability of one-dimensional model to overturn phenomenon, a three-dimensional model is favorable for accurate modeling of the break-off process when the overturn

phenomenon might occur. Since the known boundary condition is the upstream pressure, accurate modeling of flow through nozzle is critical. Current model for flow through nozzle is based on inviscid assumptions and subject to improvement. The error resulted from the current model will be much higher for thick nozzle plate and longer pulsing time width. A model that also includes the entire nozzle and plenum would be more accurate.

Of all the cases studied for pulsing driving pressure input, the formation of satellite droplet seems to be inevitable for this geometry and this wave form. Studies of different driving pressure functions are advised in future study in order to see if a favored driving pressure function can be found.

It is also recommended to study the different nozzle vibration characteristics on droplet formation. The nozzle vibration characteristics are advised to be changed artificially in order to study the nozzle vibration magnitude and vibration frequency effect, which are related to each other, on droplet formation. From these studies it may be possible to identify an ideal material and nozzle size to obtain large velocity droplet without satellite formation.

BIBLIOGRAPHY

- Adams R. L. and Roy J., 1986, "A One-Dimensional Numerical Model of A Drop-on-Demand Ink Jet", *Journal of Applied Mechanics*, Vol. 53, pp193-197
- Bogy D. B., and Talke F. E., 1984, "Experimental and Theoretical Study of Wave Propagation Phenomenon in Drop-on-Demand Ink Jet Devices", *IBM Journal of Research and Development*, Vol. 28, pp 314—321
- Brenner, M. P., Eggers, J., Joseph, K., Nagel, S. R., and Shi, X. D., 1997, "Breakdown of Scaling in droplet Fission at High Reynolds Number", *Physics of Fluids*, Vol. 9, pp1573-1589.
- Burr R. F., Tence D. A., and Berger S. S., 1996, "Multiple Dot Size Fluidics for Phase Change Piezoelectric Ink Jets", *International Conference on Digital Printing Technology*, Vol. 12, pp 12—18
- Chen A. U. and Basaran O. A., 2002, a, "A New Method for Significantly Reducing Drop Radius without Reducing Nozzle Radius in Drop-on-Demand Drop Production", *Physics of Fluids*, Vol. 14, pp L1—L4
- Chen A. U., Notz P. K. and Basaran O. A., 2002 b, "Computational and Experimental Analysis of Pinching-off and Scaling", *Physical Review Letters*, Vol. 88, pp 174501-1—174501-4
- Day R. F., Hinch J. E., and Lister J. R., 1998, "Self-Similar Capillary Pinch off of an Inviscid Fluid", *Physical Review Letters*, Vol. 80, pp704—707
- Eggers J., 1993, "Universal Pinching of 3D Ax symmetric Free-Surface Flow", *Physical Review Letters*, Vol. 71, pp3458-3460
- Eggers J and Dupont, T. F., 1994, "Drop Formation in a One-Dimensional Approximation of the Navier-Stokes Equation", *Journal of Fluid Mechanics*, Vol. 262, pp205-221
- Eggers J., 1997, "Nonlinear Dynamics and Breakup of Free-Surface Flows", *Review Modern Physics*, Vol. 69, pp 865—930.
- Eggers J., 2000, "Singularities in Droplet Pinching With Vanishing Viscosity", *SIAM Journal of Applied Mathematics*, Vol. 60, pp 1997—2008

- Foote G. B., 1973, "A Numerical Method for Studying Liquid Drop Behavior: Simple Oscillation", *Journal of Computational Physics*, Vol. 11, pp 507—530.
- Fromm J. E., 1982, "Numerical Calculation of the Fluid Dynamics of Drop-on-Demand Jets", *IBM Journal of Research and Development*, Vol. 28, pp322-333
- Hofer E. P., 1986, "Spot-Size Modulation in Drop-On-Demand Ink-Jet Technology", *Proceedings of the SID*, Vol. 27, pp 37—40
- Kreith F., *The CRC handbook of mechanical engineering*, CRC Press, Boca Raton Fla. 1994
- Lee H. C., 1974, "Drop formation in a liquid jet", *IBM J. research and development*, Vol.18, pp364-369
- Lee H. P., 1998, "Progress and Trends in Ink-Jet Printing Technology", *Journal of Imaging Science and Technology*, Vol. 42, pp 49—62
- Lister J. R., and Stone H. A., 1998, "Capillary Breakup of a Viscous Thread Surrounded By another Viscous Fluid", *Physics of Fluids*, Vol. 10, pp 2758—2764
- Metglas physical properties, Less EMF Inc, 141 Soller Heights Road , Ghent, NY 12075, USA.
- Middleman S., *Modeling of Axisymmetric Flow*, Academic Press, NY, 1995.
- Munson B. R., Young D. F., and Okiishi T. H., *Fundamentals of Fluid Mechanics*, John Wiley & Sons Inc. NY, 1990.
- Pan F., Kubby J., and Chen J, 2002, "Numerical Simulation of Fluid-Structure Interaction in a MEMS Diaphragm Drop Ejector", *Journal of Micro-Mechanics and Micro-Engineering*", Vol. 12, pp 70—76
- Papageorgiou D. T., 1995, "On the Breakup of Viscous Liquid Thread", *Physics of Fluids*, Vol. 7, pp 1529—1540.
- Percin G., and Khuri-Yakub B. T., 2003, "Piezoelectric Droplet Ejector for Ink-Jet Printing of Fluids and Solid Particles", *Review of Science Instruments*, Vol. 74, pp 1120—1127
- Peregrine D. H., Shoker G., and Symon A., 1990, "The Bifurcation of Liquid Bridges", *Journal of Fluid Mechanics*, Vol. 212, pp25-39

- Rao J. S. Dynamics of Plates, M Dekker, NY, 1999.
- Rayleigh L., 1878, "On the Instability of Jet", Proceedings of the London Mathematical Society, Vol. 10, pp4-13
- Shield T. W., and Bogy D. B., 1986, "A Numerical Comparison of One-Dimensional Fluid Jet Models Applied to Drop-On-Demand Printing", Journal of Computational Physics, Vol.67, pp 327—347
- Shield T. W., Bogy D. B., and Talke F. E., 1987, "Drop formation by DOD ink-jet nozzle: A comparison of experimental and numerical simulation", IBM Journal of Research and Development, Vol.31, pp 96—110.
- Sangrut, Personal communication
- Szilard R. Theory and Analysis of Plates, Prentice-Hall, NJ, 1974
- Timoshenko S, and Woinowsky-Krieger S., Theory of Plates and Shells, McGraw-Hill, NY, 1959
- Wilkes E. D., Phillips S. D., and Basaran O. A., 1999, "Computational and Experimental Analysis of Dynamics of Drop Formation", Physics of Fluids, Vol. 11, pp 3577—3597.
- Yamamoto, K. Kawashima T. Watanabe T., and Tokunaga, T, 1991, "Drop Formation in A Drop-on-Demand Ink Jet", Flucome '91, pp 339—342

APPENDICES

APPENDIX A

FORTRAN Source Code

The program is written in FORTRAN 90. The program consist one main program, ten subroutines, and four functions. The function of each subroutine and each function is listed below. The order of subroutines and functions shown in the appendix is in the same order as the list below.

Subroutines:

Initial:	Modeling droplet formation prior a half-hemisphere formed
Onedsolution:	Modeling droplet formation prior break-off occurs
Breakoffjet:	Determine the break-off
Dropmove:	Modeling free movement of break-off droplet
Residue:	Modeling liquid filament attached to nozzle after break-off occurs
Input:	Define the input parameters and return the non-dimensional parameters and capillary scales
Dripre:	Define the driving pressure input for the code
Curvature:	Calculate the pressure by FDE according to Young-Laplace equation
Gradient:	Calculate the velocity gradient by FDE
Galerkincoe:	Define the modal shape solution parameters for plate vibration equation

Functions:

P:	Return the driving pressure value at the specified time step
Uoriout:	Return flow velocity at nozzle exit plane at the specified time step
Wplate:	Return the nozzle deflection at specified time step
Uplate:	Return the nozzle vibration velocity at specified time step

Main Program

```

! PROGRAM MAIN FOR DROPFORMATION
  INCLUDE 'INPUT.F90'           !Input variables
  INCLUDE 'DRIPRE.F90'         !Define driving pressure input
  INCLUDE 'PRESSUREFUN.F90'    !Driving pressure as a function
  INCLUDE 'GALERKINCOE.F90'    !Nozzle modal shape parameter
  INCLUDE 'WPLATE.F90'         !Nozzle deflection and velocity
  INCLUDE 'FLOWOUTNOZZLE.F90'  !Nozzle flow dynamics
  INCLUDE 'CURVATURE.F90'      !Surface tension calculation
  INCLUDE 'GRADIENT.F90'       !FDE of velocity gradient
  INCLUDE 'INITIAL.F90'        !Initial stage modeling
  INCLUDE 'ONEDSOLUTION.F90'   !1-D model by MacCormack
  INCLUDE 'DROPMOVE.F90'       !Model movement of droplet
  INCLUDE 'RESIDUE.F90'        !Model liquid filament movement
  INCLUDE 'BREAKOFF.F90'

  !NMAX:                        Time serial output limitation
  !MMAX:                        Axial liquid jet length limitation
  INTEGER, PARAMETER :: NMAX=1E2, MMAX=20
  DOUBLE PRECISION, PARAMETER :: PI=3.14159265358979

  INTEGER M_z                   !Time grid refinement parameter
  INTEGER M_dz                  !Spatial grid refinement parameter
  INTEGER N_dz                  !Maximum spacial grid number

  INTEGER N                     !Time step excecuted
  INTEGER M, MD, MS             !Actural liquid jet grid number
  DOUBLE PRECISION, ALLOCATABLE :: U_j(:)      !Element velocity
  DOUBLE PRECISION, ALLOCATABLE :: SQR(:)      !Element radius
  DOUBLE PRECISION, ALLOCATABLE :: Z(:)        !Element location

  !*store: Value stored at time of break-off to be used in
  !         droplet movement model and filament model
  INTEGER Mstore                !Time step excecuted
  INTEGER Nstore                !Actural liquid jet grid number
  DOUBLE PRECISION, ALLOCATABLE :: Ustore_j(:) !Element velocity
  DOUBLE PRECISION, ALLOCATABLE :: SQRstore(:) !Element radius
  DOUBLE PRECISION, ALLOCATABLE :: Zstore(:)   !Element location

  DOUBLE PRECISION V_out        !Volume of fluid out ot nozzle
  DOUBLE PRECISION V_drop       !Volume of fluid in droplet/filament

  DOUBLE PRECISION WR           !We/Re number, Viscous effect
  DOUBLE PRECISION Bo           !Bond number, gravational effect
  DOUBLE PRECISION S_p          !Pressure scale
  DOUBLE PRECISION S_t          !Time scale
  DOUBLE PRECISION S_v          !Velocity scale
  DOUBLE PRECISION S_l          !Length scale
  DOUBLE PRECISION PMAX         !Driving pressure magnitude

```

```

DOUBLE PRECISION F_dr      !Driving pressure frequency
DOUBLE PRECISION T_pul     !Driving pressure pulse times
DOUBLE PRECISION T_end     !MAX time length the code can run
DOUBLE PRECISION dT        !Time step

DOUBLE PRECISION Hpl       !Plate thickness, Nozzle length
DOUBLE PRECISION Rpl       !Plate radius
DOUBLE PRECISION Dpl       !Plate bending rigidity
DOUBLE PRECISION Mpl       !Plate mass per unit area
DOUBLE PRECISION Epl       !Plate Young's modulus
DOUBLE PRECISION Cpl       !Plate vibration damping factor
DOUBLE PRECISION mue       !Parameters for nozzle vib
DOUBLE PRECISION phi       !Parameters for nozzle vib
DOUBLE PRECISION Q         !Parameters for nozzle vib
DOUBLE PRECISION beta      !Parameters for nozzle vib
DOUBLE PRECISION wpl       !Nozzle deflection
DOUBLE PRECISION upl       !Nozzle velocity

DOUBLE PRECISION SQRCUT    !Minimum radius cutoff criteria
DOUBLE PRECISION SQRDIVCUT !Divergence criteria
DOUBLE PRECISION ZDCUT     !Node adding criteria
DOUBLE PRECISION ZCCUT     !Node deleting criteria
DOUBLE PRECISION dRdzcut   !Shape gradient cutoff value

CHARACTER PFUNC            !Pressure function slection character

COMMON /CONSTANT/ WR, Hpl, dT, Bo
COMMON /PRESSURE/ PFUNC, F_dr, T_pul, PMAX
COMMON /ARRLENG/ N, M, M_z, M_dz, N_dz, N_out
COMMON /VOLUME/ V_out, V_drop
COMMON /BREAKOFF/ SQRCUT, SQRDIVCUT, ZDCUT, ZCCUT, dRdzcut
COMMON /PLATE/ Rpl, Mpl, Dpl, Epl, Cpl
COMMON /LARGE/ mue, phi, Q, beta, wpl, upl

CALL INPUT(Rpl,Hpl,S_p,S_t,S_v,S_l,Dpl,Mpl,Epl,Cpl,WR,Bo)

PRINT*, 'INPUT PRESSURE MAGNITUDE IN PASSCAL'
READ*, P_i                !Dimensional pressure
PMAX=P_i/S_p
PRINT*, 'INPUT PRESSURE TYPE; S, SIN; C, COS; Q, SQUARE WAVE; &
      P, PULSING'
READ*, PFUNC

T_end = 10.0
dT = T_end/(NMAX)        !Time step for output file
CALL DRIPRE(PFUNC,S_t,F_dr,T_pul) !Define non-dimensional
presure function

print*, 'Input grid refinement parameter, integer'
! read*, M_dz                !For Convergence checking
M_dz = 16                !Grid refinement parameter
M_z = 20*M_dz*MMAX       !Total grid allable, control how far
the jet can be

```

```

N_dz = 400*M_dz**2/M_dz**0.5
M = M_dz*10+1
dT = dT/N_dz

ZDCUT = 0.16/M_dz          !Define the break-off criteria
ZCCUT = 0.06/M_dz
SQRCUT = 0.001
SQRDIVCUT = 5.0
! dRdzcut = 0.5*(4*SQRT(0.1*(2*1-0.1))-SQRT(0.2*(2*1-0.2)))/0.2
!For convergence check
dRdzcut = 0.5*(4*SQRT(0.1*(2*M_dz-0.1))-SQRT(0.2*(2*M_dz-    &
0.2)))/0.2
print*, dRdzcut

OPEN(11, FILE = 'CONSTANTS')
WRITE(11,*) S_p, S_t, S_v, S_l, WR, Bo, dT
CLOSE(11)          !Output of scales, We/Re, and dt

Bo = 0.0          !Neglect gravity
! Bo = 0.908726   !In Egger's Validation
! WR = 435.37     !In Egger's validation
WR=3.0*WR        !3 is the coeffieient in equation

CALL galerkincoe(Rpl) !Calculate the constants for G-L
Quadrature

OPEN(UNIT=51,FILE='breakinfo') !Break-off parameters
OPEN(UNIT=16,FILE='TIME')      !Time of each output
OPEN(UNIT=17,FILE='PRESSURE') !Pressure output, check correct
OPEN(UNIT=21,FILE='VOLUME')    !Volume output file
OPEN(UNIT=22,FILE='RADIUS')    !Element radius output file
OPEN(UNIT=23,FILE='ZLOCATION')  !Element position output file
OPEN(UNIT=24,FILE='VELOCITY')  !Element velocity output file
OPEN(UNIT=25,FILE='curvature') !Element surface tension output
OPEN(UNIT=26,FILE='orifice')   !Nozzle movement output file

ALLOCATE (U_j(M_z), SQR(M_z), Z(M_z))
ALLOCATE (Ustore_j(M_z), SQRstore(M_z), Zstore(M_z))

CALL INITIAL(U_j,SQR,Z)

CALL ONEDSOLUTION(U_j,SQR,Z)

Nstore=N

CALL BREAKOFFJET(U_j,SQR,Z,MD,Ustore_j,SQRstore,Zstore,MS)

M=MD
CALL DROPMOVE(U_j,SQR,Z)

U_j = Ustore_j(1:M_z)      !Simulate filament after brerak-off
SQR = SQRstore(1:M_z)
Z = Zstore(1:M_z)
M=MS;

```

```
N=Nstore
```

```
M=MS
```

```
CALL RESIDUE(U_j,SQR,Z)
```

```
DEALLOCATE (U_j, SQR, Z)
```

```
DEALLOCATE (Ustore_j, SQRstore, Zstore)
```

```
CLOSE(21);CLOSE(22);CLOSE(23);CLOSE(24);CLOSE(25);CLOSE(26)
```

```
CLOSE(51)
```

```
print*, N, M, M_z, N_dz
```

```
END
```

Subroutine: Initial

```

! SUBROUTINE INITIAL STAGE
SUBROUTINE INITIAL(U,SQR,Z)
INTEGER, PARAMETER :: NMAX=1E2, MMAX=20
DOUBLE PRECISION, PARAMETER :: PI=3.14159265358979
INTEGER N_rec          !Check if match output requirement
INTEGER N_dz
INTEGER M_z
INTEGER M_dz
INTEGER N_out          !Number of time series output executed
INTEGER N, M, I, J
DOUBLE PRECISION, DIMENSION(M_z):: U      !Element velocity
DOUBLE PRECISION, DIMENSION(M_z):: SQR    !Element radius square
DOUBLE PRECISION, DIMENSION(M_z):: Z
DOUBLE PRECISION, DIMENSION(M_z):: T_cur !Element pressure
DOUBLE PRECISION, DIMENSION(M_z):: y1     !Jet shape gradient
DOUBLE PRECISION, DIMENSION(M_z):: y2     !Jet shape curve
DOUBLE PRECISION WR, dT, L, Bo
DOUBLE PRECISION ZCEN, ZCENP
DOUBLE PRECISION UO, UO_old
DOUBLE PRECISION P_sur
DOUBLE PRECISION C_vo
DOUBLE PRECISION V_out, V_drop
DOUBLE PRECISION UOROUT, P ! FUNCTION
DOUBLE PRECISION Wori, Uori          !Nozzle deflection, velocity
DOUBLE PRECISION Zini                !Tip: end of early stage
DOUBLE PRECISION Tini                !Time: end of early stage
DOUBLE PRECISION SQRini              !Radius: end of early stage

COMMON /CONSTANT/ WR, L, dT, Bo

COMMON /ARRLENG/ N, M, M_z, M_dz, N_dz, N_out
COMMON /VOLUME/ V_out, V_drop

! *****
100 format(10000f30.25)          !Output format

N_out=1
ZCENP=0.0                        !Initial static condition

UO_old=0
P_sur=0.0

UO=(P(dT)+0.0-P_sur)*dT/(2*L)!First step
C_vol=2.0                        !Tip velocity:twice exit velocity
ZCEN=(UO+UO_old)*dT*C_vol/2      !Prediction
UO_old=UO

N=1

```

```

V_out = UO*PI*dT/2
V_drop = PI*(ZCEN/2+ZCEN**3/6)

SQR(1) = 0.0                !Zero tip radius
DO WHILE(ZCEN .LE. 1.0 .AND. N .LE. N_dz*NMAX)
  V_out = V_out+(UO_old+UO)*PI*dT/2
  V_drop = PI*(ZCEN/2+ZCEN**3/6)

  ZCENP=ZCEN+UO_old*dT/2
  P_sur=4*ZCENP/(ZCENP**2+1)
  C_vol=2/(1+ZCENP**2)
  UO=UORIOUT(N,UO_old,P_sur,dT,L)
  ZCEN=ZCEN+(UO+UO_old)*dT*C_vol/2
  UO_old=UO
! *****
!   U_g=Bo*dT                !Gravitational acceleration effect
   Uori = update(N)         !Nozzle vibration
   Wori = wplate(N)
! *****

  N_rec = mod(N,N_dz)

  IF (N_rec .eq. 0) then
    Z(1:M)=(/( (M-J)*ZCEN/(M-1),J=1,M)/)
    SQR(1:M)=1-Z(1:M)**2+(ZCEN-1/ZCEN)*Z(1:M)
    SQR(1)=0.0                !Avoid negative machine error
    U(1:M)=UO

    print*,N, N_out          !Print iterations and output number
    CALL CURVATURE(Z(1:M),SQR(1:M),M,T_cur(1:M),y1(1:M),y2(1:M))

    Z(M+1:M_z)=Z(M)         !Set to be trailing edge value
    SQR(M+1:M_z)=SQR(M)
    U(M+1:M_z)=U(M)
    T_cur(M+1:M_z)=T_cur(M)

    WRITE(16,100) N_out, N*dT
    WRITE(17,100) P(N*dT)
    WRITE(21,100) V_out, V_drop
    WRITE(22,100) SQR(SQR)  !Here the SQR is square of radius
    WRITE(23,100) Z
    WRITE(24,100) U
    WRITE(25,100) T_cur
    WRITE(26,100) Wori, Uori
    N_out=N_out+1
    END IF

    N=N+1

  END DO

Zini=ZCEN;Tini=N*dT;SQRini=0.0

WRITE(51,100) Zini, SQRini, Tini

```

```

Z(1:M)=(/( (M-J)*ZCEN/(M-1),J=1,M)/)
SQR(1:M)=1-Z(1:M)**2+(ZCEN-1/ZCEN)*Z(1:M)
SQR(1)=0.0
U(1:M)=UO

CALL CURVATURE(Z(1:M),SQR(1:M),M,T_cur(1:M),y1(1:M),y2(1:M))

Z(M+1:M_z)=Z(M)
SQR(M+1:M_z)=SQR(M)
U(M+1:M_z)=U(M)
T_cur(M+1:M_z)=T_cur(M)

SQR=SQRT(SQR)

WRITE(16,100) N_out*1.0, N*dt
WRITE(17,100) P(N*dt)
WRITE(21,100) V_out, V_drop
WRITE(22,100) SQR
WRITE(23,100) Z
WRITE(24,100) U
WRITE(25,100) T_cur
WRITE(26,100) Wori, Uori

print*,N,N_out

N_out=N_out+1
N=N-1
END SUBROUTINE INITIAL

```

Subroutine: Onedsolution

```

!THIS IS THE SUBROUTINE FOR ONE DIMENSIONAL MODELING FOR THE
DROPLET FORMATION
SUBROUTINE ONEDSOLUTION(U_j,SQR,Z)
  INTEGER, PARAMETER :: NMAX=1E2, MMAX=20
  DOUBLE PRECISION, PARAMETER :: PI=3.14159265358979
  INTEGER NC(1) !Element number to be deleted
  INTEGER ND(1) !Element number to be added
  INTEGER NB(1) !Break-off elemnt number
  INTEGER M, N, M_z, M_dz, N_dz, N_rec, N_out
  DOUBLE PRECISION ZI, SQRI, UI_j !Position, radius, velocity
  of added node

!Node properties
  DOUBLE PRECISION, DIMENSION(M_z) :: U_j
  DOUBLE PRECISION, DIMENSION(M_z) :: SQR
  DOUBLE PRECISION, DIMENSION(M_z) :: Z
  DOUBLE PRECISION, DIMENSION(M_z) :: T_cur
  DOUBLE PRECISION, DIMENSION(M_z) :: dU_j !Velocity gradient
  DOUBLE PRECISION, DIMENSION(M_z) :: LGSQR!Log10 of node radius
  DOUBLE PRECISION, DIMENSION(M_z) :: y1
  DOUBLE PRECISION, DIMENSION(M_z) :: y2

!Node properties by prediction step
  DOUBLE PRECISION, DIMENSION(M_z) :: UP_j
  DOUBLE PRECISION, DIMENSION(M_z) :: SQRP
  DOUBLE PRECISION, DIMENSION(M_z) :: TP_cur
  DOUBLE PRECISION, DIMENSION(M_z) :: dUP_j
  DOUBLE PRECISION, DIMENSION(M_z) :: LGSQRP
  DOUBLE PRECISION, DIMENSION(M_z) :: y1p
  DOUBLE PRECISION, DIMENSION(M_z) :: y2p

  DOUBLE PRECISION, DIMENSION(M_z) :: UOLD_j !Node velocity at
  previous time step

  DOUBLE PRECISION WR, dT, L, Bo
  DOUBLE PRECISION V_out, V_drop
  DOUBLE PRECISION SQRCUT !Minimum radius cutoff criteria
  DOUBLE PRECISION SQRDIVCUT !Divergence criteria
  DOUBLE PRECISION ZDCUT !Node adding criteria
  DOUBLE PRECISION ZCCUT !Node deleting criteria
  DOUBLE PRECISION dRdzcut !Maximum gradient resolvable
  DOUBLE PRECISION SQRCHE !Minimum radius
  DOUBLE PRECISION SQRDIVCHE !Maximum radius
  DOUBLE PRECISION ZDCHE !Maximum distance between nodes
  DOUBLE PRECISION ZCCHE !Minimum distance between nodes
  DOUBLE PRECISION dRdzche !Shape gradient
  DOUBLE PRECISION Zbreak !Break-off position
  DOUBLE PRECISION Tbreak !Break-off time
  DOUBLE PRECISION SQRbreak !Break-off radius
  DOUBLE PRECISION Wori, Uori
  DOUBLE PRECISION Uoriold !Nozzle velocity at last step
  DOUBLE PRECISION U_g

```

```

LOGICAL CRITERIA1, CRITERIA2           !Break-off criteria
LOGICAL CRITERIA3, CRITERIA4, CRITERIA5
LOGICAL CRITERIA

COMMON /CONSTANT/ WR, L, dT, Bo
COMMON /ARRENG/ N, M, M_z, M_dz, N_dz, N_out
COMMON /VOLUME/ V_out, V_drop
COMMON /BREAKOFF/ SQRCUT, SQRDIVCUT, ZDCUT, ZCCUT, dRdzcut

100 format(10000f30.25)           !Format for output
!*****
SQRCHE=1.0                         !Initial the checking values
ZDCHE=0.1/M_dz
ZCCHE=0.1/M_dz
SQRDIVCHE=1.0
dRdzche = 1.0

LGSQR=0                             !Initialize log10 radius
LGSQRP=0
SQRP(1)=SQR(1)

CRITERIA1 = SQRCHE .GE. SQRCUT
CRITERIA2 = SQRDIVCHE .LE. SQRDIVCUT
CRITERIA3 = dRdzche .LE. dRdzcut
CRITERIA4 = N .LE. N_dz*NMAX
CRITERIA5 = M .LT. M_z
print*, CRITERIA1, CRITERIA2, CRITERIA3, CRITERIA4

print*,N_dz*NMAX                   !Print the maximum time steps
Uoriold = update(N)                !Last step nozzle velocity
DO WHILE(CRITERIA1 .AND. CRITERIA2 .AND. CRITERIA3 .AND.
CRITERIA4 .AND. CRITERIA5)
  N=N+1
  LGSQR(2:M)=LOG(SQR(2:M))
  UOLD_j=U_j

                                     !Prediction time step
  CALL CURVATURE(Z(1:M),SQR(1:M),M,T_cur(1:M),y1(1:M),y2(1:M))

!Extrapolate surface tension near tip
  T_cur(1:5)=T_cur(6)+(Z(1:5)-Z(6))*(T_cur(8)-
                                     T_cur(4))/(Z(8)-Z(4))      &

  CALL GRADIENT(Z(1:M),U_j(1:M),M,dU_j(1:M))

  LGSQRP(2:M-1) = LGSQR(2:M-1)-(U_j(2:M-1)-
                                     U_j(3:M))*dT/(Z(2:M-1)-Z(3:M))/2      &

  UP_j(2:M-1) =U_j(2:M-1)-(T_cur(2:M-1)-WR*dU_j(2:M-1)-
                                     T_cur(3:M)+ WR*dU_j(3:M))*dT/(Z(2:M-1)-Z(3:M))      &

!Outlet BC

```

```

UP_j(M) = UORIOUT(N, U_j(M), T_cur(M), dT, L)

!Tip BC

UP_j(1) = UP_j(2) + (Z(1) - Z(2)) * (UP_j(3) - UP_j(2)) / (Z(3) - Z(2))

!Correction time step
SQRP(2:M-1) = EXP(LGSQRP(2:M-1))
SQRP(1) = SQR(1) !Tip radius keep same
SQRP(M) = 1
CALL
CURVATURE(Z(1:M), SQRP(1:M), M, TP_cur(1:M), y1p(1:M), y2p(1:M))
TP_cur(1:5) = TP_cur(6) + (Z(1:5) - Z(6)) * (TP_cur(8) - &
TP_cur(4)) / (Z(8) - Z(4))
CALL GRADIENT(Z(1:M), UP_j(1:M), M, dUP_j(1:M))
LGSQR(2:M-1) = (LGSQRP(2:M-1) + LGSQR(2:M-1)) / 2 - (UP_j(2:M-1) &
- UP_j(1:M-2)) * dT / (4 * (Z(2:M-1) - Z(1:M-2)))
U_j(2:M-1) = (U_j(2:M-1) + UP_j(2:M-1)) / 2 - (TP_cur(2:M-1) - &
WR * dUP_j(2:M-1) - TP_cur(1:M-2) + WR * dUP_j(1:M- &
2)) * dT / (2 * (Z(2:M-1) - Z(1:M-2)))

U_j(1) = U_j(2) + (Z(1) - Z(2)) * (U_j(3) - U_j(2)) / (Z(3) - Z(2))

!Tip BC
U_j(M) = UORIOUT(N, U_j(M), TP_cur(M), dT, L)

!Outlet BC

Wori = wplate(N) !Nozzle move
Uori = uplate(N)
U_g = Bo * dT !Gravitational

U_j(1:M-1) = U_j(1:M-1) - Uori + Uoriold !Incooperate nozzle
Uoriold = Uori
! U_j(1:M-1) = U_j(1:M-1) + U_g !Gravitational effect
(Eggers Validation)

Z(1:M-1) = Z(1:M-1) + (U_j(1:M-1) + UOLD_j(1:M-1)) * dT / 2
!Update position
Z(1) = 2 * Z(2) - Z(3)
Z(M) = 0
!Nozzle BC kept at zero

SQR(2:M-1) = EXP(LGSQR(2:M-1))
SQR(M) = 1

V_out = V_out + (UOLD_j(M) + U_j(M)) * PI * dT / 2
!Volume of fluid pushed out
V_drop = PI * DOT_PRODUCT(SQR(1:M-1) ** 2 + SQR(2:M) ** 2, Z(1:M-1) &
- Z(2:M)) / 2
!Volume of jet

ZCCHE = MINVAL(Z(1:M-1) - Z(2:M))
ZDCHE = MAXVAL(Z(1:M-1) - Z(2:M))

1010 IF (ZCCHE .GT. ZCCUT .AND. ZDCHE .LT. ZDCUT) THEN

```

```

!No node adding/deleting
ELSEIF (ZCCHE .LE. ZCCUT) THEN
    NC=MINLOC (Z (2:M-1) -Z (3:M))           !Delete node
    Z (NC (1) +1:M-1) =Z (NC (1) +2:M)
    Z (M) =0
    SQR (NC (1) +1:M-1) =SQR (NC (1) +2:M)
    SQR (M) =1.0
    U_j (NC (1) +1:M-1) =U_j (NC (1) +2:M)
    U_j (M) =0
    M=M-1
    ZCCHE=MINVAL (Z (1:M-1) -Z (2:M))
    GOTO 1010

ELSEIF (ZDCHE .GE. ZDCUT) THEN
    ND=MAXLOC (Z (1:M-1) -Z (2:M))           !Add node
    ZI = (Z (ND (1) +1) +Z (ND (1))) /2       !Mid point adding
    SQRI = (SQR (ND (1) +1) +SQR (ND (1))) /2 !Radius
    UI_j = (U_j (ND (1) +1) +U_j (ND (1))) /2 !Velocity

    Z (ND (1) +2:M+1) =Z (ND (1) +1:M)       !Reorder numbers
    Z (ND (1) +1) =ZI
    SQR (ND (1) +2:M+1) =SQR (ND (1) +1:M)
    SQR (ND (1) +1) =SQRI
    U_j (ND (1) +2:M+1) =U_j (ND (1) +1:M)
    U_j (ND (1) +1) =UI_j
    M=M+1

    ZDCHE=MAXVAL (Z (1:M-1) -Z (2:M))

    GOTO 1010
ELSE
    PRINT*, 'ANYTHING WRONG?'               !Unpredicted
    N=N-1
    goto 1020
ENDIF

N_rec = mod(N,N_dz)                          !Check for output
IF (N_rec .eq. 0) then
    Z (M+1:M_z) =Z (M)                       !Set to Nozzle exit
    SQR (M+1:M_z) =SQR (M)
    U_j (M+1:M_z) =U_j (M)
    T_cur (M+1:M_z) =T_cur (M)

    WRITE (16,100) N_out*1.0, N*dT
    WRITE (17,100) P (N*dT)
    WRITE (21,100) V_out, V_drop
    WRITE (22,100) SQR
    WRITE (23,100) Z
    WRITE (24,100) U_j
    WRITE (25,100) T_cur
    WRITE (26,100) Wori, Uori
    print*, N, N_out                          !Iteration, output
    print*, dRdzche, dRdzcut

```

```

      N_out=N_out+1
    END IF

    CALL CURVATURE(Z(1:M),SQR(1:M),M,T_cur(1:M),y1(1:M),y2(1:M))

    SQRCHE = MINVAL(SQR(2:M))           !Set break-off check value
    SQRDIVCHE = MAXVAL(SQR(1:M))       !Set divergence value
    dRdzche = MAXVAL(y1(2:M-100))

    CRITERIA1 = SQRCHE .GE. SQR CUT
    CRITERIA2 = SQRDIVCHE .LE. SQR DIV CUT
    CRITERIA3 = dRdzche .LE. 1*dRdzcut
    CRITERIA4 = N .LE. N_dz*NMAX
    CRITERIA5 = M .LT. M_z
    END DO

1020 NB=MINLOC(SQR(2:M-1))             !Find the braek-off node

    Zbreak = Z(NB(1)+1)
    SQRbreak = SQR(NB(1)+1)
    Tbreak = N*dT

    Z(M+1:M_z)=Z(M)
    SQR(M+1:M_z)=SQR(M)
    U_j(M+1:M_z)=U_j(M)
    T_cur(M+1:M_z)=T_cur(M)

    WRITE(16,100) N_out*1.0, N*dT
    WRITE(17,100) P(N*dT)
    WRITE(21,100) V_out, V_drop
    WRITE(22,100) SQR
    WRITE(23,100) Z
    WRITE(24,100) U_j
    WRITE(25,100) T_cur
    WRITE(26,100) Wori, Uori

    N_out=N_out+1
    WRITE(51,100) Zbreak, SQRbreak, Tbreak

!   print*, 'drop formation model ended'
!   Print*, N, M, ZCCHE, ZDCHE
!   print*, 'Break-off', SQR CHE .GE. SQR CUT
!   print*, 'Divergence', SQR DIV CHE .LE. SQR DIV CUT
!   Print*, 'Out of iteration permitted', N .LE. N_dz*NMAX
!   print*, 'high gradient', dRdzche .LE. dRdzcut
!   print*, 'Jet is too long', M .LT. M_z
!   print*, dRdzche, dRdzcut
    END SUBROUTINE ONEDSOLUTION

```

Subroutine: Breakoffjet

```

SUBROUTINE BREAKOFFJET(UD_j, SQRD, ZD, MD, US_j, SQRS, ZS, MS)
DOUBLE PRECISION, DIMENSION(M_z) :: UD_j
DOUBLE PRECISION, DIMENSION(M_z) :: SQRD
DOUBLE PRECISION, DIMENSION(M_z) :: ZD
DOUBLE PRECISION, DIMENSION(M_z) :: T_cur
DOUBLE PRECISION, DIMENSION(M_z) :: y1
DOUBLE PRECISION, DIMENSION(M_z) :: y2

DOUBLE PRECISION, DIMENSION(M_z) :: US_j
DOUBLE PRECISION, DIMENSION(M_z) :: SQRS
DOUBLE PRECISION, DIMENSION(M_z) :: ZS

INTEGER NS(1)           !Node number to be deleted
INTEGER ND(1)           !Node number to be added
INTEGER NB(1)           !Break-off node number
INTEGER MB1             !Number of nodes add by rounding
INTEGER I, J, MD, MS
INTEGER M, N, M_z, M_dz, N_dz, N_rec, N_out

DOUBLE PRECISION SQRCUT      !Minimum radius cutoff criteria
DOUBLE PRECISION dRdzcut     !Maximum gradient resolvable
DOUBLE PRECISION SQRCHE     !Minimum radius
DOUBLE PRECISION dRdzche     !Shape gradient

DOUBLE PRECISION SQRDIVCUT, ZDCUT, ZCCUT

DOUBLE PRECISION Zpichbc     !Leading edge to break-off pt
DOUBLE PRECISION Rpinch     !Spherical rounding radius
DOUBLE PRECISION Zcenpinch  !Center of the rounding sphere

COMMON /ARRLENG/ N, M, M_z, M_dz, N_dz, N_out
COMMON /BREAKOFF/ SQRCUT, SQRDIVCUT, ZDCUT, ZCCUT, dRdzcut

CALL CURVATURE(ZD(1:M), SQRD(1:M), M, T_cur(1:M), y1(1:M), y2(1:M))
dRdzche = MAXVAL (y1(2:M-100))
SQRCHE=MINVAL(SQRD(2:M_z))
print*,dRdzche, dRdzcut
print*,SQRCHE
if (SQRCHE .LE. SQRCUT) THEN !Break-off by minimum radius
  print*, 'break-off right for minimum radius reached'
  NB = MINLOC(SQRD(2:M)) + 1 !Avoid break-off at tip

  MB1 = NB(1)

  SQRD(NB(1)) = 0.0
  UD_j(NB(1)) = UD_j(NB(1)+1) !Satellite Drop

  ZS(1:M-MB1+1) = ZD(MB1:M) !Reorder element numbers

```

```

SQRS(1:M-MB1+1) = SQRD(MB1:M)
US_j(1:M-MB1+1) = UD_j(MB1:M)
ZS(M-MB1+2:M_z) = 0 !Set to be nozzle node value
SQRS(M-MB1+2:M_z)=1
US_j(M-MB1+2:M_z)=UD_j(M)
MS = M-MB1+1

UD_j(NB(1)) = UD_j(NB(1)-1) !For primary Drop

ZD(MB1+1:M_z)=ZD(MB1) !Trailing edge initial BC
SQRD(MB1+1:M_z)=SQRD(MB1)
UD_j(MB1+1:M_z)=UD_j(MB1)
MD = MB1
ELSE if (dRdzche .GE. 0.9*dRdzcut) then
!Break-off filament
ND = MAXLOC(SQRD(1:M/2)) !Avoid break-off at tip
NB = MINLOC(SQRD(ND(1):ND(1)+500))+ND(1)-1
If (ZD(NB(1)) .LE. 0.3) then
print*, 'Break-off near nozzle'
I = 0.3/ZCCUT
I = M - I
NB = MINLOC(SQRD(ND(1):I))
ELSE
END IF

Zpinchbc = SQRD(NB(1))
Rpinch = SQRD(NB(1))
Zcenpinch = ZD(NB(1))
MB1 = Zpinchbc*0.6/ZCCUT !Added element number
print*, 'Break-off information near trailing edge of
primary droplet'

ZS(NB(1):M_z) = ZD(NB(1):M_z)
SQRS(NB(1):M_z) = SQRD(NB(1):M_z)
US_j(NB(1):M_z) = UD_j(NB(1):M_z)
if (MB1 .ge. 1) then
Print*, 'REFINABLE RADIUS'
ZS(NB(1)-MB1:NB(1)-1)=ZD(NB(1)) +Zpinchbc - &
Zpinchbc/MB1*(((J-1)*1.0,J=1,MB1)/)
SQRS(NB(1)-MB1:NB(1)-1) = SQRT(Rpinch**2 - (ZS(NB(1)- &
MB1:NB(1)-1)-Zcenpinch)**2)

SQRS(NB(1)-MB1) = 0.0 !Set leading edge zero radius
US_j(NB(1)-MB1:NB(1)-1) = UD_j(NB(1))
else
print*, 'RADIUS IS SMALL ENOUGH'
ZS(NB(1)) = ZD(NB(1))
SQRS(NB(1)) = 0.0
US_j(NB(1)) = UD_j(NB(1)+1)
Endif

MB1 = NB(1)-MB1
ZS(1:M-MB1+1) = ZS(MB1:M) !Reorder element numbers

```

```

SQRS(1:M-MB1+1)=SQRS(MB1:M)
US_j(1:M-MB1+1)=US_j(MB1:M)

ZS(M-MB1+2:M_z) = 0           !Set to be nozzle node value
SQRS(M-MB1+2:M_z)=1
US_j(M-MB1+2:M_z)=US_j(M)

MS= M-MB1+1

                                !BREAK-OFF OF MAIN DROP
NB=MAXLOC(y1(1:M-100))
Zpinchbc = SQRD(NB(1))*(SQRT(y1(NB(1))**2+1) -
                                abs(y1(NB(1))))           &
Rpinch = SQRD(NB(1))*SQRT(y1(NB(1))**2+1)
Zcenpinch = ZD(NB(1)) - Zpinchbc + Rpinch

MB1 = Zpinchbc*0.6/ZCCUT       !Added element number

if (MB1 .ge. 1) then
  ZD(NB(1)+1:NB(1)+MB1) = ZD(NB(1)) -
                                Zpinchbc/MB1*(/(J*1.0,J=1,MB1)/) &
  SQRD(NB(1)+1:NB(1)+MB1) = SQRT(Rpinch**2 -
                                (ZD(NB(1)+1:NB(1)+MB1)-Zcenpinch)**2) &

  SQRD(NB(1)+MB1) = 0.0       !Set leading edge zero radius
  UD_j(NB(1)+1:NB(1)+MB1) = UD_j(NB(1))
else
  print*, 'break-off right at tip'
  ZD(NB(1)) = ZD(NB(1)) - ZCCUT/0.6
  SQRD(NB(1)) = 0.0
  UD_j(NB(1)) = UD_j(NB(1))
Endif

MD=NB(1)+MB1

ZD(MD+1:M_z)=ZD(MD)           !Trailing edge initial BC
SQRD(MD+1:M_z)=SQRD(MD)
UD_j(MD+1:M_z)=UD_j(MD)

ELSE
  print*, 'break-off information is wrong'
  stop
ENDIF
END SUBROUTINE BREAKOFFJET

```

Subroutine: Dropmove

```

! SUBROUTINE AFTER BREAK-OFF HAPPEN
SUBROUTINE DROPMOVE(U_j,SQR,Z)
INTEGER, PARAMETER :: NMAX=1E2, MMAX=20
DOUBLE PRECISION, PARAMETER :: PI=3.14159265358979
INTEGER NC(1) !Node number to be deleted
INTEGER ND(1) !Node number to be added
INTEGER NB(1) !Break-off node number
INTEGER MB1 !Number of nodes add by rounding
INTEGER I, J
INTEGER M, N, M_z, M_dz, N_dz, N_rec, N_out
DOUBLE PRECISION ZI, SQRI, UI_j
!Node properties
DOUBLE PRECISION, DIMENSION(M_z) :: U_j
DOUBLE PRECISION, DIMENSION(M_z) :: SQR
DOUBLE PRECISION, DIMENSION(M_z) :: Z
DOUBLE PRECISION, DIMENSION(M_z) :: T_cur
DOUBLE PRECISION, DIMENSION(M_z) :: dU_j !Velocity gradient
DOUBLE PRECISION, DIMENSION(M_z) :: LGSQR !Log10: node radius
DOUBLE PRECISION, DIMENSION(M_z) :: y1
DOUBLE PRECISION, DIMENSION(M_z) :: y2
!Node properties by prediction step

DOUBLE PRECISION, DIMENSION(M_z) :: UP_j
DOUBLE PRECISION, DIMENSION(M_z) :: SQRP
DOUBLE PRECISION, DIMENSION(M_z) :: TP_cur
DOUBLE PRECISION, DIMENSION(M_z) :: dUP_j
DOUBLE PRECISION, DIMENSION(M_z) :: LGSQRP
DOUBLE PRECISION, DIMENSION(M_z) :: y1p
DOUBLE PRECISION, DIMENSION(M_z) :: y2p

DOUBLE PRECISION, DIMENSION(M_z) :: UOLD_j!Velocity last step
DOUBLE PRECISION WR, dT, L, Bo
DOUBLE PRECISION V_out, V_drop
DOUBLE PRECISION SQR CUT !Minimum radius criteria
DOUBLE PRECISION SQRDIVCUT !Divergence criteria
DOUBLE PRECISION ZDCUT !Node adding criteria
DOUBLE PRECISION ZCCUT !Node deleting criteria
DOUBLE PRECISION dRdzcut !Maximum gradient resolvable
DOUBLE PRECISION SQRCHE !Minimum radius
DOUBLE PRECISION SQRDIVCHE !Maximum radius
DOUBLE PRECISION ZDCHE !Maximum distance at nodes
DOUBLE PRECISION ZCCHE !Minimum distance at nodes
DOUBLE PRECISION dRdzche !Shape gradient
DOUBLE PRECISION Zbreak !Break-off position
DOUBLE PRECISION Tbreak !Break-off time
DOUBLE PRECISION SQRbreak !Break-off radius

DOUBLE PRECISION Ztip !Droplet tip position

```

```

DOUBLE PRECISION Wori, Uori
DOUBLE PRECISION Uoriold           !Nozzle velocity last step
DOUBLE PRECISION U_g

LOGICAL CRITERIA1, CRITERIA2, CRITERIA3 !Break-off criteria
LOGICAL CRITERIA4, CRITERIA5, CRITERIA6

COMMON /CONSTANT/ WR, L, dT, Bo
COMMON /ARRLENG/ N, M, M_z, M_dz, N_dz, N_out
COMMON /VOLUME/ V_out, V_drop
COMMON /BREAKOFF/ SQRCUT, SQRDIVCUT, ZDCUT, ZCCUT, dRdzcut

100  format(10000f30.25)           !Format for output

CALL CURVATURE(Z(1:M),SQR(1:M),M,T_cur(1:M),y1(1:M),y2(1:M))

WRITE(16,100) N_out*1.0, N*dT
WRITE(17,100) P(N*dT)
WRITE(21,100) V_out, V_drop
WRITE(22,100) SQR
WRITE(23,100) Z
WRITE(24,100) U_j
WRITE(25,100) T_cur
!*****
SQRCHE=1.0
ZDCHE=0.1/M_dz
ZCCHE=0.1/M_dz
SQRDIVCHE=1.0

dRdzche = 1.0
Ztip = Z(1)
I = N

CRITERIA1 = SQRCHE .GE. SQRCUT
CRITERIA2 = SQRDIVCHE .LE. SQRDIVCUT
CRITERIA3 = dRdzche .LE. 2*dRdzcut
CRITERIA4 = I .LE. N_dz*NMAX
CRITERIA5 = Ztip .LE. 50.0
CRITERIA6 = M .LT. M_z
print*, 'begin drop move modeling'
print*, N_dz*NMAX, Ztip

DO WHILE(CRITERIA1 .AND. CRITERIA2 .AND. CRITERIA3 .AND.      &
         CRITERIA4 .AND. CRITERIA5 .AND. CRITERIA6)
  I=I+1
  LGSQR(2:M-1)=LOG(SQR(2:M-1))
  UOLD_j=U_j

!Prediction time step
  CALL CURVATURE(Z(1:M),SQR(1:M),M,T_cur(1:M),y1(1:M),y2(1:M))

  !Extrapolate surface tension near tip
  T_cur(1:5) = T_cur(6)+(Z(1:5)-Z(6))*(T_cur(8)-      &

```

```

          T_cur(4))/(Z(8)-Z(4))
T_cur(M-4:M) = T_cur(M-5)+(Z(M-4:M)-Z(M-5))*(T_cur(M-7)- &
          T_cur(M-3))/(Z(M-7)-Z(M-3))
CALL GRADIENT(Z(1:M),U_j(1:M),M,dU_j(1:M))
LGSQRP(2:M-1) = LGSQR(2:M-1)-(U_j(2:M-1)- &
          U_j(3:M))*dT/(Z(2:M-1)-Z(3:M))/2
UP_j(2:M-1) = U_j(2:M-1)-(T_cur(2:M-1)-WR*dU_j(2:M-1)- &
          T_cur(3:M)+ WR*dU_j(3:M))*dT/(Z(2:M-1)-Z(3:M))

UP_j(M) = UP_j(M-1)           !Trailing Edge BC
UP_j(1) = UP_j(2)           !Leading Edge BC

!Correction time step
SQRP(2:M-1)=EXP(LGSQRP(2:M-1))
SQRP(1)=SQR(1)
SQRP(M)=SQR(M)
CALL
CURVATURE(Z(1:M),SQRP(1:M),M,TP_cur(1:M),y1p(1:M),y2p(1:M)) &
TP_cur(1:5) = TP_cur(6)+(Z(1:5)-Z(6))*(TP_cur(8)- &
          TP_cur(4))/(Z(8)-Z(4))
TP_cur(M-4:M) = TP_cur(M-5)+(Z(M-4:M)-Z(M-5))*(TP_cur(M-7)&
          - TP_cur(M-3))/(Z(M-7)-Z(M-3))
CALL GRADIENT(Z(1:M),UP_j(1:M),M,dUP_j(1:M))
LGSQR(2:M-1) = (LGSQRP(2:M-1)+LGSQR(2:M-1))/2-(UP_j(2:M-1)&
          - UP_j(1:M-2))*dT/4*(Z(2:M-1)-Z(1:M-2))
U_j(2:M-1) = (U_j(2:M-1)+UP_j(2:M-1))/2-(TP_cur(2:M-1)- &
          WR*dUP_j(2:M-1)- TP_cur(1:M-2)+WR*dUP_j(1:M- &
          2))*dT/(2*(Z(2:M-1)-Z(1:M-2)))

U_j(1)=U_j(2)           !Leading Edge BC
U_j(M)=U_j(M-1)       !Trailing Edge BC

Z(1:M)=Z(1:M)+(U_j(1:M)+UOLD_j(1:M))*dT/2 !Update position
Z(1) = 2*Z(2)-Z(3)
Z(M) = 2*Z(M-1)-Z(M-2)           !Trailing edge

SQR(2:M-1)=EXP(LGSQR(2:M-1))
SQR(M)=SQR(M)

V_drop = PI*DOT_PRODUCT(SQR(1:M-1)**2+SQR(2:M)**2,Z(1:M-1)&
          - Z(2:M))/2 !Drop volume
!
ZCCHE=MINVAL(Z(1:M-1)-Z(2:M))           !Set deleting value
ZDCHE=MAXVAL(Z(1:M-1)-Z(2:M))           !Set adding value

1010 IF (ZCCHE .GT. ZCCUT .AND. ZDCHE .LT. ZDCUT) THEN
!No node adding/deleting
      ELSEIF (ZCCHE .LE. ZCCUT) THEN
          NC=MINLOC(Z(2:M-1)-Z(3:M))           !Delete node
          Z(NC(1)+1:M-1)=Z(NC(1)+2:M)
          Z(M)=0
          SQR(NC(1)+1:M-1)=SQR(NC(1)+2:M)

```

```

SQR(M)=1.0
U_j(NC(1)+1:M-1)=U_j(NC(1)+2:M)
U_j(M)=0
M=M-1
ZCICHE=MINVAL(Z(1:M-1)-Z(2:M)) !Set deleting value

GOTO 1010
ELSEIF (ZCICHE .GE. ZDCUT) THEN
    ND=MAXLOC(Z(1:M-1)-Z(2:M)) !Add node
    ZI = (Z(ND(1)+1)+Z(ND(1)))/2 !Mid point adding
    SQRI = (SQR(ND(1)+1)+SQR(ND(1)))/2
    UI_j = (U_j(ND(1)+1)+U_j(ND(1)))/2

    Z(ND(1)+2:M+1)=Z(ND(1)+1:M)
    Z(ND(1)+1)=ZI
    SQR(ND(1)+2:M+1)=SQR(ND(1)+1:M)
    SQR(ND(1)+1)=SQRI
    U_j(ND(1)+2:M+1)=U_j(ND(1)+1:M)
    U_j(ND(1)+1)=UI_j
    M=M+1

    ZDCICHE=MAXVAL(Z(1:M-1)-Z(2:M))!Set adding value

    GOTO 1010
ELSE
    PRINT*, 'ANYTHING WRONG?' !Unpredicted
    N=N-1
    goto 1020
ENDIF

N_rec = mod(I,N_dz) !Check for output
IF (N_rec .eq. 0) then
    Z(M:M_z)=Z(M) !Set to Nozzle values
    SQR(M:M_z)=SQR(M)
    U_j(M:M_z)=U_j(M)
    T_cur(M:M_z)=T_cur(M)

    WRITE(16,100) N_out*1.0, I*dT
    WRITE(17,100) P(I*dT)
    WRITE(21,100) V_out, V_drop
    WRITE(22,100) SQR
    WRITE(23,100) Z
    WRITE(24,100) U_j
    WRITE(25,100) T_cur
    ! print*, I, N_out
    ! print*, dRdzche, 10*dRdzcut
    N_out=N_out+1
END IF

SQRICHE=MINVAL(SQR(2:M-1)) !Set break-off value
SQRDIVICHE=MAXVAL(SQR(1:M)) !Set divergence value
Ztip = Z(1) !Check tip position
dRdzche = MAXVAL (y1(2:M-1))

```

```

CRITERIA1 = SQRCHE .GE. SQRCUT
CRITERIA2 = SQRDIVCHE .LE. SQRDIVCUT
CRITERIA3 = dRdzche .LE. 10*dRdzcut
CRITERIA4 = I .LE. N_dz*NMAX
CRITERIA5 = Ztip .LE. 50.0
CRITERIA6 = M .LT. M_z
END DO

1020 NB=MINLOC(SQR(2:M-1))           !Find break-off node
Zbreak = Z(NB(1)+1)
SQRbreak = SQR(NB(1)+1)
Tbreak = I*dt

WRITE(51,100) Zbreak, SQRbreak, Tbreak

Z(M:M_z)=Z(M)
SQR(M:M_z)=SQR(M)
U_j(M:M_z)=U_j(M)
T_cur(M:M_z)=T_cur(M)

WRITE(16,100) N_out*1.0, I*dt
WRITE(17,100) P(I*dt)
WRITE(21,100) V_out, V_drop
WRITE(22,100) SQR
WRITE(23,100) Z
WRITE(24,100) U_j
WRITE(25,100) T_cur
N_out=N_out+1
!
! Print*, I, M, ZCCHE, ZDCHE
! print*, 'Moved too far', Ztip .le. 50.0
! print*, 'Jet too long', M .LE. M_z
! print*, 'break-off again', SQRCHE .GE. SQRCUT
! print*, 'diverge', SQRDIVCHE .LE. SQRDIVCUT
! print*, 'time to stop', I .LE. N_dz*NMAX
! print*, 'high gradient', dRdzche .LE. 10*dRdzcut
! print*, dRdzche, 10*dRdzcut
END SUBROUTINE DROPMOVE

```

Subroutine: Residue

```

! SUBROUTINE AFTER BREAK-OFF HAPPEN
SUBROUTINE RESIDUE(U_j,SQR,Z)
INTEGER, PARAMETER :: NMAX=1E2, MMAX=20
DOUBLE PRECISION, PARAMETER :: PI=3.14159265358979
INTEGER NC(1) !Node number to be deleted
INTEGER ND(1) !Node number to be added
INTEGER NB(1) !Break-off node number
INTEGER MB1 !Node Number added rounding
INTEGER I, J
INTEGER M, N, M_z, M_dz, N_dz, N_rec, N_out
DOUBLE PRECISION ZI, SQRI, UI_j
!Node properties
DOUBLE PRECISION, DIMENSION(M_z) :: U_j
DOUBLE PRECISION, DIMENSION(M_z) :: SQR
DOUBLE PRECISION, DIMENSION(M_z) :: Z
DOUBLE PRECISION, DIMENSION(M_z) :: T_cur
DOUBLE PRECISION, DIMENSION(M_z) :: dU_j !Velocity gradient
DOUBLE PRECISION, DIMENSION(M_z) :: LGSQR !Log10 of radius
DOUBLE PRECISION, DIMENSION(M_z) :: y1
DOUBLE PRECISION, DIMENSION(M_z) :: y2
!Node properties by prediction step
DOUBLE PRECISION, DIMENSION(M_z) :: UP_j
DOUBLE PRECISION, DIMENSION(M_z) :: SQRP
DOUBLE PRECISION, DIMENSION(M_z) :: TP_cur
DOUBLE PRECISION, DIMENSION(M_z) :: dUP_j
DOUBLE PRECISION, DIMENSION(M_z) :: LGSQRP
DOUBLE PRECISION, DIMENSION(M_z) :: y1p
DOUBLE PRECISION, DIMENSION(M_z) :: y2p

DOUBLE PRECISION, DIMENSION(M_z) :: UOLD_j! Velocity last step
DOUBLE PRECISION WR, dT, L, Bo
DOUBLE PRECISION V_out, V_drop
DOUBLE PRECISION SQRCUT !Minimum radius cutoff
DOUBLE PRECISION SQRDIVCUT !Divergence criteria
DOUBLE PRECISION ZDCUT !Node adding criteria
DOUBLE PRECISION ZCCUT !Node deleting criteria
DOUBLE PRECISION dRdzcut !Maximum shape gradient
DOUBLE PRECISION SQRCHE !Minimum radius
DOUBLE PRECISION SQRDIVCHE !Maximum radius
DOUBLE PRECISION ZDCHE !Maximum distance at nodes
DOUBLE PRECISION ZCCHE !Minimum distance at nodes
DOUBLE PRECISION dRdzche !Shape gradient
DOUBLE PRECISION Zbreak !Break-off position
DOUBLE PRECISION Tbreak !Break-off time
DOUBLE PRECISION SQRbreak !Break-off radius

DOUBLE PRECISION Ztip !Filament tip position
DOUBLE PRECISION Wori, Uori

```

```

DOUBLE PRECISION Uoriold           !Nozzle velocity last step
DOUBLE PRECISION U_g

LOGICAL CRITERIA1, CRITERIA2, CRITERIA3 !Break-off criterias
LOGICAL CRITERIA4, CRITERIA5, CRITERIA6

COMMON /CONSTANT/ WR, L, dT, Bo
COMMON /ARRLENG/ N, M, M_z, M_dz, N_dz, N_out
COMMON /VOLUME/ V_out, V_drop
COMMON /BREAKOFF/ SQRCUT, SQRDIVCUT, ZDCUT, ZCCUT, dRdzcut

100 format(10000f30.25)           !Format for output

CALL CURVATURE(Z(1:M),SQR(1:M),M,T_cur(1:M),y1(1:M),y2(1:M))

WRITE(16,100) N_out*1.0, N*dT      !The start of Filament
WRITE(17,100) P(N*dT)
WRITE(21,100) V_out, V_drop
WRITE(22,100) SQR
WRITE(23,100) Z
WRITE(24,100) U_j
WRITE(25,100) T_cur
Print*, M, NB, MBl
! *****

SQRCHE=1.0
ZDCHE=0.1/M_dz
ZCCHE=0.1/M_dz
SQRDIVCHE=1.0
dRdzche = 1.0
Ztip = Z(1)
I=N

CRITERIA1 = SQRCHE .GE. SQRCUT
CRITERIA2 = SQRDIVCHE .LE. SQRDIVCUT
CRITERIA3 = dRdzche .LE. dRdzcut
CRITERIA4 = I .LE. N_dz*NMAX
CRITERIA5 = Ztip .GE. 1.0 .AND. Ztip .LE. 40.0
CRITERIA6 = M .LT. M_z
print*, 'begin filament modeling'
print*,N_dz*NMAX, Ztip
Uoriold = uplate(N)                !Last step nozzle velocity
DO WHILE(CRITERIA1 .AND. CRITERIA2 .AND. CRITERIA3           &
        .AND. CRITERIA4 .AND. CRITERIA5 .AND. CRITERIA6)
    I=I+1
    LGSQR(2:M-1)=LOG(SQR(2:M-1))
    UOLD_j=U_j

!Prediction time step
CALL CURVATURE(Z(1:M),SQR(1:M),M,T_cur(1:M),y1(1:M),y2(1:M))

T_cur(1:5) = T_cur(6)+(Z(1:5)-Z(6))*(T_cur(8)-           &
        T_cur(4))/(Z(8)-Z(4))
CALL GRADIENT(Z(1:M),U_j(1:M),M,dU_j(1:M))

```

```

LGSQRP(2:M-1) = LGSQR(2:M-1) - (U_j(2:M-1) - U_j(3:M)) * dT /      &
                (Z(2:M-1) - Z(3:M)) / 2

UP_j(2:M-1) = U_j(2:M-1) - (T_cur(2:M-1) - WR*dU_j(2:M-1) -      &
                T_cur(3:M) + WR*dU_j(3:M)) * dT / (Z(2:M-1) - Z(3:M))

UP_j(M) = UORIOUT(N, U_j(M), T_cur(M), dT, L)      !Outlet BC
UP_j(1) = UP_j(2)      !Tip BC
!Correction time step
SQRP(2:M-1) = EXP(LGSQRP(2:M-1))
SQRP(1) = SQR(1)      !Tip radius
SQRP(M) = 1      !Nozzle node

CALL
CURVATURE(Z(1:M), SQRP(1:M), M, TP_cur(1:M), y1p(1:M), y2p(1:M))      &
TP_cur(1:5) = TP_cur(6) + (Z(1:5) - Z(6)) * (TP_cur(8) -      &
                TP_cur(4)) / (Z(8) - Z(4))
CALL GRADIENT(Z(1:M), UP_j(1:M), M, dUP_j(1:M))
LGSQR(2:M-1) = (LGSQRP(2:M-1) + LGSQR(2:M-1)) / 2 - (UP_j(2:M-1) &
                - UP_j(1:M-2)) * dT / (4 * (Z(2:M-1) - Z(1:M-2)))
U_j(2:M-1) = (U_j(2:M-1) + UP_j(2:M-1)) / 2 - (TP_cur(2:M-1) -      &
                WR*dUP_j(2:M-1) - TP_cur(1:M-2) + WR*dUP_j(1:M-      &
                2)) * dT / (2 * (Z(2:M-1) - Z(1:M-2)))

U_j(1) = U_j(2)      !Tip BC
U_j(M) = UORIOUT(N, U_j(M), TP_cur(M), dT, L)      !Outlet BC

Wori = wplate(I)      !Nozzle move
Uori = uplate(I)
U_g = Bo * dT      !Gravity
! U_j(1:M-1) = U_j(1:M-1) - Uori + Uoriold      !Incorporate nozzle
Uoriold = Uori
U_j(1:M-1) = U_j(1:M-1) + U_g      !Incorporate gravity

Z(1:M-1) = Z(1:M-1) + (U_j(1:M-1) + UOLD_j(1:M-1)) * dT / 2
Z(M) = 0
Z(1) = 2 * Z(2) - Z(3)

SQR(2:M-1) = EXP(LGSQR(2:M-1))
SQR(M) = 1

V_out = V_out + (UOLD_j(M) + U_j(M)) * PI * dT / 2
V_drop = PI * DOT_PRODUCT(SQR(1:M-1) ** 2 + SQR(2:M) ** 2, Z(1:M-1) &
                - Z(2:M)) / 2
ZCCHE = MINVAL(Z(1:M-1) - Z(2:M))      !Set node deleting value
ZDCHE = MAXVAL(Z(1:M-1) - Z(2:M))      !Set node adding value

1010 IF (ZCCHE .GT. ZCCUT .AND. ZDCHE .LT. ZDCUT) THEN
!No node adding/deleting
    ELSEIF (ZCCHE .LE. ZCCUT) THEN
        NC = MINLOC(Z(2:M-1) - Z(3:M))      !Delete node
        Z(NC(1) + 1:M-1) = Z(NC(1) + 2:M)
        Z(M) = 0

```

```

SQR(NC(1)+1:M-1)=SQR(NC(1)+2:M)
SQR(M)=1.0
U_j(NC(1)+1:M-1)=U_j(NC(1)+2:M)
U_j(M)=0
M=M-1
ZCCHE=MINVAL(Z(1:M-1)-Z(2:M)) !Node deleting value

GOTO 1010
ELSEIF (ZCCHE .GE. ZDCUT) THEN
  ND=MAXLOC(Z(1:M-1)-Z(2:M)) !Add node
  ZI = (Z(ND(1)+1)+Z(ND(1)))/2
  SQRI = (SQR(ND(1)+1)+SQR(ND(1)))/2
  UI_j = (U_j(ND(1)+1)+U_j(ND(1)))/2

  Z(ND(1)+2:M+1)=Z(ND(1)+1:M) !Reorder numbers
  Z(ND(1)+1)=ZI
  SQR(ND(1)+2:M+1)=SQR(ND(1)+1:M)
  SQR(ND(1)+1)=SQRI
  U_j(ND(1)+2:M+1)=U_j(ND(1)+1:M)
  U_j(ND(1)+1)=UI_j
  M=M+1

  ZDCHE=MAXVAL(Z(1:M-1)-Z(2:M))!Node adding value

  GOTO 1010
ELSE
  PRINT*, 'ANYTHING WRONG?' !Unpredicted
  N=N-1
  goto 1020
ENDIF

N_rec = mod(I,N_dz) !Check match output

IF (N_rec .eq. 0) then
  Z(M+1:M_z)=Z(M) !Set to Nozzle value
  SQR(M+1:M_z)=SQR(M)
  U_j(M+1:M_z)=U_j(M)
  T_cur(M+1:M_z)=T_cur(M)

  WRITE(16,100) N_out*1.0, I*dt
  WRITE(17,100) P(I*dt)
  WRITE(21,100) V_out, V_drop
  WRITE(22,100) SQR
  WRITE(23,100) Z
  WRITE(24,100) U_j
  WRITE(25,100) T_cur
  WRITE(26,100) Wori, Uori
  print*,I, N_out
  print*, dRdzche, dRdzcut
  N_out=N_out+1
END IF

SQRCHE=MINVAL(SQR(2:M))
SQRDIVCHE=MAXVAL(SQR(1:M))

```

```

Ztip = Z(1)
dRdzche = MAXVAL (y1(2:M))

CRITERIA1 = SQRCHE .GE. SQRCUT
CRITERIA2 = SQRDIVCHE .LE. SQRDIVCUT
CRITERIA3 = dRdzche .LE. dRdzcut
CRITERIA4 = I .LE. N_dz*NMAX
CRITERIA5 = Ztip .GE. 1.0 .AND. Ztip .LE. 40.0
CRITERIA6 = M .LT. M_z
END DO

1020 NB=MINLOC(SQR(2:M-1))           !Find braek-off node
Zbreak = Z(NB(1)+1)
SQRbreak = SQR(NB(1)+1)
Tbreak = I*dt

Z(M+1:M_z)=Z(M)
SQR(M+1:M_z)=SQR(M)
U_j(M+1:M_z)=U_j(M)
T_cur(M+1:M_z)=T_cur(M)

WRITE(16,100) N_out*1.0, I*dt
WRITE(17,100) P(I*dt)
WRITE(21,100) V_out, V_drop
WRITE(22,100) SQR
WRITE(23,100) Z
WRITE(24,100) U_j
WRITE(25,100) T_cur
WRITE(26,100) Wori, Uori

N_out=N_out+1
WRITE(51,100) Zbreak, SQRbreak, Tbreak

print*, 'filament model ended'
Print*, I, M, ZCCHE, ZDCHE
print*, 'Retreat to nozzle', Ztip .GE. 1.0 .AND. Ztip .LE. 30
print*, 'break-off satellite', SQRCHE .GE. SQRCUT
print*, 'diverge', SQRDIVCHE .LE. SQRDIVCUT
print*, 'out of iteration permitted', I .LE. N_dz*NMAX
print*, 'high gradient', dRdzche .LE. dRdzcut
print*, dRdzche, dRdzcut
print*, 'Jet is too long', M .LT. M_z
N=I
END SUBROUTINE RESIDUE

```

Subroutine: Input

```

! SUBROUTINE FOR INPUT VARIABLES
SUBROUTINE INPUT(R,L,S_p,S_t,S_v,S_l,D,M,E,C,WR,Bo)
DOUBLE PRECISION Den_w !Fluid density
DOUBLE PRECISION Segma !Fluid surface tension
DOUBLE PRECISION Nv !Fluid dynamics viscosity
DOUBLE PRECISION g_z !Gravity acceleration
DOUBLE PRECISION R_o !Nozzle radius
DOUBLE PRECISION R_pl !Dimensional plate radius
DOUBLE PRECISION Thi_pl !Dimensional plate thickness
DOUBLE PRECISION Nu !Plate poisson ratio
DOUBLE PRECISION E_pl !Dimensional plate Young modulus
DOUBLE PRECISION Den_pl !Dimensional plate density
DOUBLE PRECISION C_i !Dimensional plate vib damping factor
DOUBLE PRECISION S_p !Scales, output to main program
DOUBLE PRECISION S_t
DOUBLE PRECISION S_v
DOUBLE PRECISION S_l
DOUBLE PRECISION WR !We/Re, viscous effect
DOUBLE PRECISION Bo !Bond number, gravity
DOUBLE PRECISION R !Non-dimensional plate radius
DOUBLE PRECISION L !Non-dimensional plate thickness
DOUBLE PRECISION D !Non-dimensional plate rigidity
DOUBLE PRECISION M !Non-dimensional plate mass per area

DOUBLE PRECISION E !Non-dimensional Young's modulus
DOUBLE PRECISION C !Non-dimensional vibration damping

Den_w=998.0
Sigma=0.0728
g_z=9.8
R_o=5.0E-5
R_pl=4.0E-3
Nu=0.35
C_i=27.8 !equivilent to non-dimensional C=0.05

print*,'Input fluid density, times of water'
read*,Nv !Times that of water
Nv=Nv*1.02E-3

print*,'Input plate thickness, in micro'
read*,Thi_pl
Thi_pl=Thi_pl*1.0E-6 !Change to unit in meter

print*,'Input plate density, in kg/m^3'
read*,Den_pl

print*,'Input plate Young modulus, in Gpa'

```

```
read*,E_pl
E_pl=E_pl*1.0E9           !Change to unit in meter

S_l=R_o
S_t=sqrt(Den_w*R_o**3/Sigma)
S_v=sqrt(Sigma/(Den_w*R_o))
S_p=Sigma/R_o

R=R_pl/S_l
L=Thi_pl/S_l
E=E_pl/S_p
D=E*L**3/(12*(1-Nu**2))
M=Den_pl*L/Den_w
C=C_i*S_l/(S_t*S_p)
WR=Nv/(Den_w*S_v*R_o)
Bo=Den_w*g_z*R_o**2/Sigma
END SUBROUTINE INPUT
```

Subroutine: Dripre

```

! Define the pressure input you like
SUBROUTINE DRIPRE(PFUNC,S_t,F,T_pul)
INTEGER N, I, J
DOUBLE PRECISION S_t      !Time scale
DOUBLE PRECISION F_i      !Frequency input
DOUBLE PRECISION F        !Non-dimensional frequency
DOUBLE PRECISION T_pul    !Non-dimensional pusle width
CHARACTER PFUNC           !Pressure function selector

IF (PFUNC .EQ. 'S') THEN
  PRINT*, 'INPUT PRESSURE FREQUENCY'
  READ*, F_i
  F = F_i*S_t
ELSEIF (PFUNC .EQ. 'C') THEN
  PRINT*, 'INPUT PRESSURE FREQUENCY'
  READ*, F_i
  F = F_i*S_t
ELSEIF (PFUNC .EQ. 'Q') THEN
  PRINT*, 'INPUT PRESSURE FREQUENCY'
  READ*, F_i
  F = F_i*S_t
ELSEIF (PFUNC .EQ. 'P') THEN
  PRINT*, 'INPUT PULSING PRESSURE TIME WIDTH'
  READ*, T_pul
ELSE
  PRINT*, 'INPUT IS WRONG'
END IF
36  END SUBROUTINE DRIPRE

```

Subroutine: Curvature

```

SUBROUTINE CURVATURE(x,y,M,T_cur,y1,y2)

INTEGER M,I,K
DOUBLE PRECISION X(M)
DOUBLE PRECISION Y(M)
DOUBLE PRECISION Y1(M)      !First derivative, dy/dx
DOUBLE PRECISION Y2(M)      !Second derivative, d(dy/dx)/dx
DOUBLE PRECISION T_cur(M)   !Surface tension
DOUBLE PRECISION YU(M-2)    !X explicit difference
DOUBLE PRECISION YL(M-2)    !X implicit difference
DOUBLE PRECISION XU(M-2)    !Y explicit difference
DOUBLE PRECISION XL(M-2)    !Y implicit difference

XU=X(3:M)-X(2:M-1);XL=X(1:M-2)-X(2:M-1)
YU=Y(3:M)-Y(2:M-1);YL=Y(1:M-2)-Y(2:M-1)
!Interior nodes
Y1(2:M-1)=XU*YL/(XL*(XU-XL))-XL*YU/(XU*(XU-XL))
!BC node
Y1(1)=((X(3)-X(1))*(Y(2)-Y(1))/(X(2)-X(1))-
        (X(2)-X(1))*(Y(3)-Y(1))/(X(3)-X(1)))/(X(3)-X(2))      &
Y1(M) = ((X(M-2)-X(M))*(Y(M-1)-Y(M))/(X(M-1)-X(M))-(X(M-1)-
        X(M))*(Y(M-2)-Y(M))/(X(M-2)-X(M)))/(X(M-2)-X(M-1))    &
Y2(2:M-1)= 2*((Y(3:M)-Y(2:M-1))/XU-(Y(1:M-2)-Y(2:M-1))/XL)/ &
        (XU-XL)
Y2(1)= 2*((Y(3)-Y(1))/(X(3)-X(1))-(Y(2)-Y(1))/(X(2)-X(1)))/ &
        (X(3)-X(2))
Y2(M) = 2*((Y(M-2)-Y(M))/(X(M-2)-X(M))-(Y(M-1)-Y(M))/(X(M-1) &
        -X(M)))/(X(M-2)-X(M-1))

T_cur=1/(y*sqrt(1+y1**2))-y2/sqrt(1+y1**2)**3 !Young-Laplace

end subroutine curvature

```

Subroutine: Gradient

```

! SUBROUTINE FOR FINDING FIRST ORDER GRADIENT BY NONUNIFORM GRID
SUBROUTINE GRADIENT(X,Y,M,Y1)
INTEGER M, I, J
double precision X(M)
double precision Y(M)
double precision Y1(M)      !first order derivative, dy/dx
double precision XU(M-2)    !X explicit difference
double precision XL(M-2)    !X implicit difference
XU = X(3:M)-X(2:M-1);XL=X(1:M-2)-X(2:M-1)
Y1(2:M-1) = XU*(Y(1:M-2)-Y(2:M-1))/(XL*(XU-XL))-XL*(Y(3:M)- &
           Y(2:M-1))/(XU*(XU-XL))
Y1(1) = ((X(3)-X(1))*(Y(2)-Y(1))/(X(2)-X(1))-(X(2)-X(1))* &
         (Y(3)-Y(1))/(X(3)-X(1)))/(X(3)-X(2))
Y1(M) = ((X(M-2)-X(M))*(Y(M-1)-Y(M))/(X(M-1)-X(M))-(X(M-1)- &
         X(M))*(Y(M-2)-Y(M))/(X(M-2)-X(M)))/(X(M-2)-X(M-1))
END SUBROUTINE GRADIENT

```

Subroutine: Galerkincoe

```

subroutine galerkincoe(a) !Define the modal shape parameters
double precision a      !Plate radius
double precision v      !Poisson ratio
double precision z1     !Nozzle deflection
double precision z2     !Nozzle velocity
double precision beta   !Mode shape parameter
double precision c1,c2,c4
double precision mue,phi,Q,mue_con_f,phi_con_f,Q_con_f
integer i,j
double precision WW(32),ZZ(32)

common /large/ mue, phi, Q, beta, z1, z2

!Parameters of Guass-Legendre quardature
data WW /  0.00701814576495, 0.01627742658310, &
           0.02539100983290, 0.03427454784770, &
           0.04283598967850, 0.05099787381170, &
           0.05868393946150, 0.06582206035780, &
           0.07234560942970, 0.07819369576200, &
           0.08331171110300, 0.08765186880470, &
           0.09117364548780, 0.09384415904230, &
           0.09563847545120, 0.09653984158110, &
           0.09653984158110, 0.09563847545120, &
           0.09384415904230, 0.09117364548780, &
           0.08765186880470, 0.08331171110300, &
           0.07819369576200, 0.07234560942970, &
           0.06582206035780, 0.05868393946150, &
           0.05099787381170, 0.04283598967850, &
           0.03427454784770, 0.02539100983290, &
           0.01627742658310, 0.00701814576495 /
data ZZ / -0.99726386184900, -0.98561151154500, &
           -0.96476225558800, -0.93490607593800, &
           -0.89632115576600, -0.84936761373300, &
           -0.79448379596800, -0.73218211874000, &
           -0.66304426693000, -0.58771575724100, &
           -0.50689990893200, -0.42135127613100, &
           -0.33186860228200, -0.23928736225200, &
           -0.14447196158300, -0.04830766568770, &
           0.04830766568770, 0.14447196158300, &
           0.23928736225200, 0.33186860228200, &
           0.42135127613100, 0.50689990893200, &
           0.58771575724100, 0.66304426693000, &
           0.73218211874000, 0.79448379596800, &
           0.84936761373300, 0.89632115576600, &
           0.93490607593800, 0.96476225558800, &
           0.98561151154500, 0.99726386184900 /

v=0.35      !Poisson ration
c1=-2      !Mode parameter for initial condition

```

```

c2=1                                !Mode parameter for initial condition
c4=(-1)*(3*(v-3)*c1**2+4*(v-5)*c1*c2+2*(v-7)*c2**2)/(24*(v-1))
                                !Stress function parameter
beta=3.19622/a
mue_con_f =0                       !Initial flag of Mue constant
phi_con_f =0                        !Initial flag of Phi constant
Q_con_f   =0                        !Initial flag of Q constant
mue=0
phi=0
Q=0
do i=1,32                            !Finding Interval Integration by
                                Guass-Legendre quarature
mue_con_f = WW(i)*(fun_phee(a/2+a*ZZ(i)/2))**2*(a/2+a*ZZ(i)/2)
phi_con_f = WW(i)*fun_phi(a/2+a*ZZ(i)/2)*                                &
                                fun_phee(a/2+a*ZZ(i)/2) *(a/2+a*ZZ(i)/2)
Q_con_f   = WW(i)*fun_phee(a/2+a*ZZ(i)/2)*(a/2+a*ZZ(i)/2)

mue =mue+mue_con_f
phi =phi+phi_con_f
Q   =Q+Q_con_f
enddo
mue = 0.5*(a-0)*mue                !Orthogonal parameter of Large
                                deflection equation
phi = 0.5*(a-0)*phi                !Orthogonal parameter of Large
                                deflection equation
Q   = 0.5*(a-0)*Q                  !Orthogonal parameter of Large
                                deflection equation

z1=0.0
z2=0.0

contains                            !Function doing the othogonalization
double precision function fun_phee(rr)
                                !Finding orthogonal parameter
double precision rr
fun_phee=(1+c1*(rr/a)**2+c2*(rr/a)**4
end function fun_phee

double precision function fun_phi(rr)
                                !Function doing the othogonalization
double precision rr
fun_phi = (8*c1*c4+2*(c1**3+16*c2*c4)*(rr/a)**2+10*c1**2*c2* &
            (rr/a)**4+(40/3)*c1*c2**2*(rr/a)**6+(20/3)*c2**3* &
            (rr/a)**8 )
end function fun_phi

end subroutine galerkincoe

```

Function: P

```

! Bulid a pressure function to be easilly called
FUNCTION P(X)
INTEGER N, M
DOUBLE PRECISION, PARAMETER :: PI = 3.14159265358979
DOUBLE PRECISION F
DOUBLE PRECISION T_pul
DOUBLE PRECISION PMAX !Pressure magnitude
DOUBLE PRECISION P !Pressure output
DOUBLE PRECISION X !Time
CHARACTER PFUNC !Pressure function selector

COMMON /PRESSURE/ PFUNC, F, T_pul, PMAX

IF (PFUNC .EQ. 'S') THEN
  P = PMAX*SIN(2*PI*F*X)

  ELSEIF (PFUNC .EQ. 'C') THEN
    P = PMAX*COS(2*PI*F*X)

    ELSEIF (PFUNC .EQ. 'Q') THEN
      M = 2*PI*F*X
      P = PMAX*(-1)**M

      ELSEIF (PFUNC .EQ. 'P') THEN

        IF (X .LE. T_pul) THEN
          P = PMAX

          ELSE
            P = 0
          ENDIF
        ELSE
          PRINT*, 'INPUT IS WRONG'
        END IF
      END FUNCTION P

```

Function: Uoriout

```
FUNCTION UORIOUT(N,VIN,PSUR,dT,L)
INTEGER N                !The time step number
DOUBLE PRECISION P      !Driving pressure
DOUBLE PRECISION UORIOUT !Nozzle flow velocity
DOUBLE PRECISION L      !Nozzle length
DOUBLE PRECISION dT
DOUBLE PRECISION VIN     !Velocity at previous time step
DOUBLE PRECISION PSUR    !Surface tension at nozzle outlet
UORIOUT=VIN+((P((N-1)*dT)+P(N*dT))/2-PSUR)*dT/L
END FUNCTION UORIOUT
```

Function: Wplate

```

! Nozzle deflection
function wplate(n)

double precision wplate
double precision c, E, h, D, mas, beta, P, a, dt, WR, Bo
double precision mue, phi, Q
integer i, j, n
double precision z1, z2, zk2, zk3
double precision k1_zz1, k1_zz2, k2_zz1, k2_zz2, k3_zz1, k3_zz2, &
                k4_zz1, k4_zz2

common /plate/ a, mas, D, E, c
common /CONSTANT/ WR, h, dt, Bo
common /large/ mue, phi, Q, beta, z1, z2

k1_zz1=z2*dt
k1_zz2 = ((1/(mas*mue))*(Q*P(n*dt)-E*h*phi*z1**3/a**4-D*mue*&
        beta**4*z1-c*mue*z2))*dt

k2_zz1=(z2+0.5*k1_zz2)*dt
zk2=z1+0.5*k1_zz1
k2_zz2 = ((1/(mas*mue))*(Q*P(n*dt)-E*h*phi*zk2**3/a**4-D*mue*&
        beta**4*zk2-c*mue*(z2+0.5*k1_zz2)))*dt

k3_zz1=(z2+0.5*k2_zz2)*dt
zk2=z1+0.5*k2_zz1
k3_zz2 = ((1/(mas*mue))*(Q*P(n*dt)-E*h*phi*zk2**3/a**4-D*mue*&
        beta**4*zk2-c*mue*(z2+0.5*k2_zz2)))*dt

k4_zz1=(z2+k3_zz2)*dt
zk3=z1+k3_zz1
k4_zz2 = ((1/(mas*mue))*(Q*P(n*dt)-E*h*phi*zk3**3/a**4-D*mue*&
        beta**4*zk3-c*mue*(z2+k3_zz2)))*dt

z1=z1+(k1_zz1+2*k2_zz1+2*k3_zz1+k4_zz1)/6
z2=z2+(k1_zz2+2*k2_zz2+2*k3_zz2+k4_zz2)/6
wplate=z1
end function wplate

```

Function: Uplate

```
! Nozzle vibration velocity
function uplate(n)
double precision uplate
double precision mue, phi, Q, beta, z1, z2
integer n

common /large/ mue, phi, Q, beta, z1, z2

uplate = z2

end function uplate
```

APPENDIX B

MATLAB Program for Data Processing

The MATLAB programs attached are the programs used to detect the break-off information from the data file generated by the FORTRAN source code. The functions of the MATLAB programs developed are explained in Section 5.2. The codes attached are based on a specific case data process. Data process for other cases can be achieved by simply changing the file names.

Timeseriesplot.m

```

format long;

load('C:\master thesis\rigid vibration\vibration\P10
T0.15\orifice');
load('C:\master thesis\rigid vibration\vibration\P10
T0.15\zlocation');
zlocation=zlocation';

load('C:\master thesis\rigid vibration\vibration\P10 T0.15\RADIUS');
RADIUS=RADIUS';

load('C:\master thesis\rigid vibration\vibration\P10 T0.15\time');

figure;
NN=3;
subplot(5,2,1);
plot(zlocation(:,NN),RADIUS(:,NN),'k');hold on;
plot(zlocation(:,NN),-RADIUS(:,NN),'k');
axis([0 40 -4 4]);
t=num2str(time(2,NN));
tit=strcat('t^*=',t,' half sphere formed');
title(tit);
set(gca,'DataAspectRatio',[1 1 1]);
set(gca,'PlotBoxAspectRatio',[5 1 1]);
set(gca,'ytick',[-4 0 4]);

NN=11;
subplot(5,2,3);
plot(zlocation(:,NN),RADIUS(:,NN),'k');hold on;
plot(zlocation(:,NN),-RADIUS(:,NN),'k');
axis([0 40 -4 4]);
t=num2str(time(2,NN));
tit=strcat('t^*=',t);
title(tit);
set(gca,'DataAspectRatio',[1 1 1]);
set(gca,'PlotBoxAspectRatio',[5 1 1]);
set(gca,'ytick',[-4 0 4]);

NN=21;
subplot(5,2,5);
plot(zlocation(:,NN),RADIUS(:,NN),'k'); hold on;
plot(zlocation(:,NN),-RADIUS(:,NN),'k');
axis([0 40 -4 4]);
t=num2str(time(2,NN));
tit=strcat('t^*=',t);
title(tit);
set(gca,'DataAspectRatio',[1 1 1]);%axis equal;
set(gca,'PlotBoxAspectRatio',[5 1 1]);

```

```

set(gca,'ytick',[-4 0 4]);

NN=31;
subplot(5,2,7);
plot(zlocation(:,NN),RADIUS(:,NN),'k')hold on;
plot(zlocation(:,NN));-RADIUS(:,NN),'k');
axis([0 40 -4 4]);
t=num2str(time(2,NN));
tit=strcat('t^*=',t);
title(tit);
set(gca,'DataAspectRatio',[1 1 1]);
set(gca,'PlotBoxAspectRatio',[5 1 1]);
set(gca,'ytick',[-4 0 4]);

NN=35;
subplot(5,2,9);
plot(zlocation(:,NN),RADIUS(:,NN),'k'); hold on;
plot(zlocation(:,NN),-RADIUS(:,NN),'k');
axis([0 40 -4 4]);
t=num2str(time(2,NN));
tit=strcat('t^*=',t);
title(tit);
set(gca,'DataAspectRatio',[1 1 1]);
set(gca,'PlotBoxAspectRatio',[5 1 1]);
set(gca,'ytick',[-4 0 4]);

NN=37;
subplot(5,2,2);
plot(zlocation(:,NN),RADIUS(:,NN),'k'); hold on;
plot(zlocation(:,NN),-RADIUS(:,NN),'k');
axis([0 40 -4 4]);
t=num2str(time(2,NN));
tit=strcat('t^*=',t,' Primary break-off');
title(tit);
set(gca,'DataAspectRatio',[1 1 1]);
set(gca,'PlotBoxAspectRatio',[5 1 1]);
set(gca,'ytick',[-4 0 4]);

ND=37; NF=104;MM=2;
subplot(5,2,4);
zdrop=zlocation(:,ND+MM)+orifice(ND,2)*(time(ND+MM,2)-time(ND,2));
zdrop=zdrop+orifice(ND,1)-orifice(ND+MM-1,1);
plot(zdrop,RADIUS(:,ND+MM),'k',zdrop,-RADIUS(:,ND+MM),'k');hold on;
plot(zlocation(:,NF+MM),RADIUS(:,NF+MM),'k'); hold on;
plot(zlocation(:,NF+MM),-RADIUS(:,NF+MM),'k');
axis([0 40 -4 4]);
t=num2str(time(2,ND+MM));
tit=strcat('t^*=',t);
title(tit);
set(gca,'DataAspectRatio',[1 1 1]);
set(gca,'PlotBoxAspectRatio',[5 1 1]);
set(gca,'ytick',[-4 0 4]);

ND=37; NF=104;MM=6;

```

```

subplot(5,2,6);
zdrop=zlocation(:,ND+MM)+orifice(ND,2)*(time(ND+MM,2)-time(ND,2));
zdrop=zdrop+orifice(ND,1)-orifice(ND+MM-1,1);
plot(zdrop,RADIUS(:,ND+MM),'k',zdrop,-RADIUS(:,ND+MM),'k');hold on;
plot(zlocation(:,NF+MM),RADIUS(:,NF+MM),'k'); hold on;
plot(zlocation(:,NF+MM),-RADIUS(:,NF+MM),'k');
axis([0 40 -4 4]);
t=num2str(time(2,ND+MM));
tit=strcat('t^*=',t);
title(tit);
set(gca,'DataAspectRatio',[1 1 1]);
set(gca,'PlotBoxAspectRatio',[5 1 1]);
set(gca,'ytick',[-4 0 4]);

```

```

ND=37; NF=104;MM=8;
subplot(5,2,8);
zdrop=zlocation(:,ND+MM)+orifice(ND,2)*(time(ND+MM,2)-time(ND,2));
zdrop=zdrop+orifice(ND,1)-orifice(ND+MM-1,1);
plot(zdrop,RADIUS(:,ND+MM),'k',zdrop,-RADIUS(:,ND+MM),'k');hold on;
plot(zlocation(:,NF+MM),RADIUS(:,NF+MM),'k'); hold on;
plot(zlocation(:,NF+MM),-RADIUS(:,NF+MM),'k');
axis([0 40 -4 4]);
t=num2str(time(2,ND+MM));
tit=strcat('t^*=',t);
title(tit);
set(gca,'DataAspectRatio',[1 1 1]);
set(gca,'PlotBoxAspectRatio',[5 1 1]);
set(gca,'ytick',[-4 0 4]);

```

```

ND=37; NF=104;MM=10;
subplot(5,2,10);
zdrop=zlocation(:,ND+MM)+orifice(ND,2)*(time(ND+MM,2)-time(ND,2));
zdrop=zdrop+orifice(ND,1)-orifice(ND+MM-1,1);
plot(zdrop,RADIUS(:,ND+MM),'k',zdrop,-RADIUS(:,ND+MM),'k');hold on;
plot(zlocation(:,NF+MM),RADIUS(:,NF+MM),'k'); hold on;
plot(zlocation(:,NF+MM),-RADIUS(:,NF+MM),'k');
axis([0 40 -4 4]);
t=num2str(time(2,ND+MM));
tit=strcat('t^*=',t,' Satellite break-off');
title(tit);
set(gca,'DataAspectRatio',[1 1 1]);
set(gca,'PlotBoxAspectRatio',[5 1 1]);
set(gca,'ytick',[-4 0 4]);

```

```

set(gcf,'unit','inches');
set(gcf,'position',[0 0 6 8]);
set(gcf,'paperposition',[0 0 6 8]);
set(gcf,'color','w');

```

```

print -fl -dtiff -r600 VPP100T015

```

Breakoffshapesave.m

```
format long;

load('C:\master thesis\rigid vibration\vibration\P10
T0.15\orifice');
load('C:\master thesis\rigid vibration\vibration\P10
T0.15\zlocation');
zlocation=zlocation';

load('C:\master thesis\rigid vibration\vibration\P10 T0.15\RADIUS');
RADIUS=RADIUS';

load('C:\master thesis\rigid vibration\vibration\P10 T0.15\time');

n=length(time(2,:)); %find the length of time array
tche=0.1:0.1:0.1*n; %Set the array to compare

%Find time for halfsphere forms
[k, j]=find(abs(time(2,.)-tche) >0.000001);

%Cut off initial stage records
ttime=time(2,j);

%Find first break-off time
[kk, jj]=find(abs(ttime-tche(j)+0.1)>0.000001)
ND=jj(2)+n-length(j);
%jj(1) is the half hemisphere forms
%jj(2) is the first break-off

zvibwr60p10t015=zlocation(:,ND);rvibwr60p10t015=RADIUS(:,ND);
savefile='vibwr60p10t015';
save(savefile,'zvibwr60p10t015','rvibwr60p10t015');
```

Breakoffshapesave.m

```

load rigwr5p10t012.mat;
load rigwr5p10t015.mat;
load rigwr5p10t02.mat;
load rigwr5p10t025.mat;

load rigwr60p10t012.mat;
load rigwr60p10t015.mat;
load rigwr60p10t02.mat;
load rigwr60p10t025.mat;

load vibwr5p10t012.mat;
load vibwr5p10t015.mat;
load vibwr5p10t02.mat;
load vibwr5p10t025.mat;
load vibwr60p10t012.mat;
load vibwr60p10t015.mat;
load vibwr60p10t02.mat;
load vibwr60p10t025.mat;

z(:,1)=zwr5p10t012;r(:,1)=rwr5p10t012;
z(:,2)=zvibr60p10t012;r(:,2)=rvibr60p10t012;
z(:,3)=zwr5p10t015;r(:,3)=rwr5p10t015;
z(:,4)=zvibr60p10t015;r(:,4)=rvibr60p10t015;
z(:,5)=zwr5p10t02;r(:,5)=rwr5p10t02;
z(:,6)=zvibr60p10t02;r(:,6)=rvibr60p10t02;
z(:,7)=zwr5p10t025;r(:,7)=rwr5p10t025;
z(:,8)=zvibr60p10t025;r(:,8)=rvibr60p10t025;

z(:,9)=zrigwr5p10t012;r(:,9)=rrigwr5p10t012;
z(:,10)=zvibr5p10t012;r(:,10)=rvibr5p10t012;
z(:,11)=zrigwr5p10t015;r(:,11)=rrigwr5p10t015;
z(:,12)=zvibr5p10t015;r(:,12)=rvibr5p10t015;
z(:,13)=zrigwr5p10t02;r(:,13)=rrigwr5p10t02;
z(:,14)=zvibr5p10t02;r(:,14)=rvibr5p10t02;
z(:,15)=zrigwr5p10t025;r(:,15)=rrigwr5p10t025;
z(:,16)=zvibr5p10t025;r(:,16)=rvibr5p10t025;

str=['P^\cdotT=1.2';'P^\cdotT=1.2';'P^\cdotT=1.5';'P^\cdotT=1.5'
;'P^\cdotT=2.0';'P^\cdotT=2.0';'P^\cdotT=2.5';'P^\cdotT=2.5'];
for i=1:8
    subplot(4,2,i);
    plot(z(:,i),r(:,i),'k',z(:,i),-r(:,i),'k');
    axis([0 40 -4 4]);
    title(str(i,:));
    set(gca,'DataAspectRatio',[1 1 1]);
    set(gca,'PlotBoxAspectRatio',[5 1 1]);
    set(gca,'XTick',0:10:40,'YTick',-4:4:4);
end

```

```

set(gcf,'unit','inches');
set(gcf,'position',[0 0 6 5]);
set(gcf,'paperposition',[0 0 6 5]);
set(gcf,'color','w');
gtext('a','fontsize',14);gtext('b','fontsize',14);

figure;
%str=['P\cdotT_p_u_l_s_e=1.2';'P\cdotT_p_u_l_s_e=1.2';
      'P\cdotT_p_u_l_s_e=1.5';'P\cdotT_p_u_l_s_e=1.5';
      'P\cdotT_p_u_l_s_e=2.0';'P\cdotT_p_u_l_s_e=2.0';
      'P\cdotT_p_u_l_s_e=2.5';'P\cdotT_p_u_l_s_e=2.5'];
for i=1:8
    subplot(4,2,i);
    plot(z(:,i+8),r(:,i+8),'k',z(:,i+8),-r(:,i+8),'k');
    axis([0 40 -4 4]);
    title(str(i,:));
    set(gca,'DataAspectRatio',[1 1 1]);
    set(gca,'PlotBoxAspectRatio',[5 1 1]);
    set(gca,'XTick',0:10:40,'YTick',-4:4:4);
end

set(gcf,'unit','inches');
set(gcf,'position',[0 0 6 5]);
set(gcf,'paperposition',[0 0 6 5]);
set(gcf,'color','w');
gtext('a','fontsize',14);gtext('b','fontsize',14);

%print -f1 -dtiff -r300 f610
%print -f2 -dtiff -r300 f611

```

Breakofflength.m

```

format long;

%load('C:\master thesis\rigid vibration\vibration\P10
T0.15\orifice');
%load('C:\master thesis\rigid vibration\vibration\P10
T0.15\zlocation');
%zlocation=zlocation';

%load('C:\master thesis\rigid vibration\vibration\P10
T0.15\RADIUS');
%RADIUS=RADIUS';

%load('C:\master thesis\rigid vibration\vibration\P10 T0.15\time');

n=length(time(2,:)); %find the length of time array
tche=0.1:0.1:0.1*n; %Set the array to compare

%Find time for halfsphere forms
[k, j]=find(abs(time(2,.)-tche) >0.000001);

%Cut off initial stage records
ttime=time(2,j);

%Find first break-off time
[kk, jj]=find(abs(ttime-tche(j)+0.1)>0.000001)
ND=jj(2)+n-length(j);
NS=length(time(2,:));

zd=zlocation(:,ND);rd=RADIUS(:,ND);

zs=zlocation(:,NS);rd=RADIUS(:,NS);

rmind = min(rd(2:6400));
rmins = min(rs(2:6400));

if rmind < 0.001 % Threshold radius reached
    [rmind,I] = min(rd(2:6400));
    zmind=zs(I+1);
else % Threshold gradient reached
    [rmind,I] = min(rd(100:6400));
    zmind=zd(I+100);
end

if rmins < 0.001 % Threshold radius reached
    [rmins,I] = min(rs(2:6400));
    zmins=zs(I+1);
else % Threshold gradient reached

```

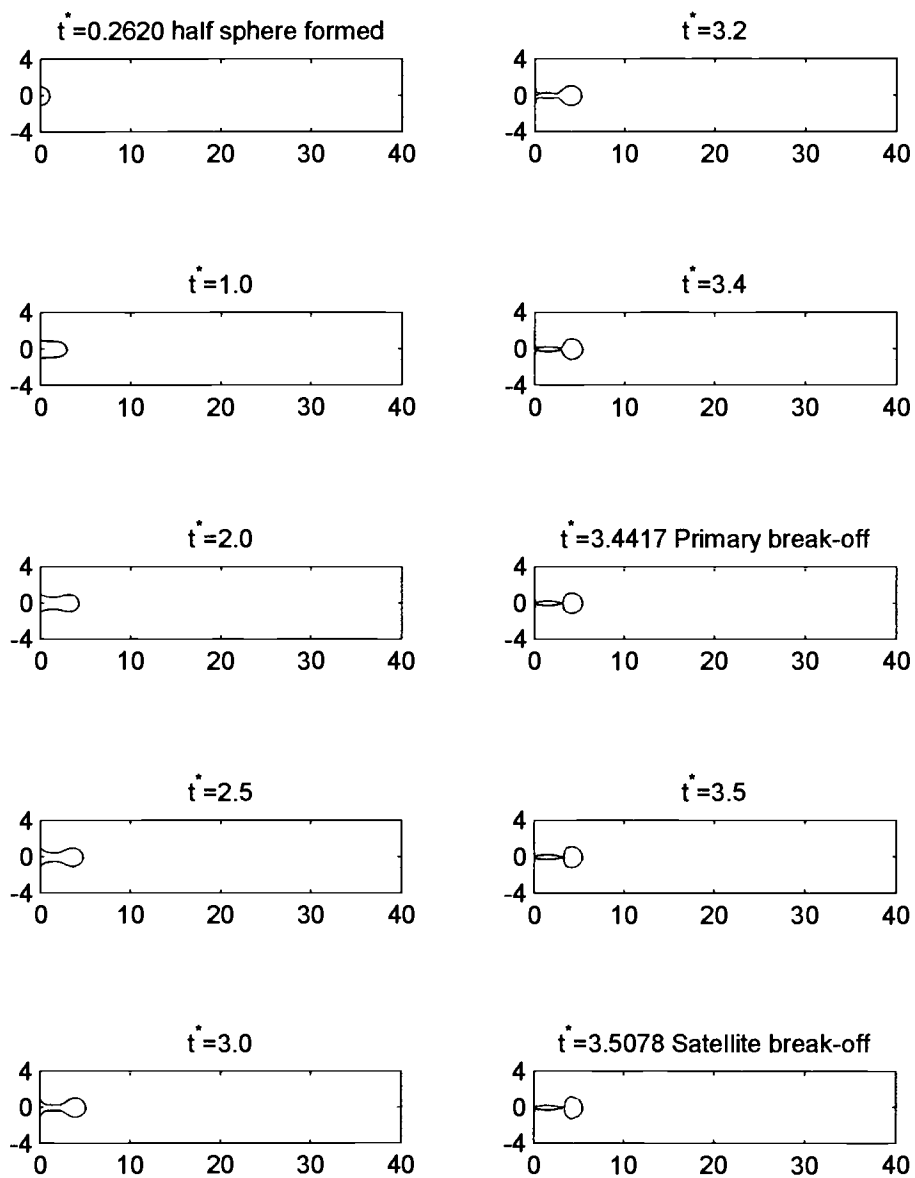
```
[rmins,I] = min(rs(100:6400));  
zmins=zs(I+100);  
end
```

APPENDIX C

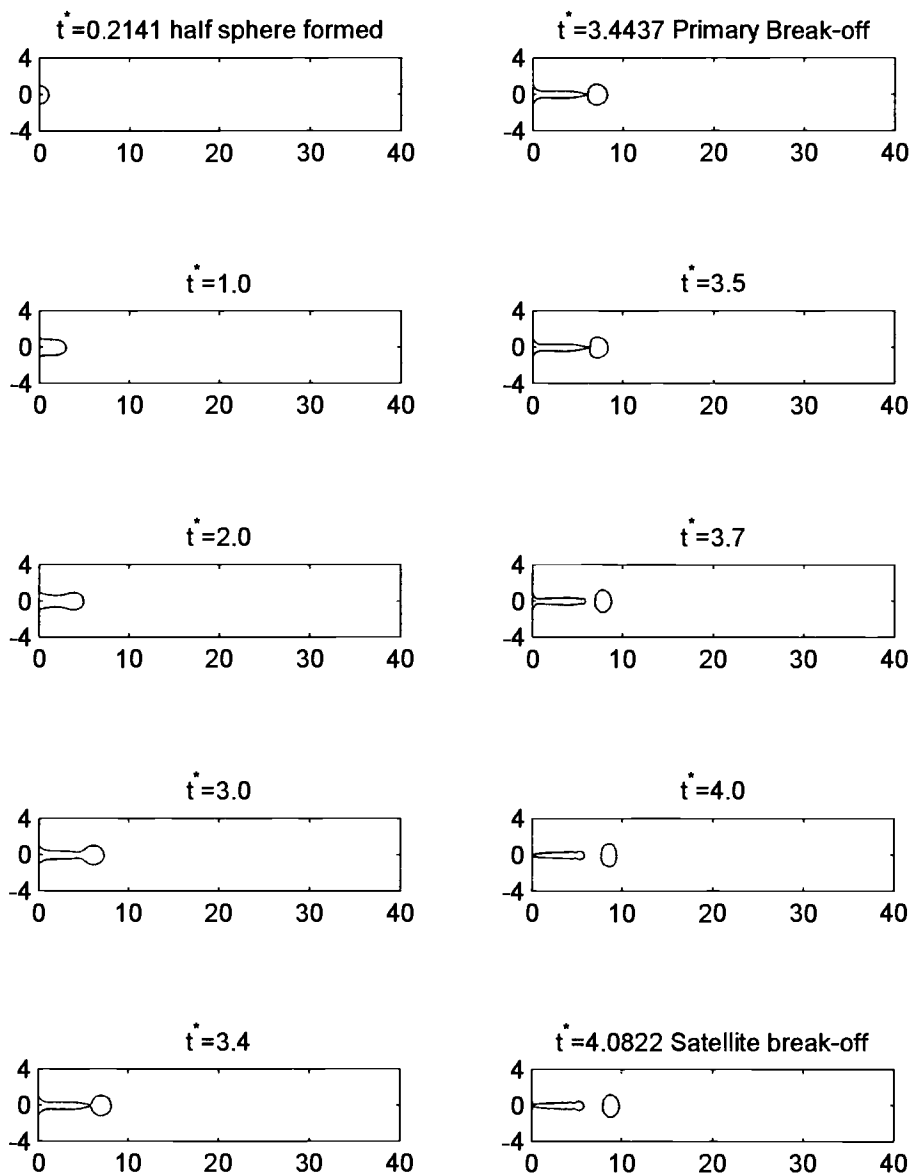
Sample Droplet Formation Time Sequence

The liquid shape plots that follows is the complete cases studied for making comparison between droplet formation from a rigid nozzle and that from a vibration nozzle. The droplet formation process for each cases studied contains ten liquid shape plots by time sequence, starting from a half hemisphere formed. The file name of each case appears at the top of the page of images, and contains the information about that case. For example, in the file name “R-RW60-P10-T0.12”: R indicates the nozzle studied is rigid nozzle; WR60 indicates the non-dimensional viscosity parameter, Re/We of the fluid studied is 60; P10 indicate the non-dimensional driving pressure magnitude is 10; T0.12 indicates the non-dimensional driving pressure pulse times is 0.12. A complete set of the droplet formation process liquid shape plots is available upon request.

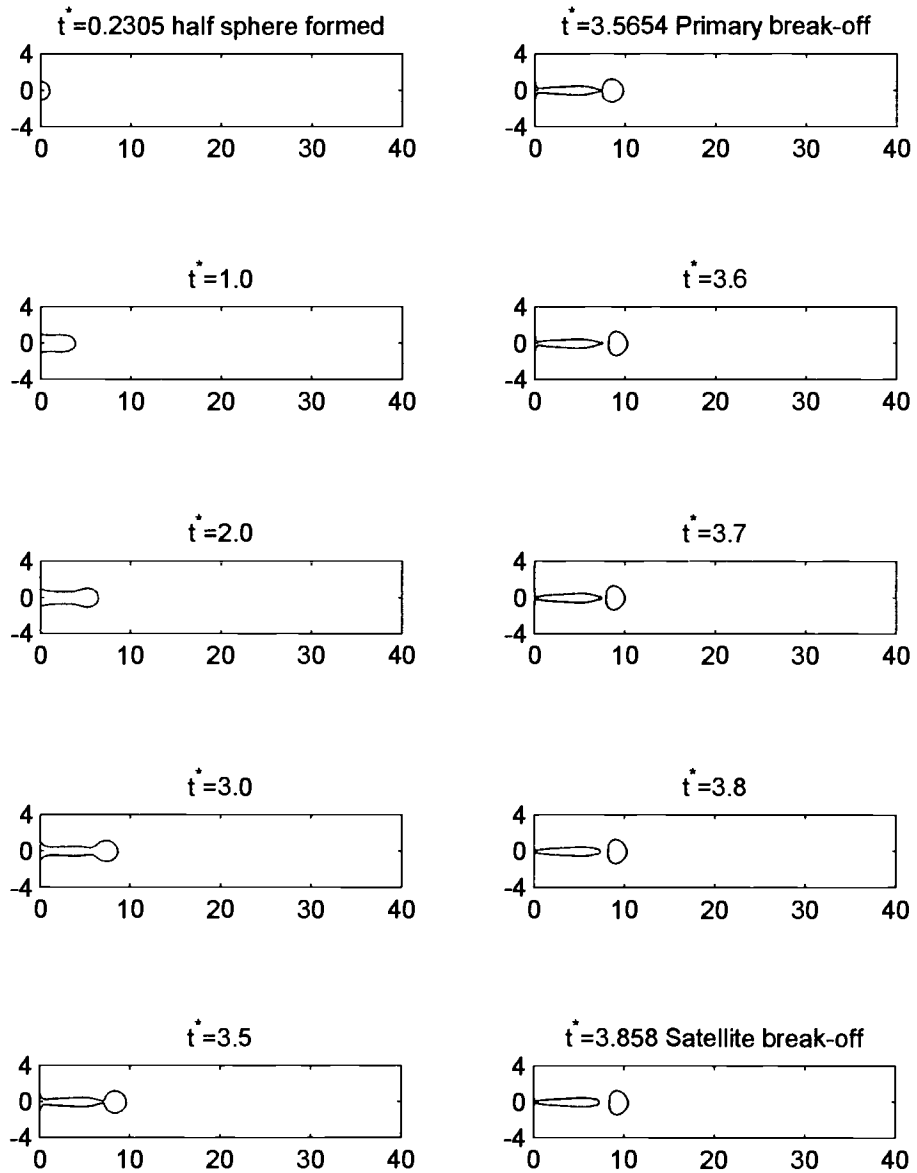
R-WR60-P10-T0.12



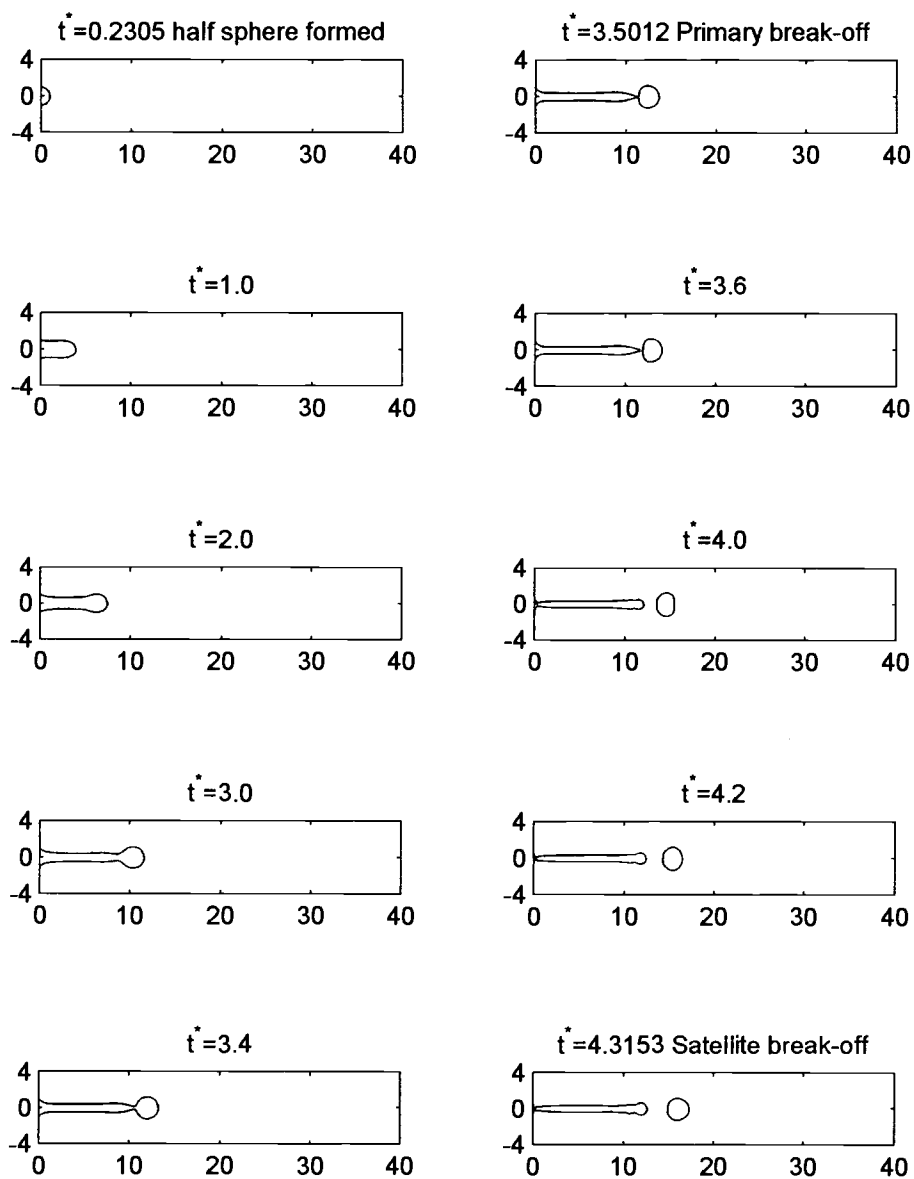
V-WR60-P10-T0.12



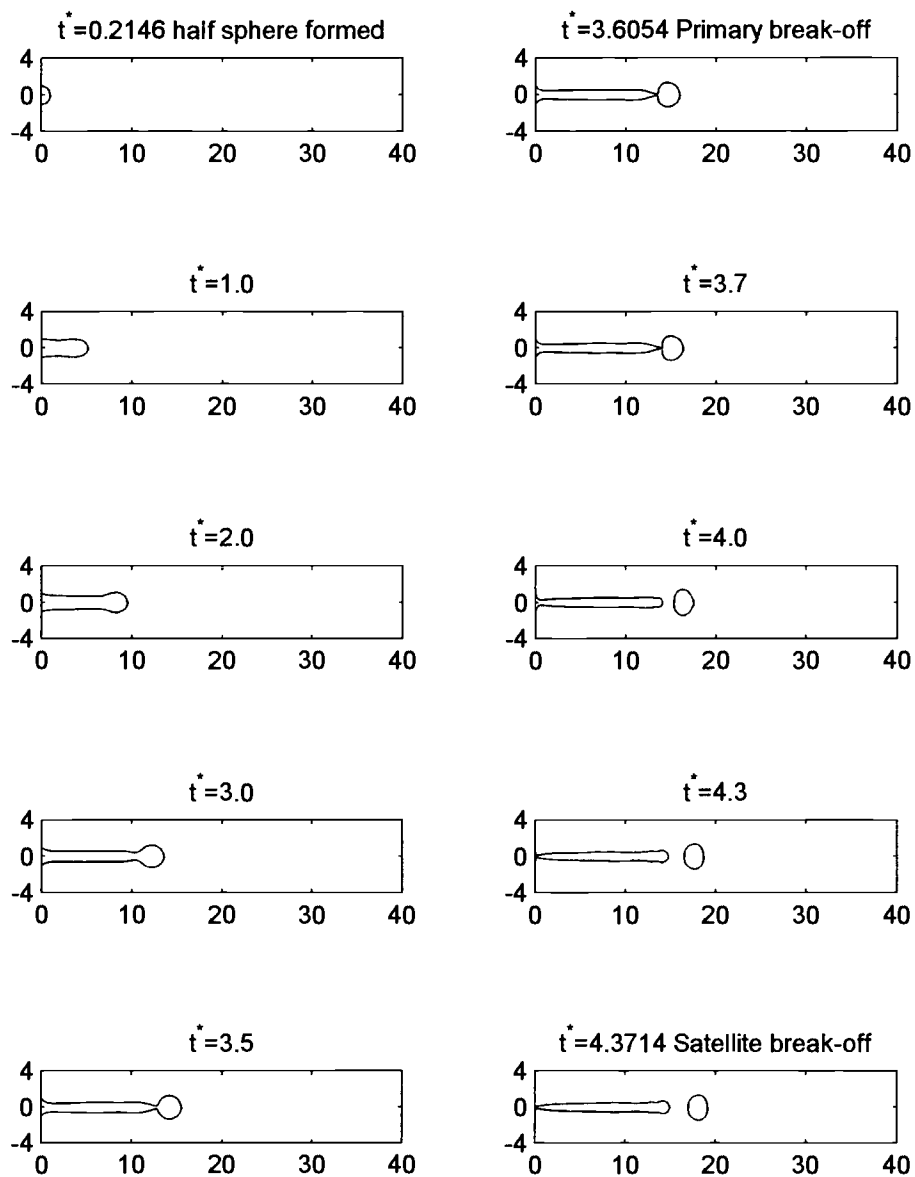
R-WR60-P10-T0.15



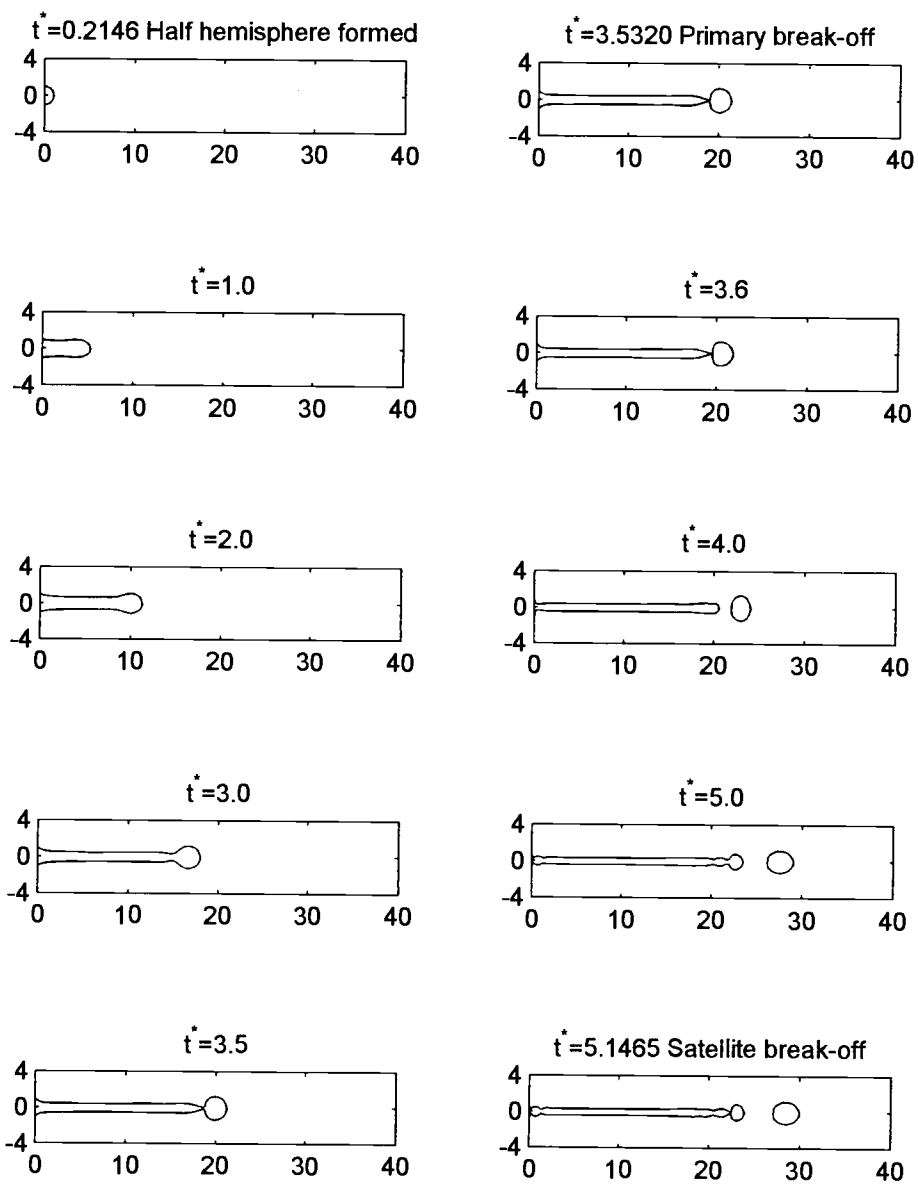
V-WR60-P10-T0.15



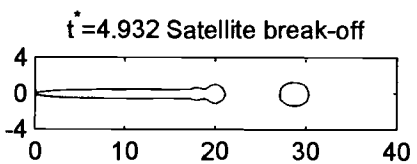
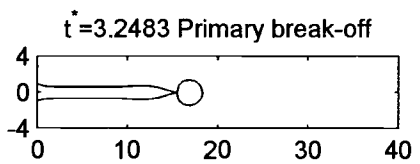
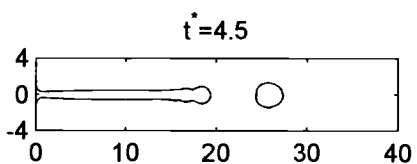
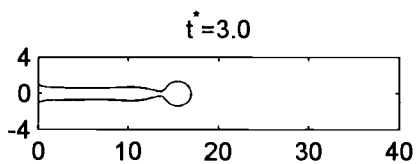
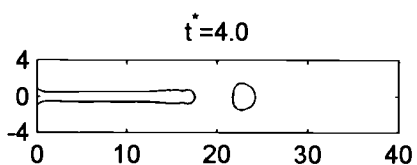
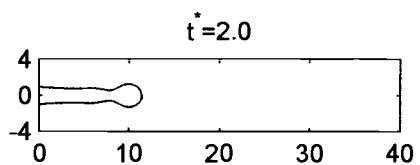
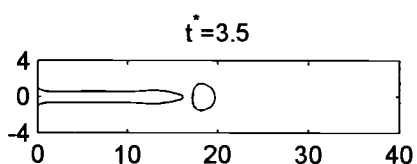
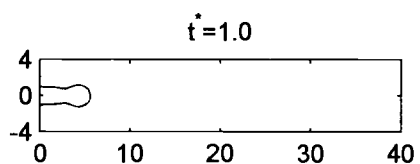
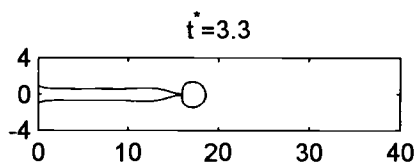
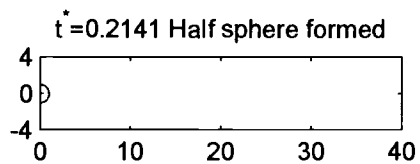
R-WR60-P10-T0.2



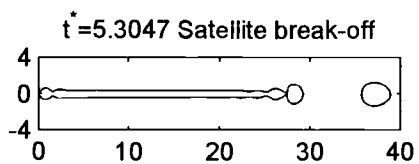
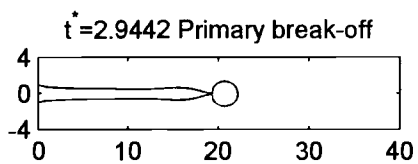
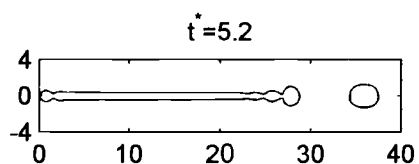
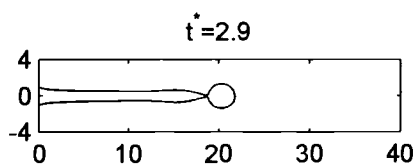
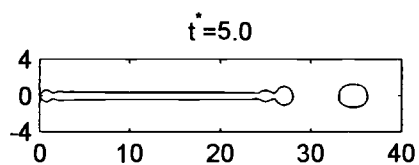
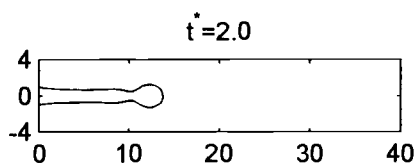
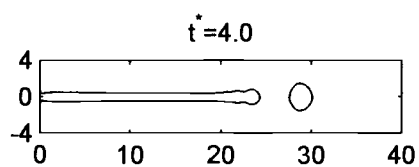
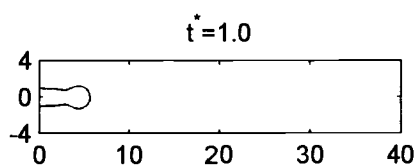
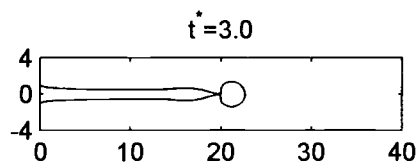
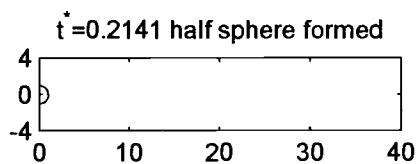
V-WR60-P10-T0.2



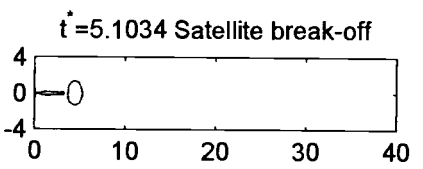
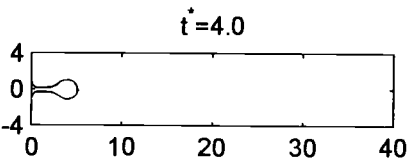
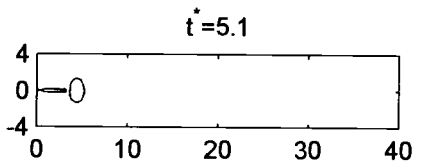
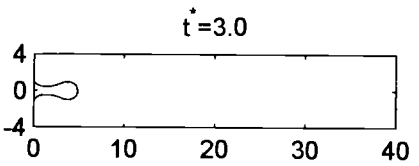
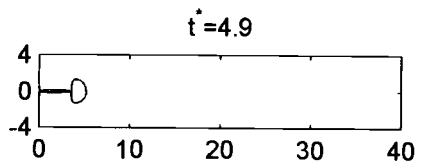
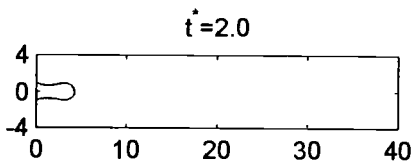
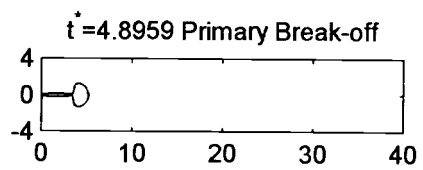
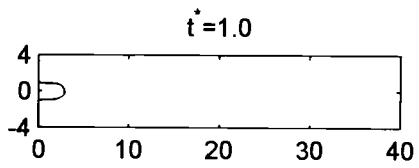
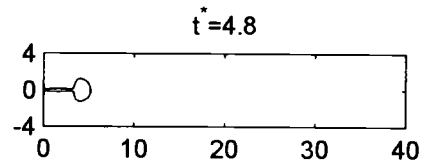
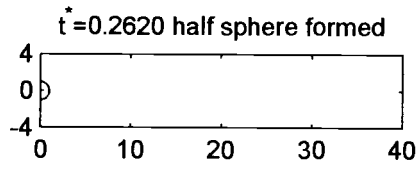
R-WR60-P10-T0.25



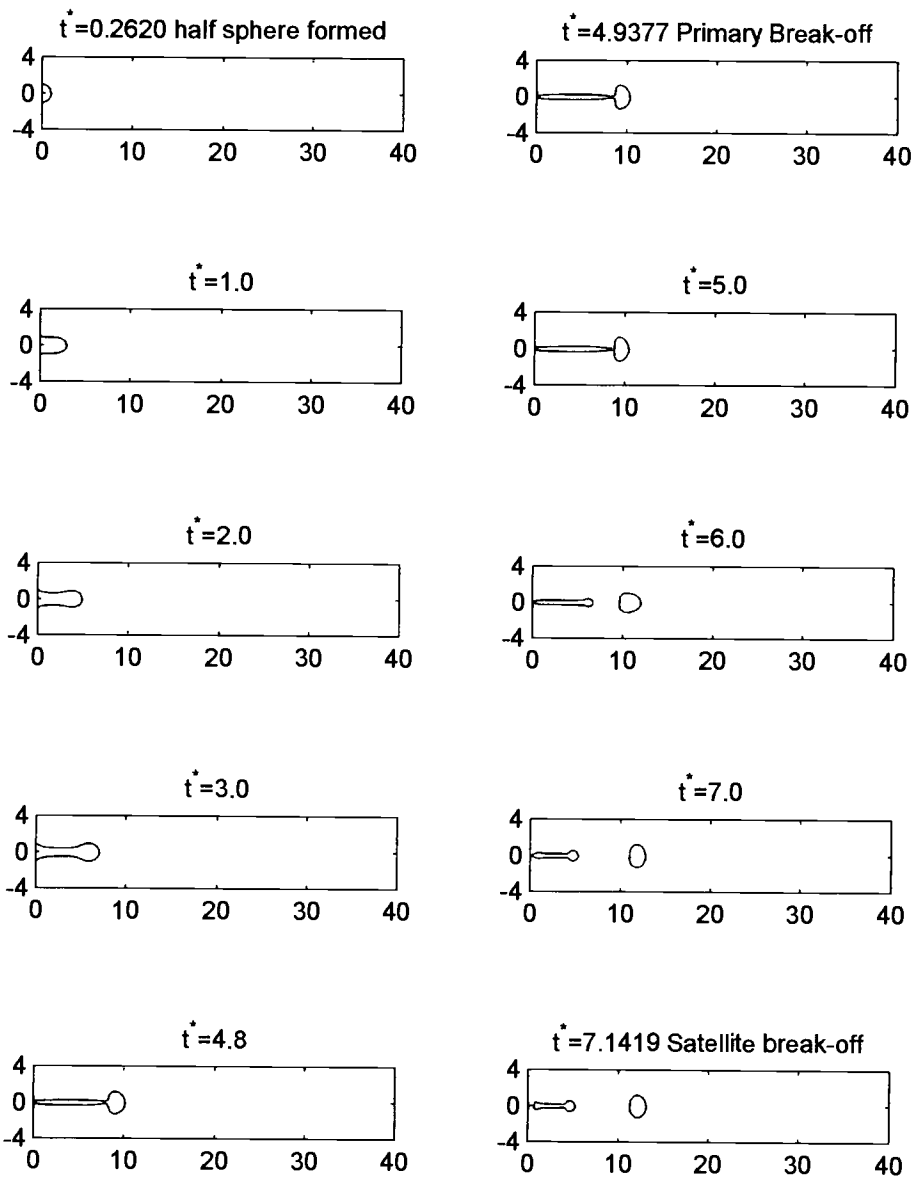
V-WR60-P10-T0.25



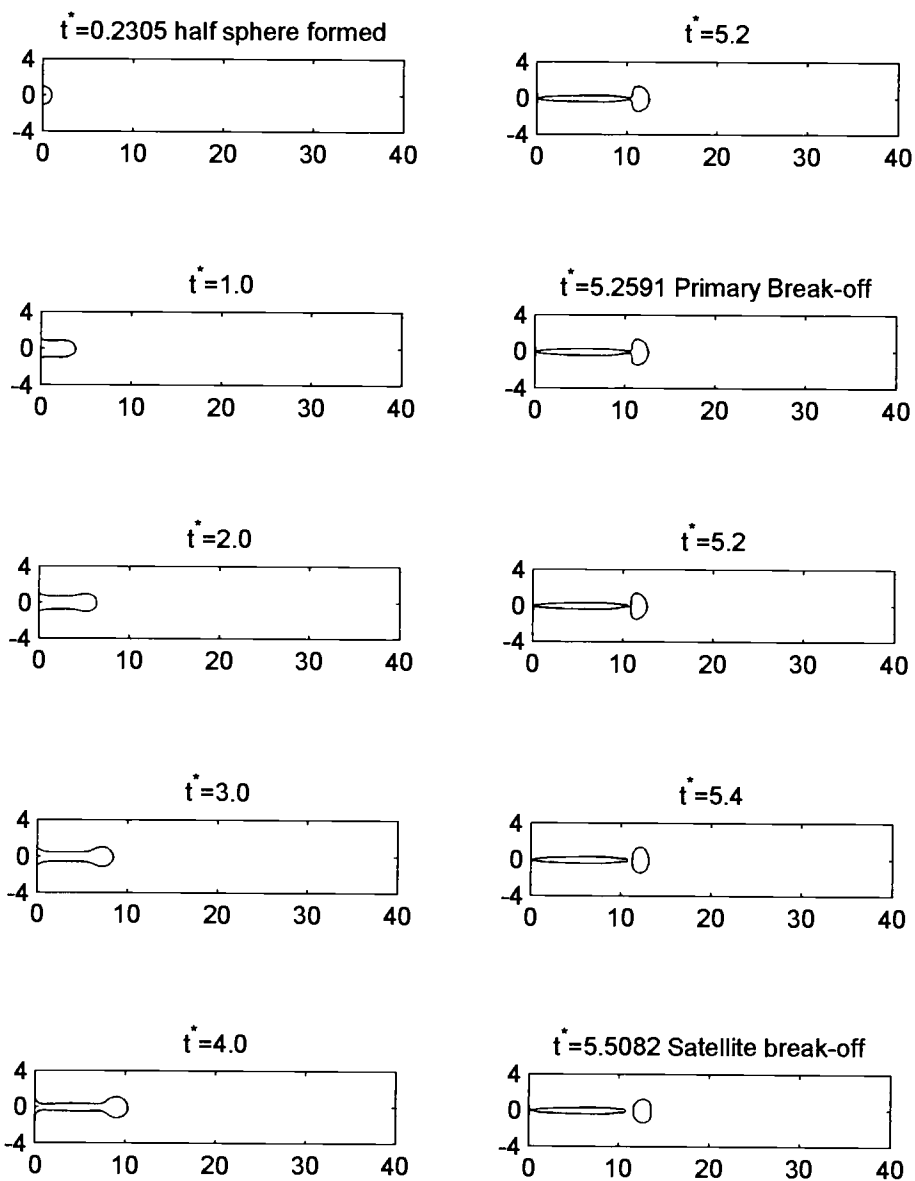
R-WR5-P10-T0.12



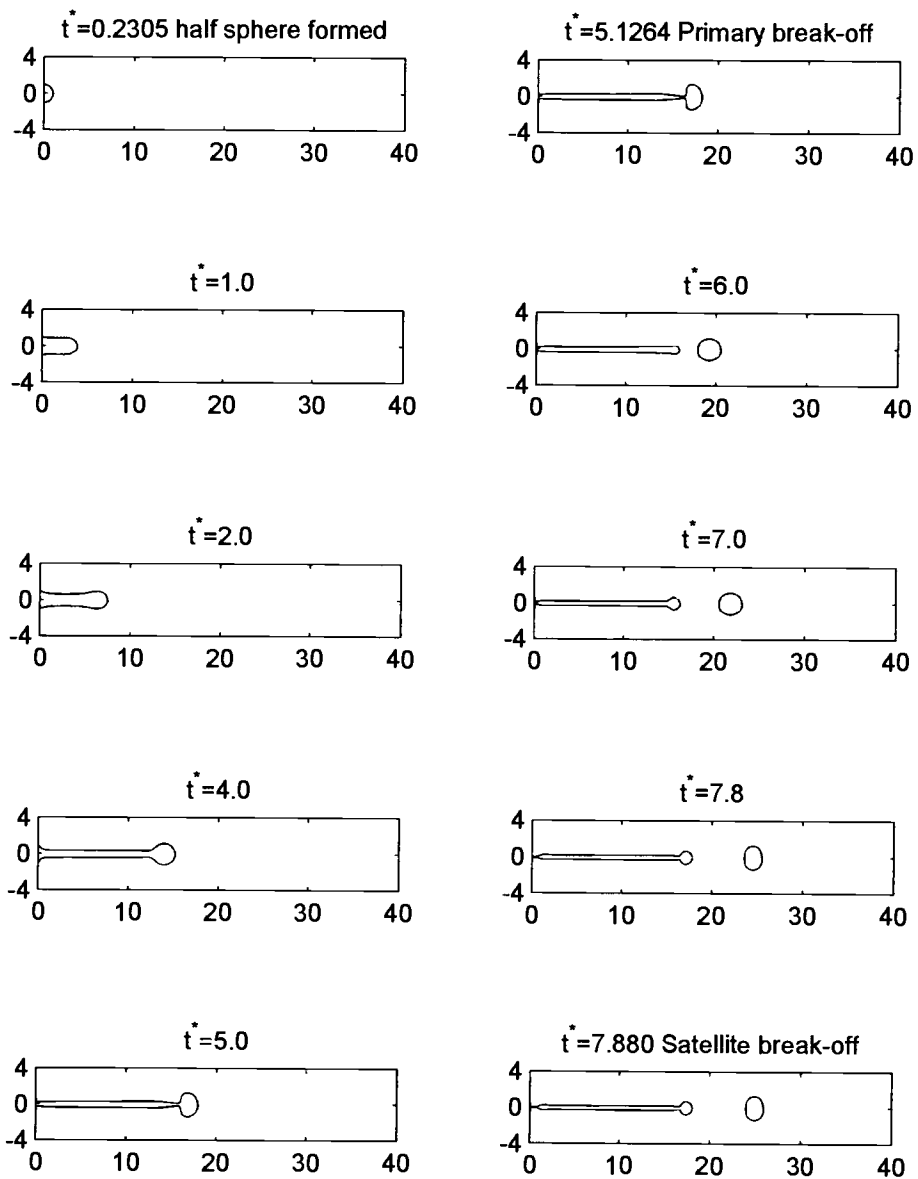
V-WR5-P10-T0.12



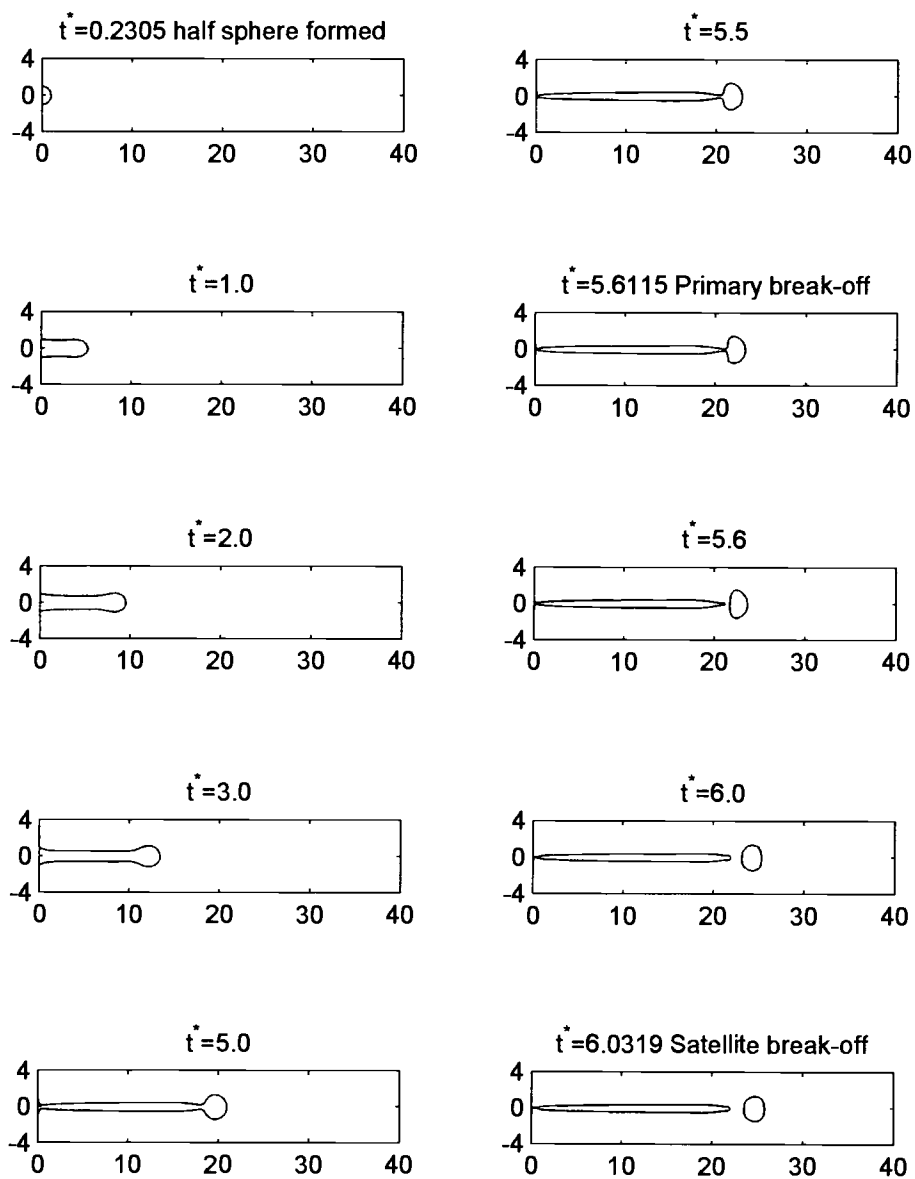
R-WR5-P10-T0.15



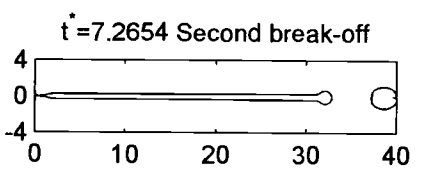
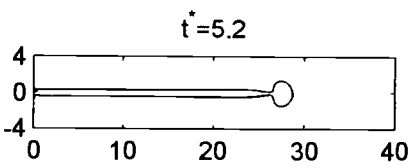
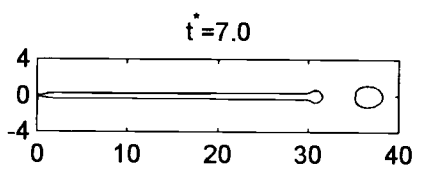
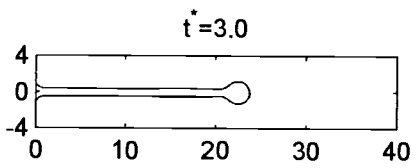
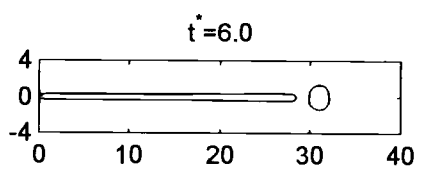
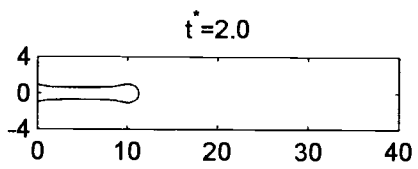
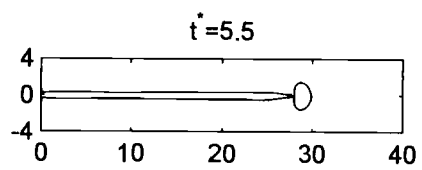
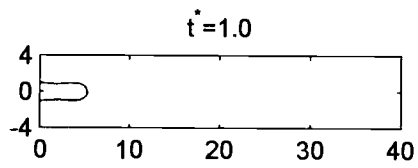
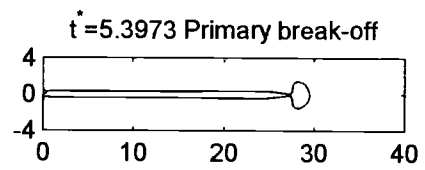
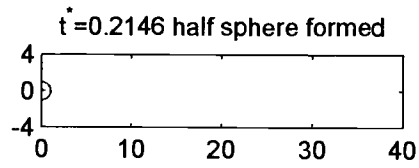
V-WR5-P10-T0.15



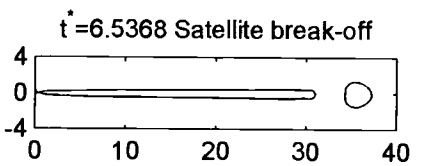
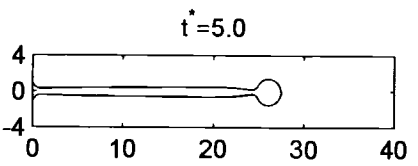
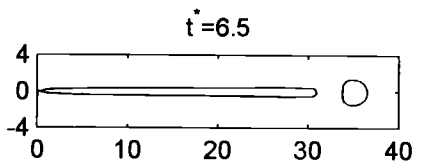
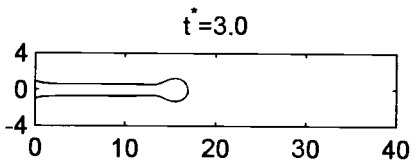
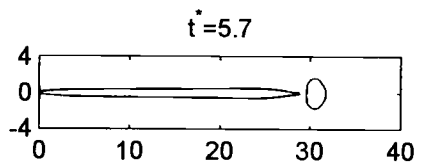
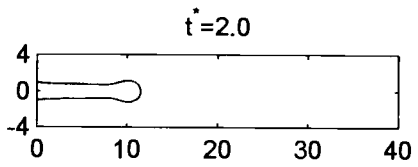
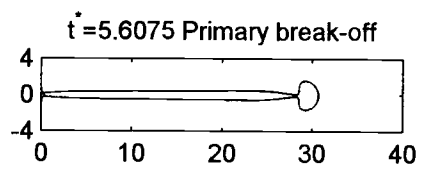
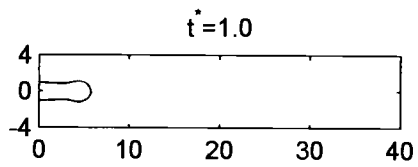
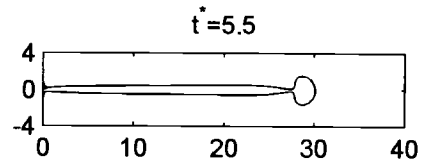
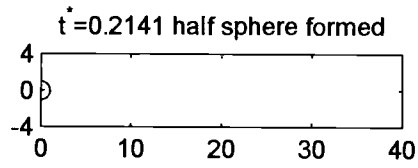
R-WR5-P10-T0.2



V-WR5-P10-T0.2



R-WR5-P10-T0.25



V-WR5-P10-T0.25

